



HAL
open science

Quadratic nonlinear optical properties of $\text{La}_3\text{Ga}_{5.5}\text{Nb}_{0.5}\text{O}_{14}$ (LGN) and periodically-poled Rb: KTiOPO_4 (PPRKTP) crystals

Dazhi Lu

► **To cite this version:**

Dazhi Lu. Quadratic nonlinear optical properties of $\text{La}_3\text{Ga}_{5.5}\text{Nb}_{0.5}\text{O}_{14}$ (LGN) and periodically-poled Rb: KTiOPO_4 (PPRKTP) crystals. Cristallography. Université Grenoble Alpes; Shandong University (Jinan, Chine), 2018. English. NNT : 2018GREAT042 . tel-01903306

HAL Id: tel-01903306

<https://theses.hal.science/tel-01903306>

Submitted on 24 Oct 2018

HAL is a multi-disciplinary open access archive for the deposit and dissemination of scientific research documents, whether they are published or not. The documents may come from teaching and research institutions in France or abroad, or from public or private research centers.

L'archive ouverte pluridisciplinaire **HAL**, est destinée au dépôt et à la diffusion de documents scientifiques de niveau recherche, publiés ou non, émanant des établissements d'enseignement et de recherche français ou étrangers, des laboratoires publics ou privés.

THÈSE

Pour obtenir le grade de

**DOCTEUR DE LA COMMUNAUTE UNIVERSITE
GRENOBLE ALPES**

**préparée dans le cadre d'une cotutelle entre la
Communauté Université Grenoble Alpes et
Shandong University**

Spécialité : **OPTIQUE ET RADIOFREQUENCES**

Arrêté ministériel : le 6 janvier 2005 – 25 mai 2016

Présentée par

Dazhi LU

Thèse dirigée par **Benoît BOULANGER** et **Patricia SEGONDS**
codirigée par **Huaijin ZHANG** et **Haohai YU**

préparée au sein des **Institut Néel** et **State Key Lab of Crystal
Materials**

dans l'**École Doctorale EEATS** et **Graduate School of
Shandong University**

Propriétés optiques non linéaires quadratiques des cristaux $\text{La}_3\text{Ga}_{5.5}\text{Nb}_{0.5}\text{O}_{14}$ (LGN) et Rb:KTiOPO_4 à domaines ferroélectriques alternés périodiquement (PPRKTP)

Thèse soutenue publiquement le **29 Juin 2018**,
devant le jury composé de :

Monsieur Jean-Louis COUTAZ

Professeur à l'Université de Savoie Mont-Blanc, Président

Monsieur Gérard AKA

Professeur à l'École Nationale Supérieure de Chimie de Paris, Rapporteur

Monsieur Antoine GODARD

Directeur de Recherche à l'ONERA, DMPH, Rapporteur

Monsieur François BALEMBOIS

Professeur à l'Université Paris Sud, Examineur

Monsieur Benoît BOULANGER

Professeur à l'Université Grenoble Alpes, Institut Néel, Directeur de thèse

Madame Patricia SEGONDS

Professeure à l'Université Grenoble Alpes, Institut Néel, Directrice de thèse



Acknowledgements

This thesis was first carried out in Institute of Crystal Materials, Shandong University in China, under the guidance of my Chinese supervisor, Prof. Huaijin Zhang (co-supervisor: Prof. Haohai Yu), and then finished in “Optique et Matériaux” group, Néel Institute in France, under the guidance of my French supervisor, Prof. Benoît Boulanger (co-supervisor: Prof. Patricia Segonds). Thanks to the “co-tutelle” project, I can have this precious opportunity to study in Shandong University and Université Grenoble Alpes.

I would first and foremost like to thank my two supervisors: Prof. Huaijin Zhang and Prof. Benoît Boulanger. It's Prof. Huaijin Zhang who introduced me into the marvelous crystal world, and taught me not only how to do research, but also how to be a better man. It's Prof. Benoît Boulanger who guided me to explore the Palace of “nonlinear optics”, and helped me really a lot to solve all the problems both in academic study and daily life. Prof. Benoît Boulanger is really a strict, careful and hard-working researcher, meanwhile, he is also a patient, tolerant and humorous teacher. Benoît, thanks for all your guidance which is full of life philosophy, like “No news is good news”.

I would also like to thank my co-supervisor Prof. Haohai Yu and Prof. Patricia Segonds. It's Prof. Haohai Yu who supported me tremendously in getting interest in research and conquering the crystal physics world. It's Prof. Patricia Segonds who taught me all the details of the Magic sphere experiment. Her rigorous attitude was stamped in my mind. Meanwhile, I would like to thank Prof. Jiyang Wang for your supports and suggestions these years.

Thanks for all your assistance and kind guidance, my supervisors. I will be grateful all my life and I have spent a really happy time with you.

This work cannot be done without the colleagues' assistance. I would like to express my thankfulness to Feng Guo for helping me with the experiments, to Alexandra Peña for spending time with me in the lab and modifying the paper, to Cyril Bernerd for helping me insert into the lab and "le temps de thé", to Jérôme Debray for your marvelous sphere, to David Jegouso, Véronique Boutou and Corinne Felix for your treatment with the laser source ensuring the success of this experiment. I would also like to express my thankfulness to Qingming Lu, Qiang Fu in Shandong University for the help. Grand merci to all of you.

I would like to thank Chinese Scholarship Council for their financial support.

My life in France was colorful and full of happiness thanks to my dear friends: Shibo Shu, Kewen Shi, Mengyao He, Tianyi Wei, Chaoran Yang, Xiao Xu's family, Weijia Qian, Yining Huang, Panyi Feng, Yi Wang and Jiahao Zuo. Life abroad is tough, but all the problems can be solved with your accompany. Wish you all to be safe abroad and to have a bright future.

Finally, the warmest of my gratitude goes to my parents, my sister, my wife and other family members. Supports without precondition, love without distance. You give me all you have and also the courage for pursuing my dream. Love you.

Let's end with a Chinese saying which is always encouraging me: "No matter how high the mountain is, one can always ascend to its top." (华山再高，顶有过路)

MERCI.

Grenoble, April 2018

Dazhi LU (路大治)

Contents

1	Introduction.....	5
2	Theory.....	8
2.1	Introduction	8
2.2	Linear optical properties	8
2.3	Nonlinear optical properties.....	17
2.3.1	Birefringence phase-matching	23
2.3.2	Angular quasi-phase-matching	24
2.3.3	Acceptances	28
2.3.4	Spatial walk-off.....	30
2.4	Conclusion	32
3	LGN crystal.....	33
3.1	State of the art and motivations.....	33
3.2	Crystallographic structure	34
3.3	Crystal growth.....	35
3.3.1	Introduction.....	35
3.3.2	Chemical composition of the melt for the growth of LGN....	37
3.3.3	Description of the furnace used for our experiments.....	38
3.3.4	Weight control	39
3.3.5	Thermal field.....	41
3.3.6	Growing atmosphere	45

3.3.7	Rotating and pulling rates	45
3.3.8	Summary of the crystal growth technical parameters and produced crystals.....	48
3.4	Linear optical properties	49
3.4.1	Orientation of the dielectric frame.....	49
3.4.2	Transmittance spectra	50
3.4.3	Optical damage threshold	51
3.4.4	Sellmeier equations using the prism method	51
3.5	Nonlinear optical properties	54
3.5.1	Calculations of the birefringence phase-matching conditions and of the corresponding effective coefficients	54
3.5.2	Measurement of the birefringence phase-matching properties and refinement of the Sellmeier equations.....	57
3.5.2.1	Description of the sphere method.....	57
3.5.2.1.1	Introduction	57
3.5.2.1.2	General configuration of the experiment setup.....	58
3.5.2.1.3	Focusing conditions in the sphere.....	60
3.5.2.1.4	The Euler circle.....	62
3.5.2.2	Measured phase-matching angles of Second-Harmonic Generation and Difference-Frequency Generation.....	64
3.5.2.3	Refinement of the Sellmeier equations from the fit of the	

	phase-matching angles	66
3.5.3	Measurements of the nonlinear coefficient d_{11}	67
3.5.3.1	Non-phase-matching measurements	67
3.5.3.2	Phase-matching measurements	71
3.5.3.3	Analysis	76
3.5.4	Calculation of supercontinuum conditions	77
3.6	Summary and discussion	78
4	PPRKTP crystal	82
4.1	State of the art and motivations.....	82
4.2	Theoretical analysis.....	83
4.3	Measurements.....	90
4.4	Results and discussions	96
4.5	Conclusions and perspectives.....	101
5	Conclusion	102
6	References	104
7	Appendix.....	117
-	D. Lu et.al, “Acentric langanite $La_3Ga_{5.5}Nb_{0.5}O_{14}$ crystal: a new nonlinear crystal for the generation of mid-infrared parametric light” <i>Optics Express</i> 24 (16), 17603 (2016);	
-	F. Guo, D. Lu et.al, “Phase-matching properties and refined Sellmeier equations of $La_3Ga_{5.5}Nb_{0.5}O_{14}$ ” <i>Optical Materials Express</i> 8(4), 858 (2018);	
-	D. Lu, et.al, “Validation of the Angular Quasi-Phase-Matching theory for the biaxial optical class using PPRKTP”, <i>Optics Letters</i> , accepted (2018).	

1 Introduction

Nonlinear optics, which has attracted the world's attention since the invention of LASER in 1960, is an important technique for expanding the frequency range of existing laser sources thanks to the excellent coherent properties and the high intensity of the laser. A huge spectral range can be then addressed, from ultraviolet to visible, infrared and even terahertz, so that nowadays nonlinear optics plays vital roles in the fields of medicine, industry, military applications, spectroscopy, and quantum information. During a nonlinear process, phase-matching conditions have to be fulfilled in order to get an optimal frequency conversion efficiency compatible with real applications. There are two main ways for realizing such a condition: the first one is by using anisotropic dispersive crystals and is called birefringence phase-matching (BPM); the other one is based on the periodic modulation of the sign of the second-order nonlinear coefficient of isotropic or anisotropic crystals, which corresponds to quasi-phase-matching (QPM). Reaching BPM or QPM is then a crucial target, but whether BPM or QPM, nonlinear crystals must be of excellent crystal quality, exhibiting large size, high damage threshold and a large transparency range. The present dissertation is at the heart of this problem, since we have addresses materials and phase-matching purposes. We have grown large size $\text{La}_3\text{Ga}_{5.5}\text{Nb}_{0.5}\text{O}_{14}$ (LGN) crystals and evaluated their nonlinear properties in the framework of BPM. This crystal is a promising nonlinear crystal for high energy applications in band II of transmission of the atmosphere, *i.e.* between $3 \mu\text{m}$ and $5 \mu\text{m}$, for Lidar applications for example. Concerning the QPM approach, we have realized the first full validation of the theory of angular QPM (AQPM) in the case of a biaxial crystal, by studying a periodically-poled large-aperture Rb-doped KTiOPO_4 (PPRKTP) crystal.

This work has been performed in the frame work of an international collaboration between Shandong University in China where the LGN crystals were grown, KTH in Sweden where the PPRKTP crystal was poled, and University of Grenoble-Alpes in France where the most parts of the nonlinear theoretical and experimental studies on LGN and PPRKTP were done.

Chapter II gives all the theoretical tools that are necessary for achieving and analyzing our experiments, including the description of light propagation based on the real part of the first-order dielectric permittivity tensor that defines the linear properties, and the basis of second-order nonlinear optics by focusing on BPM and QPM.

Chapter III is devoted to the LGN crystal. Firstly, we introduced the crystal structure and the growth method we used, *i.e.* the Czochralski method, including the description of all the relevant optimization parameters that have to be mastered, and that lead to the LGN crystals we used for the experiments. Secondly, we worked on the linear optical properties of LGN by measuring the transmission spectra in polarized light, the optical damage threshold, as well as the Sellmeier equations. Thirdly, the second-order nonlinear optical properties of LGN have been theoretically evaluated: it includes the BPM conditions and the corresponding effective coefficients of second-harmonic generation (SHG), sum-frequency generation (SFG), and difference-frequency generation (DFG). Finally, the BPM angles of SHG and DFG were directly measured by using the sphere method. Meanwhile, the nonlinear coefficient d_{11} was measured using the Maker Fringes method as well as BPM measurements. All these results proved the strong potentiality of LGN.

Chapter IV reports the first general validation of the AQPM scheme in the

case of a biaxial crystal. The PPRKTP crystal was used because it can be obtained in larger size so that it can be shaped as a sphere. This validation included the calculations and the measurements using the sphere method of the angular distribution of the four SHG AQPM types that are allowed in PPRKTP on the one hand, and of the corresponding effective coefficients on the other hand. The agreement between theory and experiment was perfect, which opens a new and exciting door in nonlinear optics.

The works performed during this thesis led to the three publications given in the Appendix:

- D. Lu, T. Xu, H. Yu, Q. Fu, H. Zhang, P. Segonds, B. Boulanger, X. Zhang, and J. Wang, “Acentric langanite $La_3Ga_{5.5}Nb_{0.5}O_{14}$ crystal: a new nonlinear crystal for the generation of mid-infrared parametric light” *Optics Express* 24 (16), 17603 (2016);
- F. Guo, D. Lu, P. Segonds, J. Debray, H. Yu, H. Zhang, J. Wang, and B. Boulanger, “Phase-matching properties and refined Sellmeier equations of $La_3Ga_{5.5}Nb_{0.5}O_{14}$ ” *Optical Materials Express* 8(4), 858 (2018);
- D. Lu, A. Peña, P. Segonds, J. Debray, S. Joly, F. Laurell, V. Pasiskevicius, H. Yu, H. Zhang, J. Wang, C. Canalias and B. Boulanger, “Validation of the Angular Quasi-Phase-Matching theory for the biaxial optical class using PPRKTP”, *Optics Letters*, accepted (2018).

2 Theory

2.1 Introduction

This chapter presents briefly the theoretical elements which will be used in the next chapters. The first part deals with the linear optical properties, and describes the propagation of light based on the real part of the dielectric permittivity tensor. The second part introduces the basis of nonlinear optics, by focusing on the quadratic parametric phenomena. Two ways for obtaining the maximum parametric generation are specifically described, one is birefringence phase-matching [1], and the other one is angular quasi-phase-matching [2].

2.2 Linear optical properties

When light propagates in a medium, its electric field gives rise to an induced polarization in the medium. This polarization can vary linearly or nonlinearly with the electric field according to the intensity of the exciting electric field.

When the light intensity is lower than around 1 MW/cm², then the induced polarization is written [3]:

$$\vec{P}(\omega) = \epsilon_0 \chi^{(1)}(\omega) \cdot \vec{E}(\omega) \quad (2.1)$$

where ϵ_0 is the free-space permittivity, and $\chi^{(1)}(\omega)$ is the first-order electric susceptibility tensor that is a complex quantity in the general case. The dot “.” stands for the contracted product. It is also a rank-2 tensor, which means that

it is represented by a 3×3 matrix. The present work is limited to transparent media, so that the imaginary part of $\chi^{(1)}(\omega)$ can be neglected.

In a non-conducting and non-magnetic medium, the propagation equation of light at the circular frequency ω is:

$$\vec{\nabla} \times \vec{\nabla} \times \vec{E}(\omega) = \frac{\omega^2}{c^2} \vec{E}(\omega) + \omega^2 \mu_0 \vec{P}(\omega) \quad (2.2)$$

where $\omega = 2\pi c/\lambda$, λ is the wavelength and c is the velocity of light in a vacuum; μ_0 is the free-space permeability. Combined with Eq. (2.1), Eq. (2.2) becomes:

$$\vec{\nabla} \times \vec{\nabla} \times \vec{E}(\omega) - \frac{\omega^2}{c^2} \epsilon_r(\omega) \cdot \vec{E}(\omega) = 0 \quad (2.3)$$

where “ \times ” stands for a vectorial product and “ \cdot ” for the contracted product; $\epsilon_r(\omega)$ is the dielectric permittivity tensor of the crystal defined by $\epsilon_r(\omega) = 1 + \chi^{(1)}(\omega)$. It is then a rank-2 tensor. In the crystal, there is an orthonormal frame, named the dielectric frame written (x, y, z) , in which the dielectric tensor of the medium is diagonal, which gives for the representative matrix:

$$\epsilon_r(\omega) = \begin{bmatrix} \epsilon_{rxx} & 0 & 0 \\ 0 & \epsilon_{ryy} & 0 \\ 0 & 0 & \epsilon_{rzz} \end{bmatrix} \quad (2.4).$$

The axes $(\vec{Ox}, \vec{Oy}, \vec{Oz})$ are the principle axes of the medium. Three situations exist according to the relative values of ϵ_{rxx} , ϵ_{ryy} , and ϵ_{rzz} , which define the three optical classes [4]. The isotropic optical class corresponds to $\epsilon_{rxx} = \epsilon_{ryy} = \epsilon_{rzz}$; it includes gaz, liquids, glasses and cubic crystals. Rhombohedral, tetragonal and hexagonal crystals belong to the uniaxial optical class, which corresponds to $\epsilon_{rxx} = \epsilon_{ryy} \neq \epsilon_{rzz}$. The biaxial optical class is defined by $\epsilon_{rxx} \neq \epsilon_{ryy} \neq \epsilon_{rzz}$ and it concerns monoclinic, triclinic and

orthorhombic crystals. In this work two crystals are studied: LGN and PPRKTP, which belong to the uniaxial and biaxial optical classes, respectively.

The wave plane is a solution of the propagation equation (2.3); it is written [4]:

$$\vec{E}(\omega, \vec{r}, t) = \vec{e}(\omega)E(\omega, \vec{r})\exp[\pm i\vec{k} \cdot \vec{r}]\exp[-i\omega t] \quad (2.5)$$

where \vec{r} is the position, $\vec{e}(\omega)$ is the unit vector of the electric field vector, $E(\omega, \vec{r})$ is the scalar complex amplitude of the electric field verifying $E^*(\omega, \vec{r}) = E(-\omega, \vec{r})$, and \vec{k} is the wave vector that corresponds to the direction of propagation of the wave. In a lossless medium, $+\vec{k} \cdot \vec{r}$ corresponds to a forward propagation whereas $-\vec{k} \cdot \vec{r}$ corresponds to a backward propagation.

When an electromagnetic wave propagates in a given direction of unit vector \vec{u} in an anisotropic medium, with $|\vec{u}(\theta, \varphi)| = 1$, the wave vector can exhibit two different values, $|\vec{k}^+|$ and $|\vec{k}^-|$ corresponding to \vec{k}^+ and \vec{k}^- defined as:

$$\vec{k}^\pm(\omega, \theta, \varphi) = \frac{\omega}{c} n^\pm(\omega, \theta, \varphi) \vec{u}(\theta, \varphi) \quad (2.6)$$

where (θ, φ) are the angles of spherical coordinates of \vec{u} in the dielectric frame (x, y, z) , as presented in Fig. 2.1.

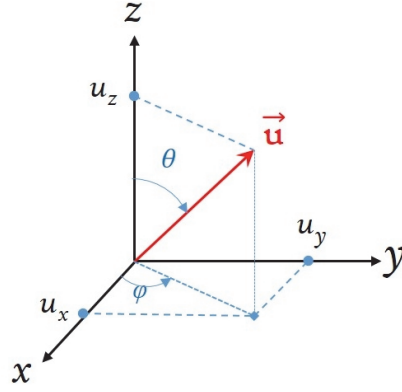


Figure 2.1 Orientation of the direction of propagation \vec{u} in the dielectric frame (x, y, z) : u_x , u_y and u_z are the Cartesian coordinates of \vec{u} while θ and φ are the angles of spherical coordinates.

According to Fig. 2.1, the Cartesian coordinates are related to the angles of spherical coordinates by:

$$\begin{cases} u_x = \sin \theta \cos \varphi \\ u_y = \sin \theta \sin \varphi \\ u_z = \cos \theta \end{cases} \quad (2.7).$$

Starting from the propagation equation (2.3) it can be shown that the refractive index n in a given direction of propagation can be found by solving the following equation at the circular frequency ω , which is called the Fresnel equation [5]:

$$u_x^2 \cdot \epsilon_{rxx} / (\epsilon_{rxx} - n^2) + u_y^2 \cdot \epsilon_{ryy} / (\epsilon_{ryy} - n^2) + u_z^2 \cdot \epsilon_{rzz} / (\epsilon_{rzz} - n^2) = 0 \quad (2.8).$$

This equation has two solutions in the general case, which can be written:

$$n^{\pm}(\omega, \vec{u}) = \left[\frac{2}{-B \mp (B^2 - 4C)^{\frac{1}{2}}} \right]^{\frac{1}{2}}$$

$$\begin{aligned}
 \text{with } B &= -u_x^2(b+c) - u_y^2(a+c) - u_z^2(a+b) \\
 C &= u_x^2bc + u_y^2ac + u_z^2ab \\
 a &= n_x^{-2}(\omega), \quad b = n_y^{-2}(\omega), \quad c = n_z^{-2}(\omega)
 \end{aligned} \tag{2.9}$$

$n_x(\omega)$, $n_y(\omega)$ and $n_z(\omega)$ are the three principal refractive indices. These are scalar quantities defined from the principal values of the dielectric permittivity tensor, i.e.: $n_x^2 = \epsilon_{rxx}$, $n_y^2 = \epsilon_{ryy}$ and $n_z^2 = \epsilon_{rzz}$.

The graphical representation of $n^\pm(\omega, \vec{u})$ is called the index surface, and the quantity $n^+(\omega, \vec{u}) - n^-(\omega, \vec{u})$ is the birefringence of the direction \vec{u} at the circular frequency ω .

In the case of a biaxial crystal, the three principal refractive indices have different magnitudes, i.e. $n_x \neq n_y \neq n_z$. The corresponding index surface is represented Fig. 2.2 in the two possible situations: $n_x < n_y < n_z$, which defines what is called a positive biaxial crystal, and $n_x > n_y > n_z$ that corresponds to a negative biaxial crystal [4].

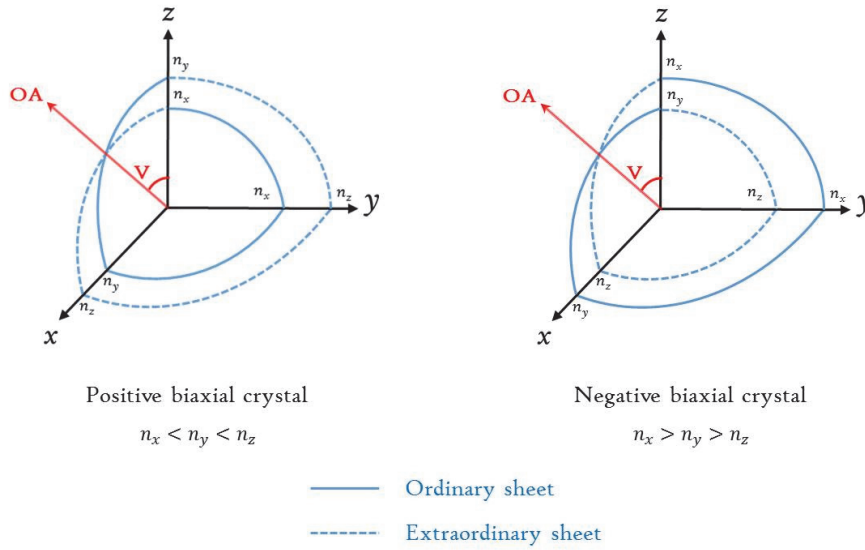


Figure 2.2 The index surface of a positive (left) and a negative (right) biaxial crystal represented in $1/8$ of the space. OA stands for an optical axis.

Note that the principal axes of the index surface coincide with the crystallographic axes for the orthorhombic, tetragonal and cubic crystal systems. It is only the case for one principal axis, which is the z axis by convention, in rhombohedral and hexagonal crystal systems. It is also true for one principal axis in the monoclinic system, but the two other axes are not connected. There is no connection between the principal axes and the crystallographic axes in the case of triclinic systems [6].

Figure 2.2 indicates that the birefringence is nil in a given direction located in the (x, z) plane; it is called the optical axis (OA). Along this direction there is a contact between the external and internal layer of the index surface. This specific point of the space is called the ombilic. There are in fact 4 ombilics lying in the (x, z) plane, which give two optical axes, each joining two opposite ombilics. It is why such a crystal is called biaxial. The angle V between OA and the z axis is expressed as [4]:

$$\sin^2 V(\omega) = \frac{n_y^{-2}(\omega) - n_x^{-2}(\omega)}{n_z^{-2}(\omega) - n_x^{-2}(\omega)} \quad (2.10)$$

The propagation of light along the optic axes leads to a nice phenomenon that is the internal conical refraction [7, 8]. It exists only in biaxial crystals.

In the case of a uniaxial crystal, the principal refractive indices verify $n_x = n_y \neq n_z$. By convention, they are defined as the ordinary and the extraordinary principal refractive indices n_o and n_e , respectively: $n_o = n_x = n_y$ and $n_e = n_z$. In that case, the index surface has only two ombilics located along the z axis as shown in Fig. 2.3. These two ombilics then define a

single optical axis, which explains why such a crystal is called uniaxial. Note that the optical axis is always oriented along the crystallographic fold rotation axis of higher order. The ordinary sheet is spherical, *i.e.* $n_o(\omega, \theta, \varphi) = n_o(\omega)$ for any direction. The extraordinary sheet is ellipsoidal, *i.e.* $n_e(\omega, \theta, \varphi) = [\cos^2\theta/n_o^2(\omega) + \sin^2\theta/n_e^2(\omega)]^{-1/2}$. By convention a uniaxial optical class is said positive when $n_o < n_e$, and negative when $n_o > n_e$, as shown in Fig. 2.3.

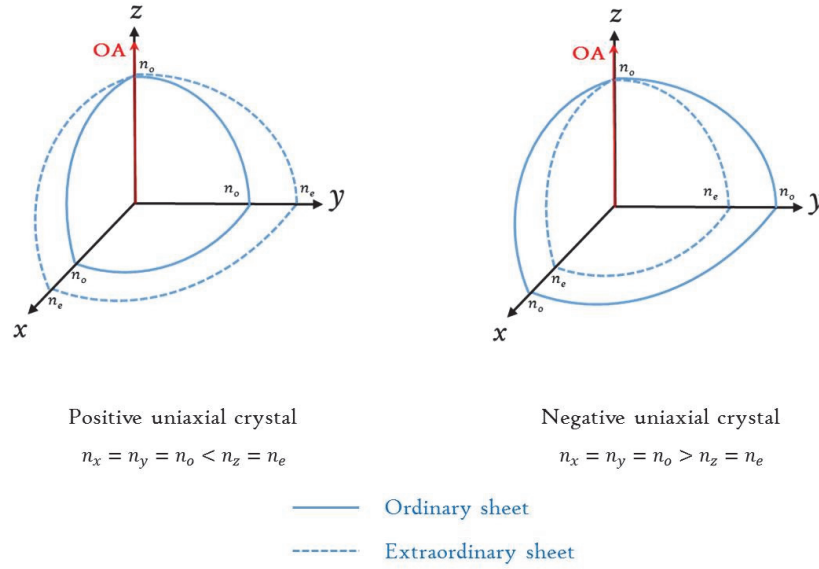


Figure 2.3 The index surface of a positive (left) and a negative (right) uniaxial crystal. OA is the optical axis.

The vector configuration of the fields when light propagates in an anisotropic medium is presented in Fig. 2.4. The frame (X, Y, Z) is a laboratory frame, where the Z axis corresponds to the propagation direction. Note that this frame is different than the dielectric frame (x, y, z) . The orthogonal vibration planes Π^\pm [9] are the planes containing the dielectric displacements \vec{D}^\pm , the electric fields \vec{E}^\pm , the Poynting vectors \vec{S}^\pm given by $\vec{S}^\pm = \vec{E}^\pm \times \vec{H}^\pm$ (\vec{H}^\pm being the magnetic field) and the wave vectors \vec{k}^\pm .

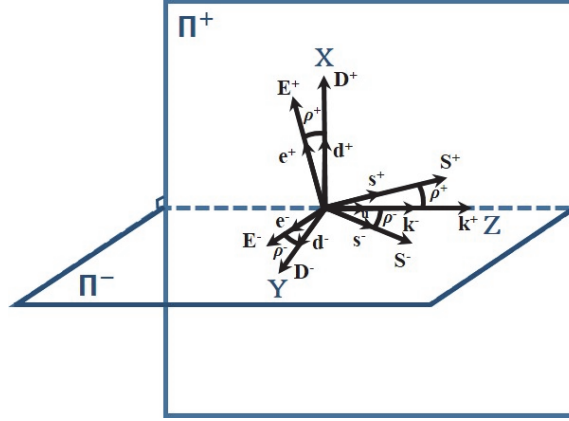


Figure 2.4 Vector configuration of an electromagnetic wave propagating in an anisotropic medium [4]. The angles ρ^\pm are called the walk-off angles.

The power density, also called the intensity, is expressed as follows [3]:

$$\|\vec{S}^\pm(\omega)\| = \frac{\|\vec{k}^\pm(\omega)\|}{2\mu_0\omega} \|\vec{E}^\pm(\omega)\|^2 \cos^2[\rho(\omega)] \quad (2.11).$$

According to Fig. 2.4, the walk-off angles can be defined as: $\rho^\pm = \arccos(\vec{d}^\pm \cdot \vec{e}^\pm) = \arccos(\vec{u}^\pm \cdot \vec{s}^\pm)$, where \vec{s} and \vec{d} are the unit vectors associated with \vec{S} and \vec{D} , respectively. The walk-off angles ρ^\pm in a direction of propagation α located in the principal plane (u, v) is written [10]:

$$\rho_{uv}(\alpha, \omega) = \arccos\left(\frac{[n_v^2(\omega)/n_u^2(\omega)]\cos^2\alpha + \sin^2\alpha}{\sqrt{[n_v^4(\omega)/n_u^4(\omega)]\cos^2\alpha + \sin^2\alpha}}\right) \quad (2.12)$$

with, for biaxial crystals: $(u, v) = (x, z)$ and $\alpha = \theta$ in the principal plane (x, z) , $(u, v) = (y, z)$ and $\alpha = \theta$ in the principal plane (y, z) , and $(u, v) = (y, x)$ and $\alpha = \varphi$ in the principal plane (x, y) ; and for uniaxial crystals, the angle ρ is equal to zero in the plane (x, y) , whereas $(u, v) = (o, e)$ and $\alpha = \theta$ in the planes (x, z) and (y, z) . Equation (2.12) shows that in the case of biaxial crystals, the walk-off angle is nil only along a principal axis of the index surface.

Out of the principal planes of biaxial crystals, and when projecting the direction of propagation onto the three principal axes, it is possible to calculate the three Cartesian coordinates (e_x, e_y, e_z) of the unit electric field vectors \vec{e}^\pm as a function of the three Cartesian coordinates (u_x, u_y, u_z) of the unit wave vector from [9]:

$$e_i^\pm(\omega, \theta, \varphi) - u_i(\theta, \varphi)[\vec{u}(\theta, \varphi) \cdot \vec{e}^\pm(\omega, \theta, \varphi)] = \frac{[n_i(\omega)]^2 e_i^\pm(\omega, \theta, \varphi)}{[n^\pm(\omega, \theta, \varphi)]^2} \quad (2.13)$$

with $(e_x^\pm)^2 + (e_y^\pm)^2 + (e_z^\pm)^2 = 1$, $n^\pm(\omega, \theta, \varphi)$ corresponds to the refractive index given by Eq. (2.9), whereas $n_i(\omega)$ stands for the principal refractive indices with $i = x, y$ and z .

In the two principal planes (y, z) , where $\varphi = 90^\circ$, and (x, z) at $\theta > V_Z$ and $\varphi = 0^\circ$, of a positive biaxial crystal as PPRKTP, the unit electric field vectors $\vec{e}^\pm(\omega, \theta, \varphi)$ are given by [4]:

$$\vec{e}^-(\varphi) = \begin{pmatrix} e_x^- \\ e_y^- \\ e_z^- \end{pmatrix} = \begin{pmatrix} -\sin\varphi \\ \cos\varphi \\ 0 \end{pmatrix} \quad (2.14)$$

$$\vec{e}^+(\omega, \theta, \varphi) = \begin{pmatrix} e_x^+ \\ e_y^+ \\ e_z^+ \end{pmatrix} = \begin{pmatrix} -\cos[\theta - \rho(\omega, \theta)]\cos\varphi \\ -\cos[\theta - \rho(\omega, \theta)]\sin\varphi \\ \sin[\theta - \rho(\omega, \theta)] \end{pmatrix} \quad (2.15).$$

In the (x, z) plane at $\theta < V_Z$ where $\varphi = 0^\circ$, Eq. (2.15) is valid, while $\vec{e}^-(\varphi)$ is given by:

$$\vec{e}^-(\varphi) = \begin{pmatrix} e_x^- \\ e_y^- \\ e_z^- \end{pmatrix} = \begin{pmatrix} 0 \\ -1 \\ 0 \end{pmatrix} \quad (2.16)$$

In the (x, y) plane, where $\theta = 90^\circ$, the components of the electric field can be written as follows:

$$\vec{e}^-(\omega, \varphi) = \begin{pmatrix} e_x^- \\ e_y^- \\ e_z^- \end{pmatrix} = \begin{pmatrix} -\sin[\varphi + \rho(\omega, \varphi)] \\ \cos[\varphi + \rho(\omega, \varphi)] \\ 0 \end{pmatrix} \quad (2.17)$$

$$\vec{e}^+ = \begin{pmatrix} e_x^+ \\ e_y^+ \\ e_z^+ \end{pmatrix} = \begin{pmatrix} 0 \\ 0 \\ 1 \end{pmatrix} \quad (2.18)$$

In a positive uniaxial crystal as LGN, the unit field vector $\vec{e}^-(\omega, \theta, \varphi)$ and $\vec{e}^+(\omega, \theta, \varphi)$ can be established by the Eqs. (2.14) and (2.15), respectively. Note that in uniaxial crystals and in the principal planes of biaxial crystals, $\vec{e}^-(\varphi) \cdot \vec{e}^+(\omega, \theta, \varphi) = 0$ is always fulfilled according to the previous equations. But \vec{e}^- and \vec{e}^+ are not perpendicular out of the principal planes of biaxial crystals.

2.3 Nonlinear optical properties

When the power density of the electric field of light is bigger than about 1 MW/cm², the nonlinear optical effects can be detected. In this work, we will focus on the interaction among three electromagnetic waves at the circular frequencies ω_1 , ω_2 , and ω_3 . In this process, the frequencies fulfill the energy conservation:

$$\hbar\omega_1 + \hbar\omega_2 = \hbar\omega_3 \quad (2.17).$$

Then each of the Fourier components ω_i (with $i = 1, 2, 3$) of the induced polarization can be developed up to the second order as [1, 11]:

$$\vec{P}(\omega_i) = \epsilon_0 \chi^{(1)}(\omega_i) \cdot \vec{E}(\omega_i) + \vec{P}^{(2)}(\omega_i) \quad (2.18)$$

$\vec{P}^{(2)}(\omega_i)$ is the second order nonlinear polarization defined by:

$$\begin{cases} \vec{P}^{(2)}(\omega_1) = \epsilon_0 \chi^{(2)}(\omega_1) : \vec{E}(\omega_3) \otimes \vec{E}^*(\omega_2) \\ \vec{P}^{(2)}(\omega_2) = \epsilon_0 \chi^{(2)}(\omega_2) : \vec{E}(\omega_3) \otimes \vec{E}^*(\omega_1) \\ \vec{P}^{(2)}(\omega_3) = \epsilon_0 \chi^{(2)}(\omega_3) : \vec{E}(\omega_1) \otimes \vec{E}(\omega_2) \end{cases} \quad (2.19)$$

where “.” and “:” are the contracted products and “ \otimes ” is the tensor product. $\chi^{(2)}(\omega_i)$ is the so-called second-order electric susceptibility tensor. It is a rank-3 tensor, so that its representative matrix has 3×9 coefficients, i.e. [4]:

$$\chi^{(2)}(\omega) = \begin{pmatrix} \chi_{xxx} & \chi_{xyy} & \chi_{xzz} & \chi_{xyz} & \chi_{xzy} & \chi_{xxz} & \chi_{xzx} & \chi_{xxy} & \chi_{xyx} \\ \chi_{yxx} & \chi_{yyy} & \chi_{yzz} & \chi_{yyz} & \chi_{yzy} & \chi_{yxz} & \chi_{yzx} & \chi_{yxy} & \chi_{yyx} \\ \chi_{zxx} & \chi_{zyy} & \chi_{zzz} & \chi_{zyz} & \chi_{zzy} & \chi_{zxz} & \chi_{zzx} & \chi_{zxy} & \chi_{zyx} \end{pmatrix} \quad (2.20)$$

where x, y and z refer to the dielectric frame. Each of the 27 coefficients depends on ω but it is not written in the matrix for more clarity. Neumann’s principle allows some coefficients to be equal to zero, and other coefficients to have equal or opposite magnitudes [6]. Furthermore, in the cases of low absorption and low dispersion of the wavelength of the electric susceptibility, so-called Kleinman’s conditions, the number of non-zero elements among the tensors can be also reduced because tensor $\chi^{(2)}$ becomes fully symmetrical, i.e. $\chi_{ijk} = \chi_{ikj} = \chi_{jik} = \chi_{jki} = \chi_{kij} = \chi_{kji}$, where $i, j, k = x, y$ or z [11]. The tensor $\chi^{(2)}$ of the two crystals studied in the present work will be given in the corresponding chapters.

Three nonlinear process can occur according to Eqs. (2.17) and (2.19): the difference-frequency generation (DFG) between ω_3 and ω_2 giving birth to a

wave at $\omega_1 = \omega_3 - \omega_2$, the DFG between ω_3 and ω_1 leading to $\omega_2 = \omega_3 - \omega_1$, and the sum-frequency generation (SFG) leading to $\omega_3 = \omega_1 + \omega_2$. The degenerate SFG, i.e. $\omega_1 = \omega_2 (= \omega)$ is called second-harmonic generation (SHG), which corresponds to $\omega_3 = 2\omega = \omega + \omega$.

The propagation equation of each interacting electromagnetic wave can be obtained from Eqs. (2.2) and (2.18), which gives:

$$\vec{\nabla} \times \vec{\nabla} \times \vec{E}(\omega_i) - \frac{\omega_i^2}{c^2} \epsilon_r(\omega_i) \cdot \vec{E}(\omega_i) = \omega_i^2 \mu_0 \vec{P}^{(2)}(\omega_i) \quad (2.21)$$

where $i = 1, 2, 3$.

This is the second-order nonlinear equation of propagation that differs from the first-order linear equation of propagation given by Eq. (2.3) due to a non-zero term on the right side depending on $\vec{P}^{(2)}(\omega_i)$. By combining Eqs. (2.19) and (2.21), and by assuming the slowly variable envelope approximation, it is possible to establish the following system of coupled differential equations [12]:

$$\begin{cases} \frac{\partial E(\omega_1, Z)}{\partial Z} = j\kappa_1 \chi_{eff} E(\omega_3, Z) E^*(\omega_2, Z) \exp(j\Delta k Z) \\ \frac{\partial E(\omega_2, Z)}{\partial Z} = j\kappa_2 \chi_{eff} E(\omega_3, Z) E^*(\omega_1, Z) \exp(j\Delta k Z) \\ \frac{\partial E(\omega_3, Z)}{\partial Z} = j\kappa_3 \chi_{eff} E(\omega_1, Z) E(\omega_2, Z) \exp(-j\Delta k Z) \end{cases} \quad (2.22)$$

Z is the space coordinate in the direction of propagation, i.e. the Z axis of the laboratory frame defined above. $E(\omega_i, Z)$ with $i = 1, 2, 3$ stands for the complex wave amplitudes, $\kappa_i = (\mu_0 \omega_i^2) / [2k(\omega_i) \cos^2 \rho(\omega_i)]$, and $\Delta k = k(\omega_3, \theta, \varphi) - k(\omega_1, \theta, \varphi) - k(\omega_2, \theta, \varphi)$ when the interacting waves are collinear.

The quantity $\Delta k \cdot Z$ corresponds to the phase shift between the nonlinear

polarization $\vec{P}^{(2)}(\omega_i)$ and the electric field $\vec{E}(\omega_i)$ radiated by the nonlinear polarization itself. χ_{eff} is the effective coefficient, which depends on the linear and nonlinear optical properties. Actually in the direction of propagation $\vec{u}(\theta, \varphi)$, it is expressed as [4]:

$$\begin{aligned}\chi_{\text{eff}}(\theta, \varphi) &= \vec{e}_1^\pm(\omega_1, \theta, \varphi) \cdot \chi^{(2)}(\omega_1 = \omega_3 - \omega_2): \vec{e}_3^\pm(\omega_3, \theta, \varphi) \otimes \vec{e}_2^\pm(\omega_2, \theta, \varphi) \\ &= \vec{e}_2^\pm(\omega_2, \theta, \varphi) \cdot \chi^{(2)}(\omega_2 = \omega_3 - \omega_1): \vec{e}_3^\pm(\omega_3, \theta, \varphi) \otimes \vec{e}_1^\pm(\omega_1, \theta, \varphi) \\ &= \vec{e}_3^\pm(\omega_3, \theta, \varphi) \cdot \chi^{(2)}(\omega_3 = \omega_1 + \omega_2): \vec{e}_1^\pm(\omega_1, \theta, \varphi) \otimes \vec{e}_2^\pm(\omega_2, \theta, \varphi)\end{aligned}\quad (2.23).$$

In the framework of the present study, it is interesting to write $\chi_{\text{eff}}(\theta, \varphi)$ as following [4]:

$$\begin{aligned}\chi_{\text{eff}}(\theta, \varphi) &= \sum_{jik} F_{jik}(\omega_3, \omega_1, \omega_2, \theta, \varphi) \chi_{jik}(\omega_1) \\ &= \sum_{kij} F_{kij}(\omega_3, \omega_1, \omega_2, \theta, \varphi) \chi_{kij}(\omega_2) \\ &= \sum_{ijk} F_{ijk}(\omega_3, \omega_1, \omega_2, \theta, \varphi) \chi_{ijk}(\omega_3)\end{aligned}\quad (2.24).$$

The three terms of this equation corresponds from top to bottom to DFG(ω_1), DFG(ω_2) and SFG(ω_3). The coefficients $F_{ijk}(\omega_3, \omega_1, \omega_2, \theta, \varphi)$ are those of a rank-3 tensor that is called the field tensor: it has 27 coefficients as for $\chi^{(2)}$, but contrary to $\chi^{(2)}$ it depends on the direction of propagation. The field tensor F is built from the unit electric field of the three interacting waves. It is defined by [13]:

$$F_{ijk}(\omega_3, \omega_1, \omega_2, \theta, \varphi) = e_i^\pm(\omega_3, \theta, \varphi) e_j^\pm(\omega_1, \theta, \varphi) e_k^\pm(\omega_2, \theta, \varphi)\quad (2.25)$$

where e_i^\pm , e_j^\pm , e_k^\pm are three Cartesian coordinates of the unit electric field vectors expressed in the dielectric frame (x, y, z) by Eq. (2.13). Note that the notation $d_{\text{eff}} = \chi_{\text{eff}}/2$ is also used.

The general solutions $E(\omega_i, Z)$ of Eqs. (2.22) are Jacobi's elliptic functions [12]. The solutions are simplified under the undepleted pump approximation. In the case of SFG for example and in the direction of propagation at the angles of spherical coordinates (θ, φ) , it comes:

$$\begin{cases} E(\omega_1, Z) = E(\omega_1, 0) \\ E(\omega_2, Z) = E(\omega_2, 0) \\ E(\omega_3, Z) = 2j\kappa_3 d_{\text{eff}}(\omega_3, \theta, \varphi) E(\omega_1, 0) E(\omega_2, 0) \int_0^Z \exp(-j\Delta k(\theta, \varphi)Z) dZ \end{cases} \quad (2.26)$$

Then the power $\mathbf{P}(\omega_3, Z)$ generated at ω_3 is expressed as [11]:

$$\mathbf{P}(\omega_3, Z) = \frac{(2N-1)72\pi}{N} \frac{A}{\varepsilon_0 c \lambda_1 \lambda_2} G(Z, w_0, \rho) d_{\text{eff}}^2(\theta, \varphi) \mathbf{P}(\omega_1, 0) \mathbf{P}(\omega_2, 0) \frac{Z^2}{w_0^2} \text{sinc}^2\left(\frac{\Delta k(\theta, \varphi)Z}{2}\right) \quad (2.27)$$

N is the number of longitudinal modes of the incident beams. $\mathbf{P}(\omega_1, 0)$ and $\mathbf{P}(\omega_2, 0)$ are the power of the incident beams, and $\lambda_i = 2\pi c/\omega_i$ ($i = 1$ or 2) are the corresponding wavelengths. $G(Z, w_0, \rho)$, which will be detailed hereafter in § 2.3.4, is the attenuation coefficient due to spatial walk-off where Z is the interaction length and w_0 is the radius of the two incident fields. The quantity A is defined as:

$$A = \frac{T^\pm(\omega_3, \theta, \varphi) T^\pm(\omega_1, \theta, \varphi) T^\pm(\omega_2, \theta, \varphi)}{n^\pm(\omega_3, \theta, \varphi) n^\pm(\omega_1, \theta, \varphi) n^\pm(\omega_2, \theta, \varphi)} \quad (2.28)$$

where $T^\pm(\omega_i, \theta, \varphi)$ ($i = 1, 2, 3$) stands for the Fresnel coefficient at ω_i given by

$T^\pm(\omega_i, \theta, \varphi) = 4n^\pm(\omega_i, \theta, \varphi)/(n^\pm(\omega_i, \theta, \varphi) + 1)^2$, $n^\pm(\omega_i, \theta, \varphi)$ being the refractive index given by Eq. (2.9) [4]. Then the notation $\text{sinc}(u)$ corresponds to the cardinal sinus function.

Figure 2.5 shows the generated power as a function of the interaction length Z . When $\Delta k \neq 0$, the power oscillates. The half-period of oscillation is called the coherence length of the parametric process L_c that is considered, and it is equal to $\pi/\Delta k$ according to Eq. (2.27). In this case, the interference between the nonlinear polarization and the radiated field is destructive due to a phase-mismatch of Δk . In particular, this dephasing is equal to π at each coherence length L_c . At the opposite, the interference is constructive when $\Delta k = 0$ since the function sinc^2 is equal to 1 so that the generated power grows continuously and is proportional to Z^2 .

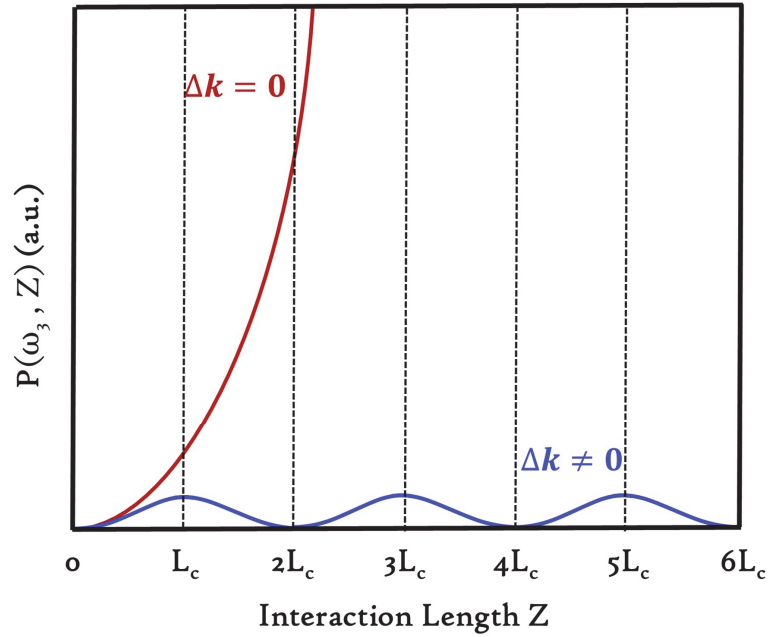


Figure 2.5 Evolution of the power $P(\omega_3, Z)$ generated by SFG as a function of the interaction length Z in the medium in the case of non phase-matching ($\Delta k \neq 0$) and phase-matching ($\Delta k = 0$). L_c is the coherence length of the SFG.

The power conversion efficiency $\eta(\omega_3, Z)$ is defined by the ratio between generated power at ω_3 and the incident powers at ω_1 and ω_2 , i.e.:

$$\eta(\omega_3, Z) = \frac{P(\omega_3, Z)}{P(\omega_1, 0) + P(\omega_2, 0)} \quad (2.29).$$

2.3.1 Birefringence phase-matching

As seen in the previous section, the power transfer between the interacting waves is maximum when the nonlinear polarization is phase-matched with the radiation field, i.e. when $\Delta k = 0$. It corresponds to the momentum conservation from the quantum point of view, which gives when the three photons propagate collinearly in the same direction $\vec{u}(\theta, \varphi)$:

$$k^\pm(\omega_3, \theta, \varphi) - k^\pm(\omega_1, \theta, \varphi) - k^\pm(\omega_2, \theta, \varphi) = 0 \quad (2.30)$$

with

$$k^\pm(\omega_i, \theta, \varphi) = \omega_i n^\pm(\omega_i, \theta, \varphi) / c \quad (2.31)$$

Then the phase-matching relation (2.30) can be written:

$$\frac{n^\pm(\omega_3, \theta, \varphi)}{\lambda_3} - \frac{n^\pm(\omega_1, \theta, \varphi)}{\lambda_1} - \frac{n^\pm(\omega_2, \theta, \varphi)}{\lambda_2} = 0 \quad (2.32).$$

There exist 2^3 possibilities for solving Eq. (2.32) [4]. Among these combinations, only three are possible, which are named Types I, II and III according to the polarization states of the three waves. They are presented in the following Table 2.1 [14].

Table 2.1 Definitions of the different possible phase-matching relations and interaction types related to sum-frequency generation (SFG) and difference-frequency generation (DFG). n_i^\pm stands for the refractive index at the circular frequency ω_i .

Phase-matching relations	Interaction types		
	SFG (ω_3)	DFG (ω_1)	DFG (ω_2)
$\omega_3 n_3^- = \omega_1 n_1^+ + \omega_2 n_2^+$	I	II	III
$\omega_3 n_3^- = \omega_1 n_1^- + \omega_2 n_2^+$	II	III	I
$\omega_3 n_3^- = \omega_1 n_1^+ + \omega_2 n_2^-$	III	I	II

Note that types II and III are equivalent for a SHG process since $\omega_1 = \omega_2$, and it will be then named type II SHG.

Table 2.1 shows that the interacting waves have to exhibit different polarization states, which can exist only when there is a birefringence in the direction of propagation. It is why this phase-matching scheme is called birefringence phase-matching (BPM).

2.3.2 Angular quasi-phase-matching

Quasi-phase-matching (QPM) is another configuration that allows the nonlinear conversion efficiency to be improved. It is based on a periodic reversal of the sign of the effective coefficient at each coherence length of the parametric process that is considered, as shown in Fig. 2.6. Then this artificial structure enables a periodic reset of π between the nonlinear polarization and the radiated field, leading to a periodic phasing [12].

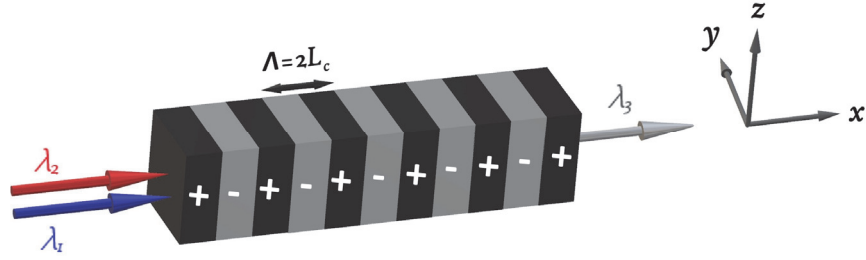


Figure 2.6 Scheme of SFG QPM where the periodic reversal of sign of the effective coefficient is produced along the x-axis of the dielectric frame: “+” and “-” stand for $+\chi_{\text{eff}}$ and $-\chi_{\text{eff}}$, respectively. λ_1 and λ_2 are the wavelengths of the two incident beams. λ_3 is the generated wavelength by SFG. Λ is the periodicity of the structure.

By this way, the constructive interference can be kept along the propagation direction because of the periodic reset of phase, as presented in Fig. 2.7.

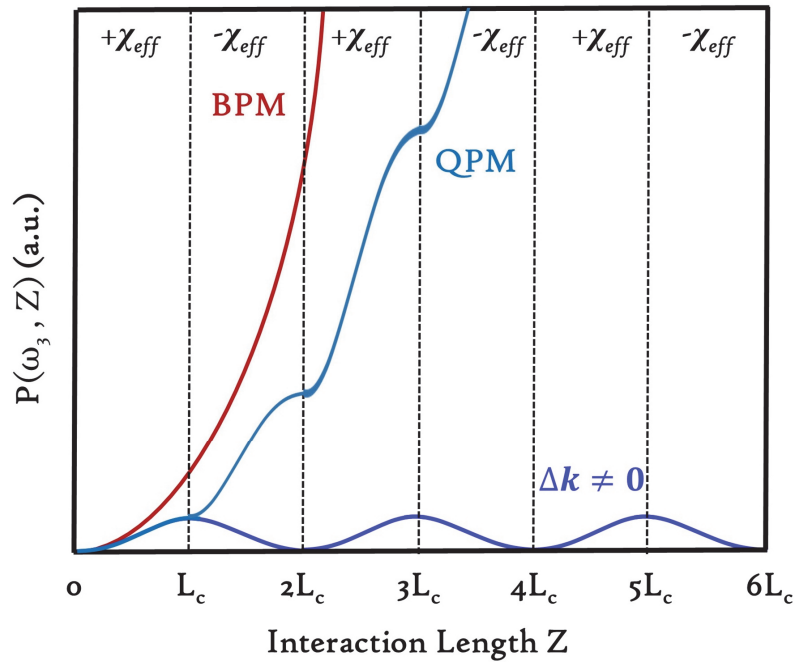


Figure 2.7 Generated power $P(\omega_3, Z)$ as a function of the interaction length Z in the cases of non phase-matching condition ($\Delta k \neq 0$), birefringence phase-matching (BPM) and quasi-phase-matching (QPM). χ_{eff} is the effective coefficient and L_c the coherence length.

When the crystal that is considered has ferroelectric properties, the sign of the effective coefficient can be obtained by the application of an electric field. Then the resulting material is said “periodically-poled”. It is the case of the periodically-poled LiNbO₃ (PPLN) [15] or the periodically-poled KTiOPO₄ (PPKTP) [16] that is considered in this work. When the crystal is not a ferroelectric one, the reversal of the sign can be obtained during the crystal growth or *a posteriori* by bonding. It is the case of the Orientation-Pattern-GaAs (OP-GaAs) [17] or -GaP (OP-GaP) [18].

In all these artificial materials, the grating vector is directly implicated in the momentum conservation that writes in a collinear configuration of propagation [1]:

$$k^{\pm}(\omega_3, \theta, \varphi) - k^{\pm}(\omega_1, \theta, \varphi) - k^{\pm}(\omega_2, \theta, \varphi) - \frac{2\pi}{\Lambda} = 0 \quad (2.33).$$

It can be demonstrated that the power of the wave generated in a QPM configuration is lower by a factor of $4/\pi^2$ compared to the power generated by BPM, as shown in Fig. 2.7.

There are 2^3 possible configurations of polarization for achieving QPM, when BPM have only 3 of them [2]. All the 8 possibilities are shown in Table 2.2.

Table 2.2 Definitions of the different quasi-phase-matching relations and interaction types related to sum-frequency generation (SFG) and difference-frequency generation

(DFG). n_i^{\pm} stands for the refractive index at the circular frequency ω_i .

Quasi-Phase-matching relations	Interaction types		
	SFG (ω_3)	DFG (ω_1)	DFG (ω_2)
$\omega_3 n_3^- = \omega_1 n_1^+ + \omega_2 n_2^+ + 1/\Lambda$	I	II	III
$\omega_3 n_3^- = \omega_1 n_1^- + \omega_2 n_2^+ + 1/\Lambda$	II	III	I
$\omega_3 n_3^- = \omega_1 n_1^+ + \omega_2 n_2^- + 1/\Lambda$	III	I	II
$\omega_3 n_3^- = \omega_1 n_1^- + \omega_2 n_2^- + 1/\Lambda$	IV	IV	IV
$\omega_3 n_3^+ = \omega_1 n_1^+ + \omega_2 n_2^+ + 1/\Lambda$	V	V	V
$\omega_3 n_3^+ = \omega_1 n_1^- + \omega_2 n_2^+ + 1/\Lambda$	VI	VIII	VII
$\omega_3 n_3^+ = \omega_1 n_1^+ + \omega_2 n_2^- + 1/\Lambda$	VII	VI	VIII
$\omega_3 n_3^+ = \omega_1 n_1^- + \omega_2 n_2^- + 1/\Lambda$	VIII	VII	VI

A generalization of QPM has been proposed by the group of Grenoble [2]. It consists in the propagation of three interacting electromagnetic waves at any angle with respect to the grating vector. This configuration is called angular quasi-phase-matching (AQPM) [2, 19]. The scheme of AQPM is shown in Fig. 2.8, where $\vec{u}(\theta, \varphi)$ represents any direction of propagation expressed as a function of the angles of spherical coordinates (θ , φ) in the dielectric frame.

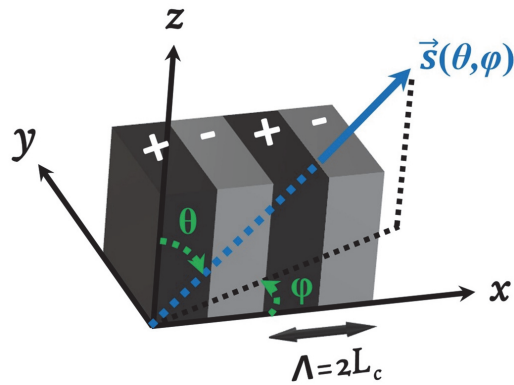


Figure 2.8 Scheme of AQPM where the grating vector of modulus Λ lies along the x axis of the dielectric frame (x, y, z). \vec{u} is the unit wave vector that is the same for the three interacting waves.

In the AQPM configuration, the periodicity, written Λ_{eff} , can vary as a function of the direction of propagation as following [2]:

$$\Lambda_{\text{eff}}(\theta, \varphi) = \frac{\Lambda}{|\sin \theta \cos \varphi|} \quad (2.34).$$

Thus the momentum conservation corresponding to AQPM can be expressed as:

$$k^{\pm}(\omega_3, \theta, \varphi) - k^{\pm}(\omega_1, \theta, \varphi) - k^{\pm}(\omega_2, \theta, \varphi) - \frac{2\pi}{\Lambda_{\text{eff}}(\theta, \varphi)} = 0 \quad (2.35)$$

where $\Lambda_{\text{eff}}(\theta, \varphi)$ is the effective periodicity defined by Eq. (2.34).

About the phase-matching types, AQPM exhibits the same 8 possible combinations of polarizations than that of QPM presented in Table 2.2.

2.3.3 Acceptances

As presented in Eq. 2.27, the interference function $\text{sinc}^2(\Delta k Z/2)$ reaches a maximum value when $\Delta k = 0$, which can be obtained by BPM, QPM as well as AQPM. It occurs in a particular direction of propagation of spherical coordinates written $(\theta_{PM}, \varphi_{PM})$ and a given set of wavelengths $(\lambda_1^{PM}, \lambda_2^{PM}, \lambda_3^{PM})$, where PM stands for BPM, QPM or AQPM.

It is important to know the effect of the variation of Δk (ζ_{PM}) from the value 0, due to variations in angle, $(\theta_{PM} \pm \Delta\theta_{PM}, \varphi_{PM} \pm \Delta\varphi_{PM})$, or in wavelengths $(\lambda_i^{PM} \pm \Delta\lambda_i^{PM})$ with $i = (1, 2, 3)$, from either sides of the phase-matching point $(\theta_{PM}, \varphi_{PM}, \lambda_i^{PM})$ [4]. It will be studied at the output of the crystal *i.e.* at $Z = L$ where L is the crystal length. The corresponding variation given by the normalized generated power with respect to its maximum value as

a function of ζ is shown in Fig. 2.9, where $\zeta = \theta, \varphi, \lambda$. The acceptance bandwidth is then defined by the deviation value $\delta\zeta$, corresponding to the width at 0.405 of the maximal value of the function represented in Fig. 2.9. Meanwhile, it is also the variation of Δk from 0 to $2\pi/L$, i.e. $\delta\zeta = \zeta_{2\pi/L}$ (see Fig. 2.9).

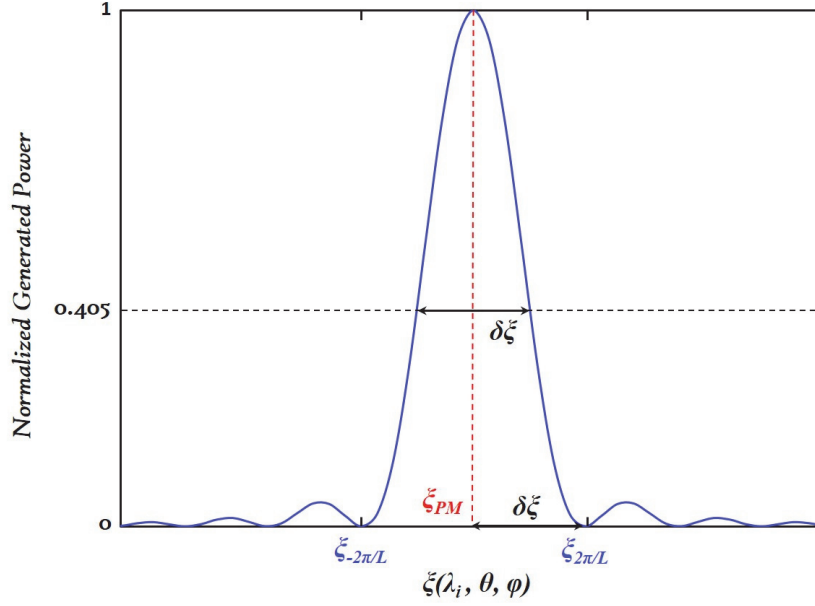


Figure 2.9 Normalized generated power as a function of the dispersive parameter $\xi = \lambda, \theta$ or φ of the refractive indices. $\delta\xi$ is the width of the curve at 0.405 of the maximal value. $\xi_{\pm 2\pi/L}$ corresponds to ξ for which $\Delta k = \pm 2\pi/L$.

The acceptance bandwidth is usually calculated by writing Δk in the form of a Taylor series about ξ [4], i.e.:

$$\Delta k(\xi_{PM}) = \frac{2\pi}{L} = \delta\xi \left. \frac{\partial \Delta k}{\partial \xi} \right|_{\xi=\xi_{PM}} + \frac{1}{2} (\delta\xi)^2 \left. \frac{\partial^2 \Delta k}{\partial \xi^2} \right|_{\xi=\xi_{PM}} + \dots \quad (2.36)$$

In the case where the first-order term is dominating, the phase-matching is called “critical” and the acceptance $L\delta\xi$ is written as:

$$L\delta\xi = \frac{2\pi}{\left. \frac{\partial\Delta k}{\partial\xi} \right|_{\xi=\xi_{PM}}} \quad (2.37).$$

When the first order term is zero, then the second-order one dominates, the phase-matching is called non-critical (NCPM). Under this condition, $L\delta\xi$ is written as:

$$L\delta\xi = \sqrt{\frac{4\pi L}{\left. \frac{\partial^2\Delta k}{\partial\xi^2} \right|_{\xi=\xi_{PM}}}} \quad (2.38).$$

A NCPM situation will be preferred to a critical (CPM) phase-matching, in order to maximize the conversion efficiency regarding the divergence or the spectral linewidth of the incident beams. Actually, the ideal situation is when the angular acceptances and the wavelength acceptance are larger than the incident beams divergence and the spectral linewidth respectively.

2.3.4 Spatial walk-off

When propagating the waves in an optically anisotropic crystal, the effect of the double refraction angle $\rho(\omega, \theta, \varphi)$ must be taken into account and it may affect the amount of the generated power as indicated in Eq. (2.27) through the quantity $G(Z, w_0, \rho)$. Actually, the incident waves will only interact in a restricted volume. The magnitude of this effect is particularly important when the Poynting vectors of the two incident beams are not collinear, which is for example the case of type II SHG, as shown in Fig. 2.10.

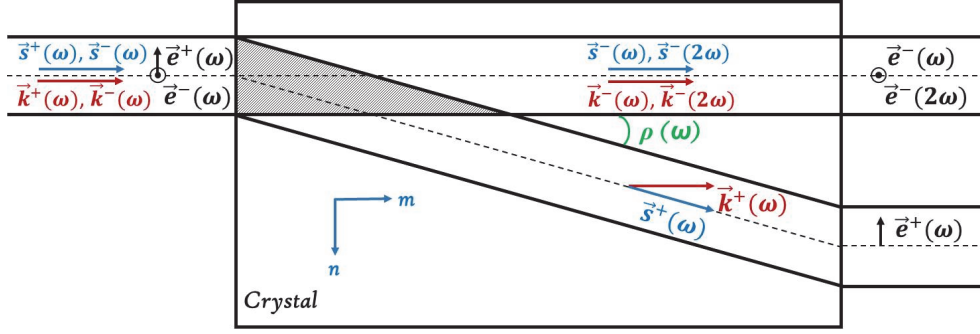


Figure 2.10 Spatial separation between the interacting beams in the case of Type II SHG in the principle planes (x, z) or (y, z) of a positive uniaxial crystal as an example.

Figure 2.10 well shows that the SHG is interrupted beyond the separation of the two fundamental beams.

The G factor can be analytically calculated only for SHG in the case of a propagation under the parallel beam approximation, that is to say when the crystal length L is lower than the twice Rayleigh length $Z_R = \pi w_0^2 / \lambda_\omega$. It is given by [4, 20]:

$$\text{Type I: } G_I(t) = \frac{\sqrt{\pi}}{t} \text{erf}(t) - \frac{1}{t^2} [1 - \exp(-t^2)] \quad (2.39)$$

$$\text{Type II: } \begin{cases} G_{II}(t) = \frac{2}{\sqrt{\pi}} \int_{-\infty}^{+\infty} F^2(a, t) da \\ \text{where} \\ F(a, t) = \frac{1}{t} \exp(-a^2) \int_0^t \exp[-(a + \tau)^2] d\tau \end{cases} \quad (2.40)$$

where $t = \rho L / w_0$, $a = m / w_0$, $\tau = \rho n / w f_0$, and m and n are the Cartesian coordinates in the plane containing the angle of double refraction as presented in Fig. 2.10.

The G factor will be strictly equal to 1 when the angle of double refraction is zero, which occurs when the propagation is along one of the principal axes of the dielectric frame, that is to say x , y or z , in a crystal belonging to the uniaxial or biaxial optical class. It is also the case when propagating the waves in any direction of the principal plane $x - y$ of a uniaxial crystal. Otherwise, the double refraction phenomenon occurs and limits the value of the conversion efficiency with $G < 1$.

2.4 Conclusion

When light propagates with a strong intensity, then the induced polarization varies non-linearly with the electric field of light. This phenomenon leads to nonlinear processes such as sum- and difference-frequency generations that will be experimentally considered in the following chapters.

Several conditions are required for achieving an optimal conversion efficiency. On the one hand, the phase-matching can be achieved, using several possible configurations: by compensating the dispersion of the refractive indices by the birefringence (BPM), or by reversing periodically the sign of the effective coefficient (QPM and AQPM). On the other hand, the magnitude of the effective coefficient has to be maximal, which can be reached by finding the right direction associated with the right configuration of polarization of the three interacting waves.

This theoretical chapter is useful for understanding and analyzing the experimental works that are described in the next chapters.

3 LGN crystal

3.1 State of the art and motivations

The optical parametric generation in the near infrared from 2 to 6 μm is of prime interest for numerous applications in civil and military fields [21-24]. The properties of the nonlinear crystals are key factors for achieving the nonlinear processes. But there is still a lack of appropriate crystals for high energy in this range. For example, the borates like LiB_3O_5 (LBO), and $\beta\text{-BaB}_2\text{O}_4$ (BBO) [25, 26] crystals have multi-photons absorption that limits the transmission range [27] ; LiNbO_3 (LN) [28] exhibits a photorefractive effect [29] ; and finally ZnGeP_2 (ZGP) can be pumped only above 2 μm , the damage threshold being reported as 60 MW/cm², which is quite low [30, 31].

“Langasite” is the generic name given to a family of crystals that are isotype of $\text{La}_3\text{Ga}_5\text{SiO}_{14}$ (LGS). These mineral materials belong to the 32 trigonal point group, where 3 and 2 stands for the 3-fold and 2-fold axes, respectively. These crystals can be grown in large size and good quality by the Czochralski method. They are widely used for bulk acoustic wave (BAW), surface acoustic wave (SAW), as well as high temperature sensor devices because of their outstanding piezoelectric properties and low acoustic friction [32-37]. Recently, the Langatate $\text{La}_3\text{Ga}_{5.5}\text{Ta}_{0.5}\text{O}_{14}$ (LGT), that is a langasite compound, was reported as a novel mid-infrared nonlinear crystal with very good indicators compared to KTP [33]. This reveals that this family may have a strong potential. This chapter describes the study of another crystal of this family, *i.e.* $\text{La}_3\text{Ga}_{5.5}\text{Nb}_{0.5}\text{O}_{14}$ (LGN): some preliminary measurements published in 2002 seemed to indicate that this crystal has also interesting nonlinear properties [32], in particular for parametric generation between 3 and 5 μm according to its transparency range,

with the ability to be grown to centimeter size. The present chapter aims at describing the LGN crystal structure, our crystal growth experiments and measurements of the linear and nonlinear optical properties.

3.2 Crystallographic structure

The Langasite crystals, with the general chemical formula $A_3BC_3D_2O_{14}$, belong to trigonal system and the P_{321} space group [38]. They contain 4 cationic sites that can be occupied by different ions. The crystal structure of LGN is shown Fig. 3.1, and briefly described hereafter. The La^{3+} ions sit at the center of (LaO_8) dodecahedrons (yellow), the Ga^{3+} ions have two positions, *i.e.* (GaO_4) tetrahedrons (deep green) and trigonal-pyramids (light green), and the Nb^{5+} ions are in forms of (NbO_6) octahedrons (light purple). Meanwhile, the (LaO_8) dodecahedrons and (NbO_6) octahedrons share the O-O edge. Then the two types of (GaO_4) are situated around the octahedrons according to the 3-fold axis. The ionic radii of Ga^{3+} (6) and Nb^{5+} (6) are 0.62 and 0.68 Å, respectively, which are close and these cations possessing ns^2np^6 electron shells could produce less localized chemical bonds which are beneficial for substitutions. Then the Ga^{3+} (6) sites could be occupied by Nb^{5+} (6) forming (NbO_6) octahedrons [39, 40]. Note that the Nb^{5+} ions are located only in the octahedral sites that result in the deviation of the rotation of opposite faces of octahedrons, these faces being normal to the *c-axis* [41]. Moreover, the octahedrons are distorted, which induces a high nonlinear polarizability and also influences the infrared (IR) cut-off of the compound [42].

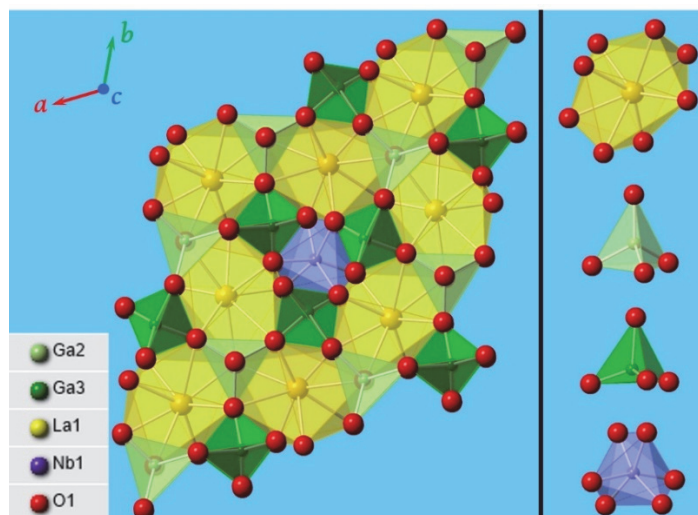


Figure 3.1 A fragment of the structure of LGN crystal (left); polyhedrons of (LaO_8) , (GaO_4) and (NbO_6) (right). a , b and c correspond to the crystallographic axes.

The c axis of the crystallographic frame is along the ternary axis. It is perpendicular to the axes a and b that make an angle of 120° between each other, the a -axis being oriented along a 2-fold axis.

3.3 Crystal growth

3.3.1 Introduction

The crystals of Langanite family are all congruent compounds, which means that they keep the same chemical composition up to the melting temperature, ranging between 1300 and 1500°C . Furthermore, these crystals do not exhibit any phase transition up to these temperatures. Therefore, the Czochralski method can be used for the crystal growth process: it consists in growing the crystal from a seed immersed in a high temperature liquid solution having the same chemical composition than the crystal. Among all the crystal growth techniques, like the flux method, the floating zone method, and vapor phase epitaxy for

example [43], the Czochralski method is nowadays one the most popular for fabricating single crystals in the field of microelectronics and photonics. Actually it has several advantages given below:

- (1) the growth condition can be observed during the whole growth process which means an easy adjustment of the parameters;
- (2) there is no direct contact between the crystal and the crucible, hence the stress could be reduced;
- (3) the necking technique could be utilized for suppressing the defects;
- (4) it is easy to obtain single crystals with large sizes and high optical quality.

In 1916, Czochralski first used this method for fabricating the metal single crystals such as Sn, Zn, Pb for example [44]. In 1918, Warenberg invented the seed technique, where a Zn crystal was obtained from a Zn wire [45]. In 1948, Teal and Litter grew Ge and Si crystals by using the seed technique combined with the rotation and shape control of the crystal [46]. In 1958, Dash discovered the necking technique aiming at reducing the dislocations in the crystal [47]. This technique has been widely used from this last step. Since the progress of the induction heating combined with the use of iridium crucible, more and more crystals have been grown, especially many with a high melting point. Thanks to further technological developments, the Automatically Control System (ADC) of the crystal diameter has been installed into the furnace. Meanwhile, several kinds of softwares, for example CGSim (STR Group), have been developed for simulating the growth process, which helps to improve the crystal growth parameters, *i.e.* temperatures, rotating rates and pulling rates, etc..

For growing a crystal using the Czochralski method, the raw materials have to be put into a crucible and heated until melting. The seed is then immersed into the melt, also called the “fusant”, and the temperature is adjusted

until a slight melting of the surface of the seed. Soon afterwards, the seed is pulled up slowly with a control of the temperature that leads to the crystallization of the melt onto the seed. For obtaining the required diameter, the heating power must be adjusted. Figure 3.2 shows some pictures of the Czochralski growth process used for the emblematic example of silicon crystal growth.

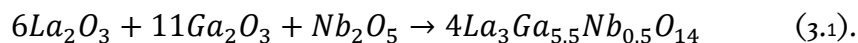


Figure 3.2 Schematic diagram of the silicon crystal growth process using Czochralski method [48].

The Czochralski method usually includes the following procedures: dosing, sintering, melting, necking, shouldering, equal-diameter growth and cooling [49].

3.3.2 Chemical composition of the melt for the growth of LGN

The raw materials were prepared from a mixture of La_2O_3 , Ga_2O_3 , and Nb_2O_5 powders with a purity of 99.99% in stoichiometric ratio according to the following chemical equation:



The mixture was put into the sintering furnace and kept for 10 hours at the temperature of 1100°C . Then it was grinded and mixed again and ready for briquetting. Afterwards, the blocks were kept for 10 hours at the temperature of 1100°C again, so that the polycrystal raw materials are ready for starting the growth. There are two points that require paying attention to: La_2O_3 absorbs moisture and CO_2 so that it has to be sintered prior to the global sintering process; and Ga_2O_3 can be easily volatilized during the process of sintering and crystal growth, which requires putting more Ga_2O_3 at the beginning, typically 1-2 weight% more.

3.3.3 Description of the furnace used for our experiments

For the crystal growth, we used the TDJ-L50 furnace conceived at Xi'an University of Technology, as shown in Fig. 3.3.

This furnace is equipped with a medium frequency power supply, whose power is 25 kW and frequency is 0.2~20 kHz. Using this furnace, we can grow crystals with a melting point up to 2100°C . Meanwhile, the temperature controlling is realized by a temperature controller/programmer (EUROTHERM818) with an accuracy of $\pm 0.2^\circ\text{C}$. The pulling rate of this furnace is 0.1~10 mm/h with a precision better than $1 \mu\text{m}$, and the rotating rate can be tuned between 0 and 40 rpm (revolutions per minute). Moreover, we

improved this furnace by adding an automatic growth control system which could enable the ADC crystal growth.



Figure 3.3 TDJ-L50 Czochralski crystal growth furnace.

3.3.4 Weight control

This process was achieved by the automatic top-weighing method allowing the weight of the crystal to be collected and processed by a computer: from a comparison between the collected signal and the set value, *i.e.* crystal weight or diameter, the computer realizes the real-time controlling and adjusting using the Proportion Integral Derivative (PID) function for the ADC process. The controlling software that we used was the JPG Auto Diameter Control Program XT-02 V 4.1, with a sensor in the weighting system having a measuring range up to 10 kg and a precision of ± 0.01 g. The goal of the ADC technique is that the crystal growth follows exactly the set value, which required the suited P, I and D parameters. The PID function is described below:

$$Y = P \cdot E + I \cdot \int E dt + D \cdot dE/dt \quad (3.2)$$

where Y is the output power; E is the error between feedback signal, such as the diameter, and the set signal; the parameters P , I and D stand for proportion, integral and derivative respectively. P is mainly responsible for the temperature control. When an error E exists between the actual and set values, the heating power will be proportionally adjusted according to P for eliminating the error. As presented in Eq. (3.2), the output power will reach 0 when $E = 0$. Therefore, the error E cannot be eliminated only by adjusting P . Then the integral parameter I is led in for thoroughly achieving the balance between the actual and set values. The main purpose of the derivative parameter D is to improve the reactive sensitivity of the system. Under the common regulation of P , I and D , the actual values can follow the change of set values thanks to a proper choice of the initial set values of P , I and D .

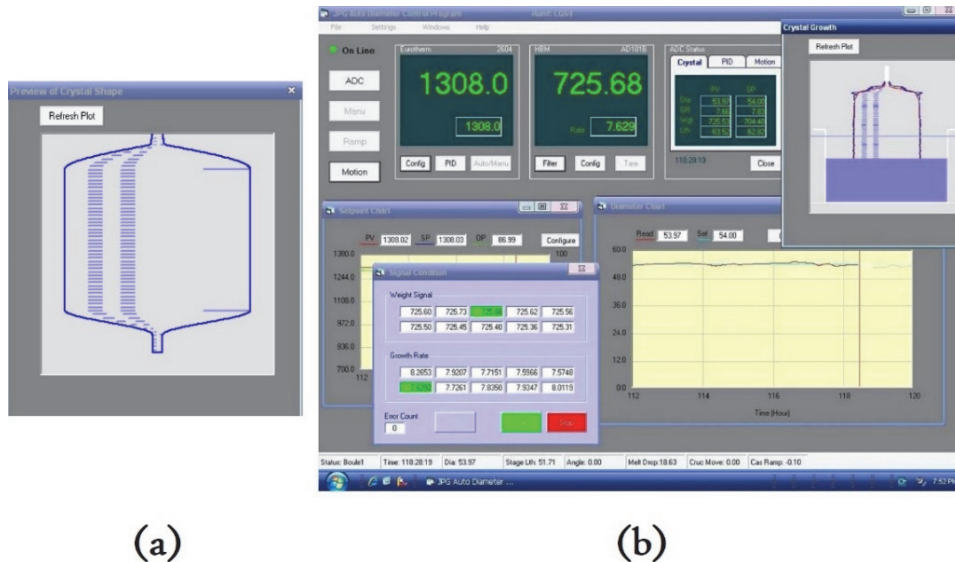


Figure 3.4 (a) The as-designed crystal shape; (b) the control program interface.

The designed crystal shape and the control program interface are shown in Fig. 3.4 (a) and (b), respectively.

Once the suited values of P, I and D are defined, the growth process can begin from the heating and melting of the polycrystal raw materials, followed by the introduction of the seed into the melt. When the crystal has reached the expected size, the temperature is then increased by 20~30°C up to the melting temperature and the as-grown crystal is simultaneously pulled out of the melt. The increasing of temperature allows the crystal to be extract of the melt quickly without redundant crystallization in the bottom. Then the melt is cooled down at a rate of 20~50 °C /h to the room temperature.

In order to grow high-optical quality crystals, several other essential factors have to be taken into account as described below.

3.3.5 Thermal field

A proper thermal field, which is the spatial distribution of the temperature, requires to be established for achieving a high-quality crystal. The thermal field is described by the axial and radial temperature gradient vectors that affect the shape of the crystal inside the melt. This shape is given by the shape of the isothermal surface at the melting point corresponding to the solid/liquid interface. There are three possible topologies: convex to the fusant (Fig. 3.5 (a)), plane (Fig. 3.5 (b)), and concave (Fig. 3.5 (c)). Among these three topologies, the plane shape is the best one while the concave is the worst one because it is detrimental to the thermal stability of the interface. But the plane shape is hard to achieve in practice, so that a slight convex shape is usually considered.

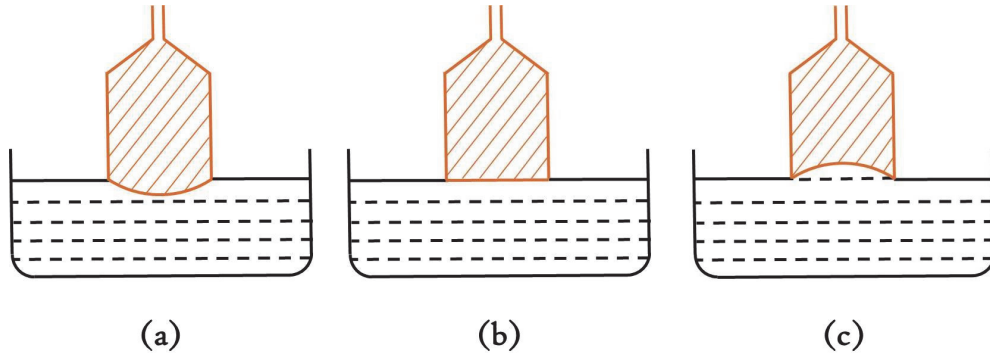


Figure 3.5 The schematic of the three possible topologies for the solid/liquid interfaces in shapes of convex (a), plane (b) and concave (c).

The crystal growth velocity V , also called the crystal growth rate, can be described by the following equation:

$$V = (k_s G_s - k_L G_L) / \rho_s L \quad (3.3)$$

k_s and k_L are the heat conduction coefficient of the crystal and fusant respectively; G_s and G_L are the temperature gradient in the crystal and the fusant respectively; ρ_s is the density of the crystal and L is the solidification heat of the crystal. The lower the temperature gradient of the fusant G_L , the faster the crystal growth rate V is, according to the invariability of the temperature gradient of the crystal G_s . Then we could get the largest crystal growth rate V_{max} , which is given by the following equation when $G_L=0$:

$$V_{max} = k_s G_s / \rho_s L \quad (3.4).$$

Hence, the crystal growth rate is higher when the radial temperature gradient becomes smaller.

The thermal field is mainly influenced by the crucible, the heating system, the applied atmosphere, and the thermal insulation material. The thickness and types of the latter are the easiest to adjust. We selected a thick mullite brick after a lot of attempts. Figure 3.6 shows the simulated results using the software CGSim for three different kinds of the thermal insulation materials: thin mullite brick, thick mullite brick and thick cellucotton. As shown in Fig. 3.6 (a) and (b), the temperature in the furnace when utilizing thin insulation material is much higher than that using a thick insulation material. Therefore, the heat loss is bigger in the thin insulation material, which needs a lot of input power to be compensated. On the other hand, the heat loss caused by this thin material induces poor heat stability, which is harmful to the stability of the crystal growth environment. When we compare the thick mullite brick (b) and cellucotton (c), we see that the heat insulation effect is much better. But the forced convection is much stronger than the free convection (b-2 and c-2), which leads to a concave shape solid-liquid interface in the condition of cellucotton. For all these reasons, we selected the thick mullite brick.

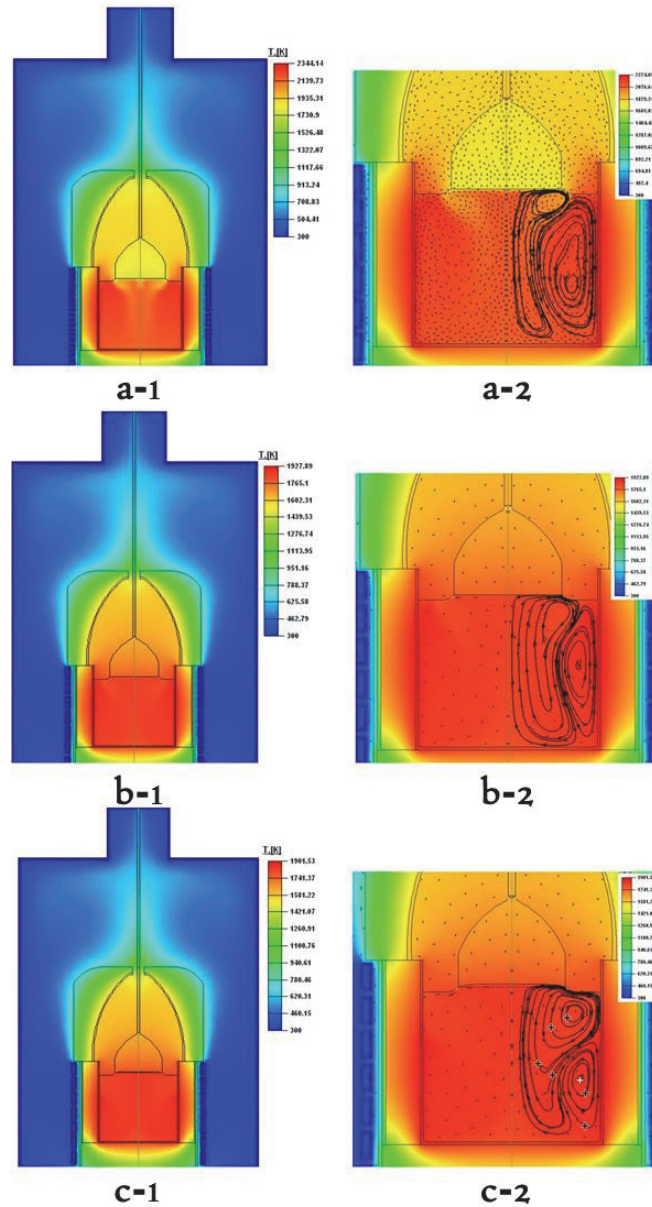


Figure 3.6 Simulated thermal field in the cases of thin mullite brick (a), thick mullite brick (b) and thick cellucotton (c). Pictures 1 correspond to the thermal distribution in the furnace, while pictures 2 concern the fusant [50].

Besides the thickness and types of the thermal insulation materials, the axial symmetry of the thermal field is also very important. This axial symmetry can guarantee the cylinder shape of the crystal. Actually, it has to be optimized in order to prevent from the radial growth rate up to the required crystal diameter and also the spiral growth [51, 52]. Two conditions should be fulfilled

for achieving this goal: firstly, it is necessary to have an observation hole in the mullite brick allowing to surveille the growth process, but it should be as little as possible in order to get no thermal perturbation; secondly, the seed holder, seed, crucible and thermal insulation material should have the same symmetry axis, which is also the symmetry axis of the thermal field.

3.3.6 Growing atmosphere

A N_2 atmosphere should be filled in the furnace for preventing the oxidization of the iridium crucible. But the gallium oxide Ga_2O_3 in the fusant is much easier to volatilize in an oxygen-deficient environment. Then we chose an atmosphere of N_2 with the oxygen content of 2%~3% vol., which looked like a good compromise. Note that our previous study on the growth of LGS [53] had shown that the color of the crystal depends on the oxygen content in the furnace: the color got deeper when there was more oxygen, as shown in Fig. 3.7 .



Figure 3.7 Different LGS crystals grown in an atmosphere with different oxygen content: 3% vol. (left), 1% vol. (right) [54].

3.3.7 Rotating and pulling rates

The constitutional supercooling theory is useful for analyzing how the pulling and rotating rates affect the crystal quality. The constitutional supercooling condition is defined as following, which is the criterion for getting the best crystal quality:

$$\frac{G}{v} < \frac{mC_L(k_0 - 1)}{D[k_0 + (1 - k_0)\exp(-\frac{v}{D}\delta)]} \quad (3.5)$$

$$\delta = 1.61D^{1/3}v^{1/6}\omega^{-1/2} \quad (3.6)$$

δ is the thickness of the solute boundary layer, D is the diffusion coefficient for solute in the fusant, v is the pulling rate, ω is the rotating rate, G is the radial thermal gradient at the interface, m is liquidus rate, C_L is the average concentration of the medium in the fusant, and k_0 is the equilibrium segregation coefficient of the solute. From Eq. (3.5), it can be seen that when the rotating rate gets higher, then the thickness of the solute boundary layer becomes thinner, so that it is harder to achieve the constitutional supercooling. Moreover, a higher rotating rate is beneficial to the change process from the convex interface to the ideal plane interface. However, it will also affect the interface stability. Fig. 3.8 (a), (b), (c), (d) are the simulated thermal field of LGN crystal growth using different rotating rates of 0, 9, 13 and 17 rpm, respectively.

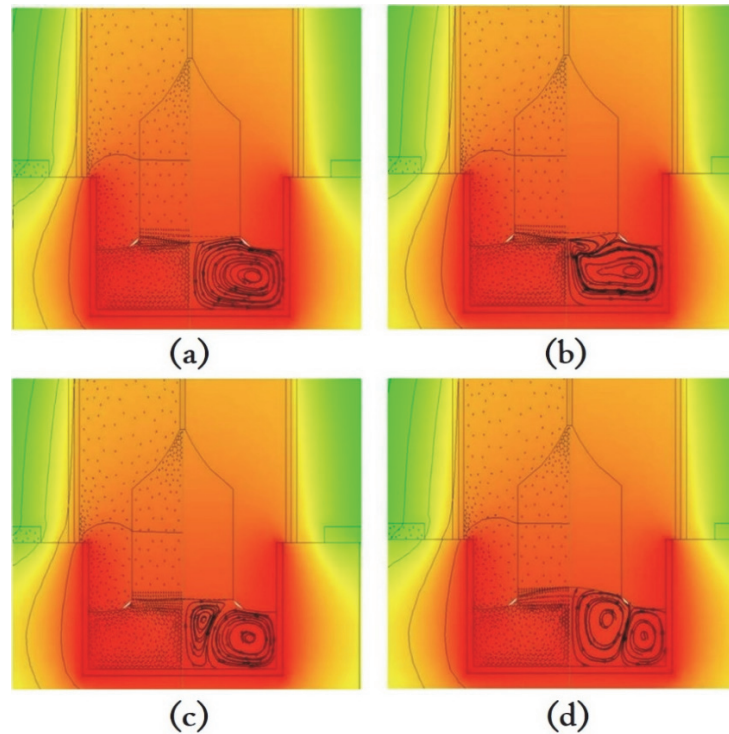


Figure 3.8 Simulated thermal field in the cases of different rotating rates of ω (a), 9 (b), 13 (c) and 17 (d) rpm [50].

Figure 3.8(a) indicates that when there is no rotation, then there is no forced convection, so that the free convection rises along the wall and flows to the bottom of the crucible with passing the surface. A forced convection appears when the rotation is activated, and it increases with the rotation speed. When the rotating rate is equal to 13 rpm (see Fig. 3.8 (c)), the solid-liquid interface becomes plane, which is a good configuration. The solid-liquid interface becomes concave when the rotating rate reaches 17 rpm, as shown in Fig. 3.8(d). Then we used a rotating rate ranging between 9 and 13 rpm.

The pulling rate has also an influence on the crystal quality through the crystal growth rate. Actually, an increasing of this rate is beneficial for making the effective segregation coefficient close to 1, which ensures a uniform chemical composition of the crystal. The segregation coefficient is given by the

ratio of the concentrations in the crystal (C_L) and in the liquid phase (C_s), and it is expressed as following [55]:

$$k_{\text{eff}} = \frac{C_s}{C_L} = \frac{k_0}{k_0 + (1 - k_0) \exp\left(-\frac{V}{D} \delta\right)} \quad (3.7)$$

k_0 is the equilibrium segregation coefficient of the solute determined by the characteristics of the solute and the solution, δ is the thickness of the solute boundary layer, D is the diffusion coefficient for solute in the fusant, and V is the crystal growth rate. As shown by Eq. (3.7), the effective segregation coefficient becomes close to 1 when V increases. It is the target, but the pulling rate should not be too fast because it would be unfavorable for removing the impurities. The best compromise is to work with a pulling rate ranging between 0.3-2 mm/h.

3.3.8 Summary of the crystal growth technical parameters and produced crystals

All the technical parameters for growing LGN crystals defined in the previous sections are summarized in Table 3.1.

Table 3.1 Crystal growth technical parameters used for the growth of LGN

Crucible	iridium, diameter-100 mm, height-56 mm
Atmosphere	N_2+O_2 (2~3% vol)
Pulling rate	0.3~2 mm/h
Rotating rate	9~13 rpm
Cooling rate	20~50 °C /h

An as-grown LGN crystal weighting 410 g, with 45 mm in diameter and 100 mm in length, is shown in Fig. 3.9 (left); another LGN crystal weighting 215 g, with 27 mm in diameter and 70 mm in length is depicted in Fig. 3.9 (right).

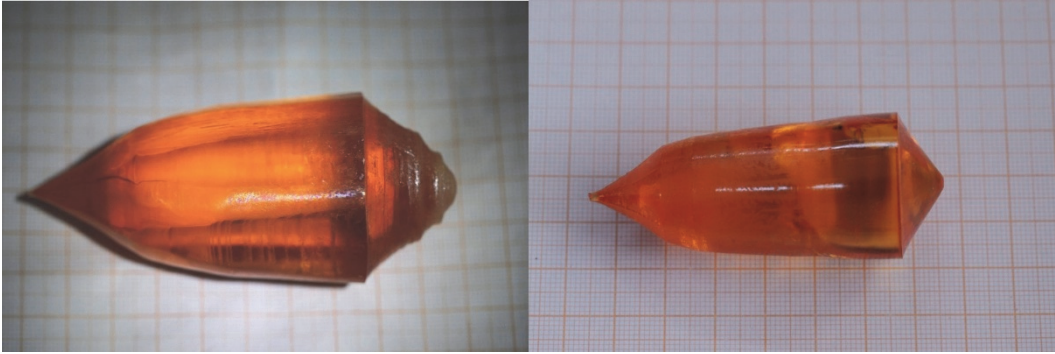


Figure 3.9 As-grown LGN crystals along the c -axis by the Czochralski method.

3.4 Linear optical properties

This part is based on the theoretical elements discussed in § 2.2 of Chapter 2.

3.4.1 Orientation of the dielectric frame

The dielectric frame (x, y, z) is the frame in which the tensor of the real part of the dielectric constant is diagonal. It is then the frame in which any optical property has to be expressed. It is an orthonormal frame, so that it cannot correspond to the crystallographic frame of LGN defined in § 3.2. We used the standard convention for the relative orientation between these two frames [6]: z is parallel to c , x is parallel to a , while y is located at 30° from b , as shown in Fig. 3.10.

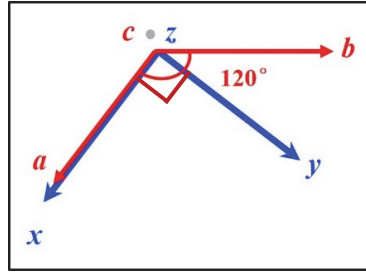


Figure 3.10 Orientation between the crystallographic (red) and the dielectric (blue) frames of LGN.

3.4.2 Transmittance spectra

The transmittance spectra were recorded using a 2-mm-thick and x -cut slab with aperture dimensions of $4 \times 4 \text{ mm}^2$. It was uncoated but polished to optical quality. We used an ultraviolet-visible-NIR spectrometer (JASCO, Model V-570) emitting polarized light between 0.19 and $2.5 \mu\text{m}$, and a FT-IR spectrometer (NEXUS 670, Thermo Nicolet Co.) emitting unpolarized light between 2.5 and $8 \mu\text{m}$.

Polarized and unpolarized transmittance spectra are depicted in Fig. 3.11(a) and 3.10(b) respectively, the inset of Fig. 3.11(a) corresponding to a zoom of the ultraviolet edge. LGN is globally transparent between 0.22 and $7.4 \mu\text{m}$, despite a strong and narrow polarized absorption peak located at $1.85 \mu\text{m}$, which is probably due to oxygen defects. There is also a smaller absorption peak at $3 \mu\text{m}$ because of Ga-O bonds [56]. From the transmission point of view, Figs. 3.11 show that LGN is suited for optical parametric generation (OPG) in band II ($3 \sim 5 \mu\text{m}$) of transmission of the atmosphere when pumped with femtosecond Ti:Sapphire or nanosecond Nd:YAG lasers, and that without any two photon absorption (TPA) of the pump.

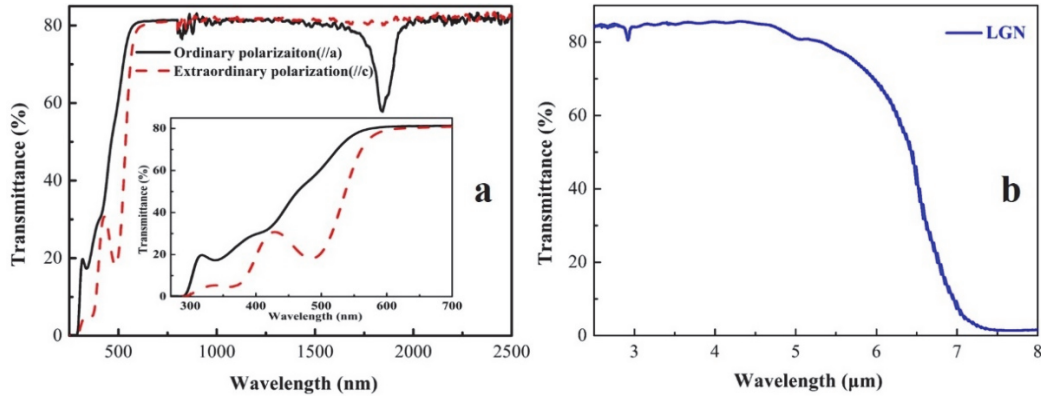


Figure 3.11 Polarized (a) and unpolarized (b) transmittance spectra of a 2-mm-thick slab of LGN cut along the x -axis. The insert in (a) corresponds to a zoom of the ultraviolet edge.

3.4.3 Optical damage threshold

The optical damage was studied using a Q-switched Nd:YAG laser (ICT Laser Work Station, Piano 2000) with a 5-ns pulse width and a 10-Hz repetition rate. The laser beam was focused using a 100-mm-focal BK7 lens onto a polished 2-mm-thick LGN slab with aperture dimensions of 4×4 mm². We also illuminated a KTP slab for reference in the same conditions. The two samples were moved toward the beam waist plane, by using a precision translation stage (Zolix Inc.), until the occurrence of a damage at the input surface of the crystals.

The beam waist diameter was equal to $30 \mu\text{m}$ at input surface of the two crystals. In these conditions, LGN was damaged at an incoming energy of $500 \mu\text{J}$, *i.e.* a peak power density of $2.82 \text{ GW}/\text{cm}^2$. It is a little bit lower than that of KTP where the damage was observed at $760 \mu\text{J}$, *i.e.* $4.29 \text{ GW}/\text{cm}^2$.

3.4.4 Sellmeier equations using the prism method

For the measurement of the principle refractive indices, a high optical quality LGN crystal was cut as a few centimeters prism with a vertex angle of $25.05 \pm 0.112^\circ$ as shown in Fig. 3.12.

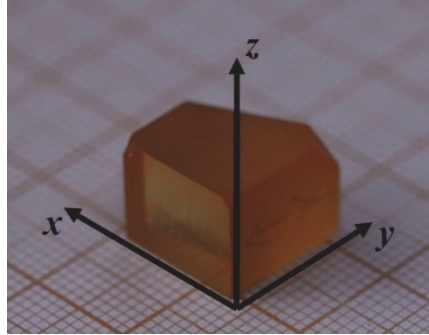


Figure 3.12 LGN prism used for the measurement of the refractive indices

The edge was cut along the z -axis so that the light propagates in the (x, y) plane of a uniaxial crystal. It has the advantage of a birefringence, *i.e.* $\Delta n = n_e - n_o$, independent of the direction of propagation, and without any spatial walk-off.

The LGN prism was placed in a high precision automatic spectrometer-goniometer (HR Spectro Master UV-VIS-IR from Trioptics). This commercial device provides measurements of the minimum deviation in polarized light for eleven sets of discrete wavelengths ranging between 0.43 and 2.33 μm known with a precision of 10^{-5} . By adjusting the proper orientation of the linear polarization of the input beam, it has been possible to determine the values of the ordinary and extraordinary principal refractive indices of LGN, *i.e.* n_o and n_e respectively, with an accuracy of 10^{-5} .

The corresponding data are displayed in Table 3.2 for the eleven sets of discrete wavelengths.

Table 3.2 Ordinary (n_o) and extraordinary (n_e) principal refractive indices of LGN, and corresponding maximal value of birefringence Δn , as a function of wavelength.

λ (nm)	n_e	n_o	$\Delta n = (n_e - n_o)$
435.8350	2.02817	1.99267	0.0355
479.9920	2.01203	1.97811	0.03392
546.0750	1.99536	1.96286	0.0325
587.5620	1.98823	1.95639	0.03184
643.8470	1.98064	1.94940	0.03124
706.5190	1.97414	1.94349	0.03065
768.1943	1.96944	1.93908	0.03036
852.1100	1.96436	1.93440	0.02996
1013.9800	1.95866	1.92877	0.02989
1529.5800	1.94816	1.91926	0.0289
2325.4199	1.93697	1.90883	0.02814

These measurements show that LGN is a positive uniaxial crystal, *i.e.* $n_o < n_e$ as defined in § 2.2, with a strong birefringence $\Delta n = (n_e - n_o) \sim 0.03$, which is *a priori* favorable for achieving phase-matching.

By using a Levenberg-Marquardt algorithm, we fitted simultaneously the refractive indices values of Table 3.2 with the same form of Sellmeier equation than that given in [32] where λ is expressed in μm , which gives:

$$n_e^2(\lambda) = 3.79511 + \frac{0.0500}{\lambda^2 - 0.03405} - 0.00964\lambda^2 \quad (3.8)$$

$$n_o^2(\lambda) = 3.68270 + \frac{0.0464}{\lambda^2 - 0.02980} - 0.00870\lambda^2 \quad (3.9)$$

and the corresponding curves is shown in Fig. 3.13.

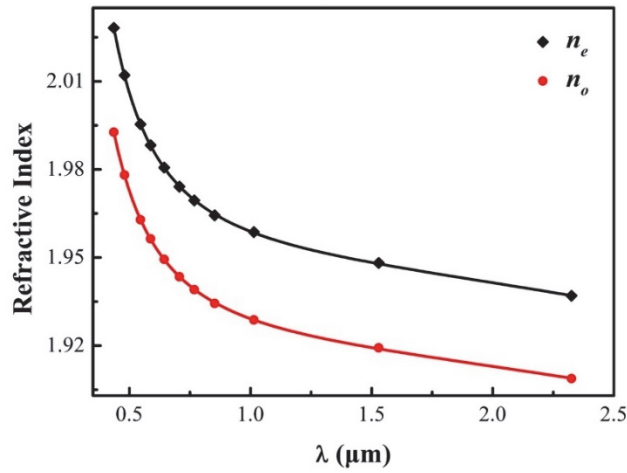


Figure 3.13 Measured principal refractive indices n_o and n_e plotted as a function of wavelength (dots), and fit of these experimental data (solid lines).

3.5 Nonlinear optical properties

The theoretical background of this part is detailed in § 2.3 of Chapter 2.

3.5.1 Calculations of the birefringence phase-matching conditions and of the corresponding effective coefficients

The birefringence phase-matching conditions have to be fulfilled in order to maximize the conversion efficiencies of Types I and II SHG, Types I, II and III SFG and DFG. The phase-matching equations and corresponding interaction types are shown in Table 2.1 of § 2.3.1. These conditions imply that the incident beams propagate along the phase-matching direction θ_{PM} in the (x, z) or (y, z) planes of LGN crystal, indicating that in a uniaxial crystal, the phase-matching equations only depend on the phase-matching angle θ_{PM} .

Table 3.3 Phase-matching conditions of a positive uniaxial crystal like LGN. λ_ω is the fundamental wavelength of SHG, and λ_1, λ_2 and λ_3 correspond to the three wavelengths involved in SFG & DFG (ω_i), with the relation of order $\lambda_1 \geq \lambda_2 > \lambda_3$.

Interaction	Birefringence Phase-Matching Condition
Type I SHG	$n_e(\lambda_\omega, \theta_{PM}) = n_o(\lambda_\omega/2)$
Type I SFG	$\frac{n_e(\lambda_1, \theta_{PM})}{\lambda_1} + \frac{n_e(\lambda_2, \theta_{PM})}{\lambda_2} = \frac{n_o(\lambda_3)}{\lambda_3}$
Type II DFG	
Type II/III SHG	$n_o(\lambda_\omega) + n_e(\lambda_\omega, \theta_{PM}) = 2n_o(\lambda_\omega/2)$
Type II SFG	$\frac{n_o(\lambda_1)}{\lambda_1} + \frac{n_e(\lambda_2, \theta_{PM})}{\lambda_2} = \frac{n_o(\lambda_3)}{\lambda_3}$
Type III DFG	
Type III SFG	$\frac{n_e(\lambda_1, \theta_{PM})}{\lambda_1} + \frac{n_o(\lambda_2)}{\lambda_2} = \frac{n_o(\lambda_3)}{\lambda_3}$
Type I DFG	

As presented in Fig. 2.3 of § 2.2, the internal layer of the index surface of a positive uniaxial crystal corresponds to the ordinary refractive index $n_o(\lambda)$, while the outer layer corresponds to the extraordinary refractive index $n_e(\lambda, \theta_{PM})$. These two indices are written as following for all phase-matching directions of the (x, z) or (y, z) plane identified by the angle θ_{PM} :

$$\begin{cases} n_o(\lambda) = n_o(\lambda) \\ n_e(\lambda, \theta_{PM}) = \left(\frac{\cos^2(\theta_{PM})}{n_o^2(\lambda)} + \frac{\sin^2(\theta_{PM})}{n_e^2(\lambda)} \right)^{-1/2} \end{cases} \quad (3.10)$$

where $n_o(\lambda)$ and $n_e(\lambda)$ are the two principal refractive indices.

According to the Neumann principle and the Kleinman assumption, the nonlinear coefficients of LGN verify: $d_{xxx} = -d_{yyy} = -d_{yyx} = -d_{yxy}$ [4]. The second-order electrical susceptibility tensor $d^{(2)} = \chi^{(2)}/2$ should be then written :

$$d^{(2)} = \begin{pmatrix} d_{xxx} & -d_{xxx} & 0 & 0 & 0 & 0 & 0 & 0 & 0 \\ 0 & 0 & 0 & 0 & 0 & 0 & 0 & -d_{xxx} & -d_{xxx} \\ 0 & 0 & 0 & 0 & 0 & 0 & 0 & 0 & 0 \end{pmatrix} \quad (3.11).$$

As written in the head part of the § 2.3, the effective coefficient of LGN writes:

$$d_{eff}(\theta_{PM}, \varphi) = d_{xxx}(F_{xxx}(\theta_{PM}, \varphi) - F_{xyy}(\theta_{PM}, \varphi) - F_{yyx}(\theta_{PM}, \varphi)) \quad (3.12)$$

The factors F_{ijk} are calculated from Eqs. (2.14) and (2.15). There is only one independent coefficient of LGN, *i.e.* d_{xxx} , written as d_{11} in the conventional contracted notation. Since the effective coefficient d_{eff} depends on the unit electric field vectors of the three interacting waves, and thus on the associated refractive indices, then the amplitude of d_{eff} depends on the phase-matching types. All the corresponding expressions of the effective coefficients regarding Types I, II and III SHG & SFG & DFG for any phase-matching direction (θ_{PM}, φ) of LGN are presented in the following Table 3.4.

The effective coefficient d_{eff} is proportional to $\sin(3\varphi)$ in the cases of Types I SHG & SFG and Type II DFG: so it will reach a maximal value at $\varphi = 90^\circ$, which corresponds to the (y, z) principal plane, and at $\varphi = 30^\circ$; it reaches zero at $\varphi = 0^\circ$, *i.e.* in the (x, z) principal plane, and at $\varphi = 60^\circ$. In the cases of Types II and III for SHG and SFG, and Types I and III for DFG, the corresponding d_{eff} is proportional to $\cos(3\varphi)$; then it is maximal at $\varphi = 0^\circ$ and at $\varphi = 60^\circ$, and it is equal to zero at $\varphi = 90^\circ$ and $\varphi = 30^\circ$. Then it is possible to measure the phase-matching angles of Types I SHG & SFG as well as of Types II DFG interactions in the (y, z) principal plane, while it can be done in the principle plane (x, z) in the cases of Types II and III SHG and SFG and Types I and III for DFG. It is what is described in the following section.

Table 3.4 Effective coefficient d_{eff} of LGN as a function of the phase-matching direction (θ_{PM}, φ) in the cases of Types I, II/III SHG and Types I, II and III SFG & DFG (ω_i).

Interaction	Effective Coefficient d_{eff}
Type I SHG	$-d_{xxx}(\lambda_{2\omega})\cos^2[\theta_{PM} - \rho(\lambda_{\omega}, \theta_{PM})]\sin(3\varphi)$
Type I SFG	$-d_{xxx}(\lambda_3)\cos[\theta_{PM} - \rho(\lambda_1, \theta_{PM})]\cos[\theta_{PM} - \rho(\lambda_2, \theta_{PM})]\sin(3\varphi)$
Type II DFG	$-d_{xxx}(\lambda_1)\cos[\theta_{PM} - \rho(\lambda_1, \theta_{PM})]\cos[\theta_{PM} - \rho(\lambda_2, \theta_{PM})]\sin(3\varphi)$
Type II/III SHG	$d_{xxx}(\lambda_{2\omega})\cos[\theta_{PM} - \rho(\lambda_{\omega}, \theta_{PM})]\cos(3\varphi)$
Type II SFG	$d_{xxx}(\lambda_3)\cos[\theta_{PM} - \rho(\lambda_2, \theta_{PM})]\cos(3\varphi)$
Type III DFG	$d_{xxx}(\lambda_1)\cos[\theta_{PM} - \rho(\lambda_2, \theta_{PM})]\cos(3\varphi)$
Type III SFG	$d_{xxx}(\lambda_3)\cos[\theta_{PM} - \rho(\lambda_1, \theta_{PM})]\cos(3\varphi)$
Type I DFG	$d_{xxx}(\lambda_1)\cos[\theta_{PM} - \rho(\lambda_1, \theta_{PM})]\cos(3\varphi)$

3.5.2 Measurement of the birefringence phase-matching properties and refinement of the Sellmeier equations

3.5.2.1 Description of the sphere method

3.5.2.1.1 Introduction

This part of the chapter aims at introducing the so-called “sphere method” proposed and developed by our group since 1989 [57], and that has been used to study the optical properties of LGN, as well PPRKTP. This method has the advantage of giving an access to any direction in the three dimensions of the space with a single sample. Because of the spherical shape, an incident laser

beam properly oriented and focused can cross the sphere in normal incidence along the sphere diameter. The smallest diameter that can be reasonably considered is around 2 mm [58].

By using this method, it is possible to determine any phase-matching angle with an accuracy better than $\pm 0.5^\circ$. This method has been successfully applied for the study of many nonlinear crystals, such as KTP [59], RTP [60], KTA [61], RTA [61], CTA [61], CSP [62], YCOB [63], GdCOB [64], LGT [33], BGS_e [65], and PPLN [66] for example.

3.5.2.1.2 General configuration of the experiment setup

For achieving the required tunability of the incident beam, the optical source we used is a multi-stages parametric source from Excel Technology and Light conversion, presented in Fig. 3.14.

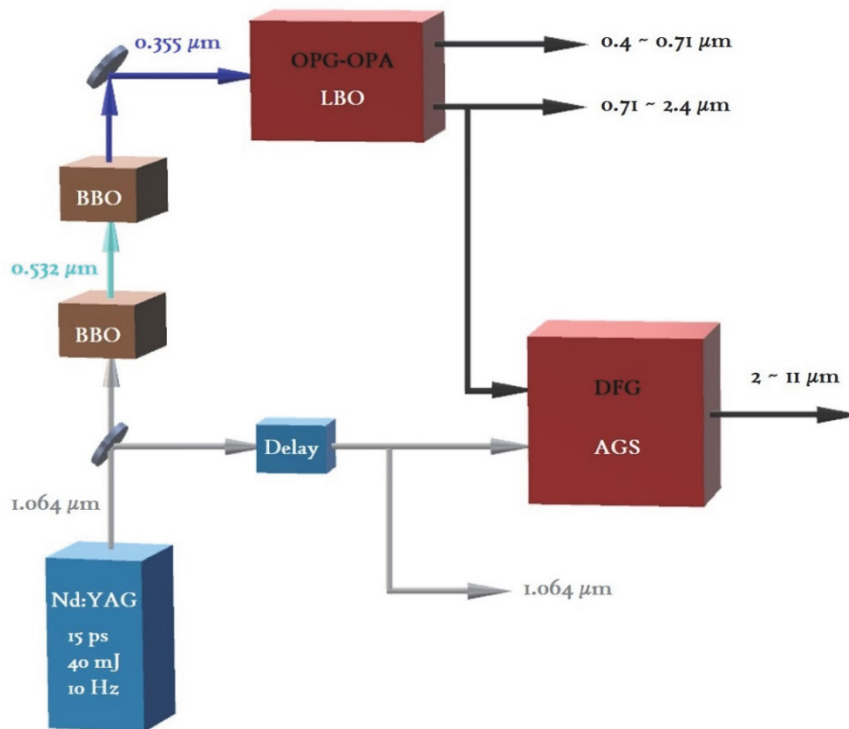


Figure 3.14 Scheme of the parametric source used for the sphere method.

A Nd:YAG laser with a pulse width of 15 ps, a repetition rate of 10 Hz and a wavelength of $1.064 \mu\text{m}$ is used as a pump source for the multi-stages parametric source. It has an average pulse energy of 40 mJ, and it is divided into two parts: 10 mJ for the DFG stage in a AgGaS_2 (AGS) crystal, while 30 mJ are used for the OPG-OPA stage based on a LBO crystal. For generating the pulses at 532 nm and 355 nm, two BBO crystals have been used for doubling and tripling the beam at $1.064 \mu\text{m}$. An energy of 8 mJ at 355 nm can be obtained. The rotation of the LBO crystal is motorized and controlled by a computer for achieving a tunability by step of 1 nm. From this stage, it is possible to get a signal wavelength λ_s tunable from $0.4 \sim 0.71 \mu\text{m}$, the corresponding idler wavelength λ_i varying between $2.4 \sim 0.71 \mu\text{m}$. The energy of these pulses changes a little bit with the wavelength and ranges around $200 \mu\text{J}$. The DFG stage is based on the mixing of this idler beam with a part of the beam at $1.064 \mu\text{m}$ inside a AGS crystal, which leads to the emission of a beam tunable from 2 to $11 \mu\text{m}$.

The experimental setup for measuring the phase-matching angles of LGN sphere is presented in Fig. 3.15.

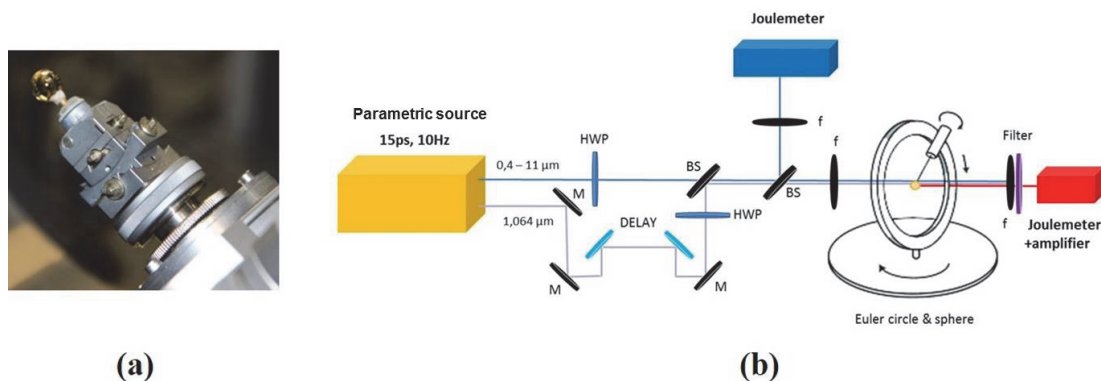


Figure 3.15 (a) Picture of the sphere of LGN stuck on a goniometric head; (b) Setup used for the direct measurement of SHG and DFG phase-matching angles.

The LGN sphere has a diameter of 10.8 mm and an asphericity below 1%. We studied Type I SHG and Type II DFG measurements in the (y, z) plane and Type III DFG in the (x, z) plane. SHG needs only one incident beam, which can be the signal or idler of the OPG-OPA or the beam generated by the DFG stage; the full tunability is then from $2 \sim 11 \mu\text{m}$. For the DFG measurements, two incident beams are required with perfect spatial and temporal overlaps: one beam arises from the OPG-OPA while the other one is a part of the $1.064 \mu\text{m}$ beam. Achromatic half wave plates (HWP) are used for adjusting the polarization of the different beams. A 100-mm-focusing lens (f) is also placed in front of the sphere in order to properly focus the incident beams inside the sphere as detailed in § 3.5.2.1.3. The energy of the incoming beams is measured by a J4-09 Molelectron pyroelectric joulemeter placed behind a beam splitter (BS) and a lens with a focal length of 50 mm. Simultaneously, a J3-05 Molelectron joulemeter combined with a PEM 531 amplifier is placed at the exit of the sphere with a filter for removing the input wavelength in order to detect only the generated beam. The phase-matching angles are measured thanks to the Euler circle, described in more details in § 3.5.2.1.4, with an accuracy of $\pm 0.5^\circ$.

3.5.2.1.3 Focusing conditions in the sphere

It is important to get a quasi-parallel propagation of the interacting beams inside the sphere for achieving a precise measurement of the angles of collinear phase-matching. Actually, a divergence inside the sphere would lead to non-collinear phase-matched interactions that would have lower efficiencies than those in the collinear phase-matched interactions [59]. Furthermore, the divergence could enlarge the spectral and angular acceptances. The distance

between the focusing lens and the sphere must be then judiciously chosen, as described hereafter.

The sphere consists of two contiguous spherical diopters and it is equivalent to a spherical lens with two identical focal lengths f described by [67]:

$$f^{\pm}(\lambda, \theta, \varphi) = \frac{n^{\pm}(\lambda, \theta, \varphi)R}{2(n^{\pm}(\lambda, \theta, \varphi) - 1)} \quad (3.13)$$

where R is the radius of the sphere and $n^{\pm}(\lambda, \theta, \varphi)$ is the refractive index in the direction of angles of spherical coordinates (θ, φ) . If $n^{\pm}(\lambda, \theta, \varphi) < 2$ then $f^{\pm}(\lambda, \theta, \varphi) > R$, which means that the two focal planes of the sphere are outside the crystal as presented in Fig. 3.16(a). On the other hand, if $n^{\pm}(\lambda, \theta, \varphi) > 2$, they are located inside the sphere since $f^{\pm}(\lambda, \theta, \varphi) < R$, which could damage the sphere as shown in Fig. 3.16(b). Several constraints should be taken into account for achieving the quasi-parallel condition [68]: the focal plane of the incident beam must be located at the focal plane of the input diopter of the sphere if $n^{\pm}(\lambda, \theta, \varphi) < 2$ as indicated in Fig. 3.16(a). On the opposite, when $n^{\pm}(\lambda, \theta, \varphi) > 2$, the so-called configuration $2f - 2f$ has to be used, as shown in Fig. 3.16(b) [68].

Not that under the quasi-parallel condition, the sphere diameter D is much smaller than twice the Rayleigh length Z_R defined by [69]:

$$Z_R = \frac{\pi n^{\pm}(\lambda, \theta, \varphi) w_{sph}^2}{\lambda} \quad (3.14)$$

where w_{sph} is the beam waist radius inside the sphere.

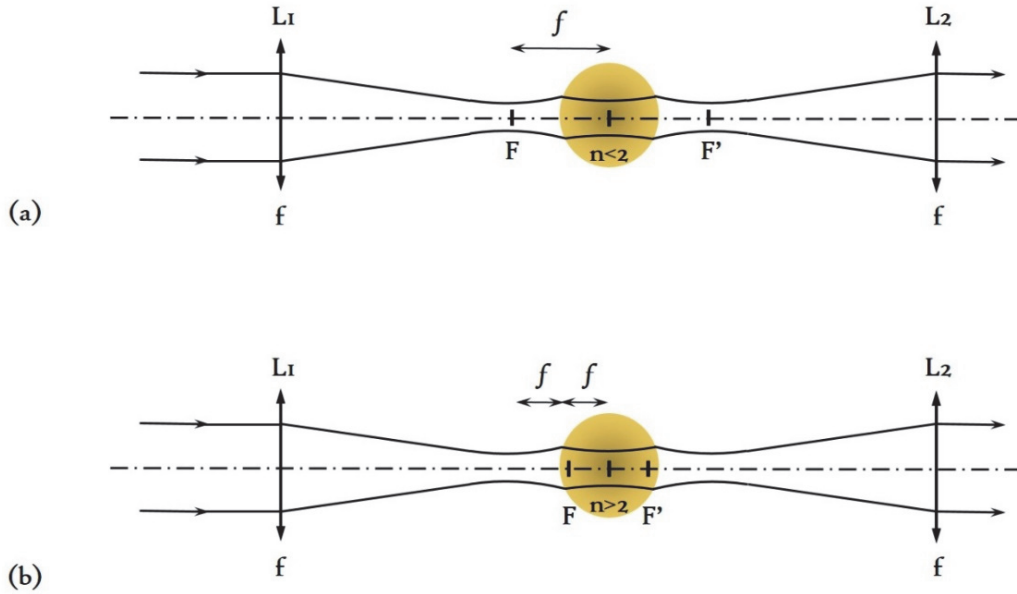


Figure 3.16 Focusing conditions of the incident beam when (a) $n^{\pm}(\lambda, \theta, \varphi) < 2$ and (b) $n^{\pm}(\lambda, \theta, \varphi) > 2$.

3.5.2.1.4 The Euler circle

The sphere is stuck on a goniometric head and it is placed at the center of the Euler circle. Each displacement of the sphere is controlled by adjusting the small translation plates located on the goniometric head. The Euler circle enables the manual control of the sphere rotation with an accuracy of 0.003° . The schematic figure of Euler circle is shown in Fig. 3.17, and the three rotations are marked by the angles α , β and γ .

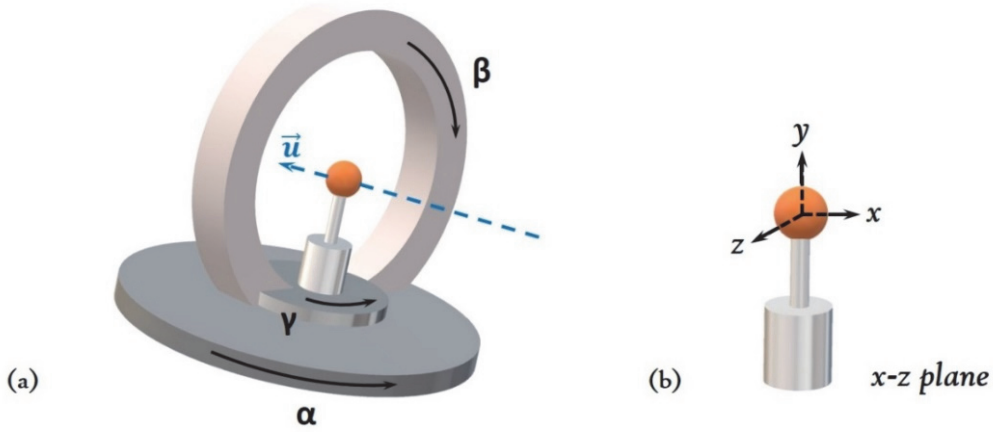


Figure 3.17 Schematic diagram (a) of the Euler circle, consisting of three rotation axes marked by the angles α , β and γ ; (b) example of a sphere oriented along the y axis.

The beams have to propagate through the center of the sphere. Under these conditions, the rotation of the sphere on it-self allows the beams to propagate in any direction (θ, φ) of the dielectric frame (x, y, z) . Note that some areas close to the sticking axis of the sphere cannot be reached because of the screening by the goniometric head or the circles of the Euler circle. Then if necessary, the sphere will have to be stuck in different directions. But we did not need that in the present study of LGN.

As presented in Fig. 3.17 (a), the angle β can be fixed for holding the vertical direction of the sphere, which is along the y axis for example as shown in Fig. 3.17(b). Then the rotation of the sphere through the angle $\alpha = \gamma$ makes it possible to explore the (x, z) principle plane. The corresponding relationship between the angles (θ, φ) in the dielectric frame and the angles α, β and γ is written as following [68]:

$$\begin{cases} \theta = \frac{\pi}{2} - (\alpha + \gamma) \\ (\varphi = 0) \end{cases}$$

(3.15).

3.5.2.2 Measured phase-matching angles of Second-Harmonic Generation and Difference-Frequency Generation

The recorded SHG phase-matching tuning curve with the sphere method is presented in Fig. 3.18 [70]. According to the analysis performed in § 3.5.1, Type I SHG ($1/\lambda_{2\omega}^o = 1/\lambda_{\omega}^e + 1/\lambda_{\omega}^e$) has been studied in the (y, z) plane. λ_{ω} and $\lambda_{2\omega}$ are the fundamental and second harmonic wavelengths, respectively. Here, the fundamental wavelength ranges from 1.3 to 3.43 μm , and no measurement is accessible beyond 75° because the associated effective coefficient is too low according to Table 3.4.

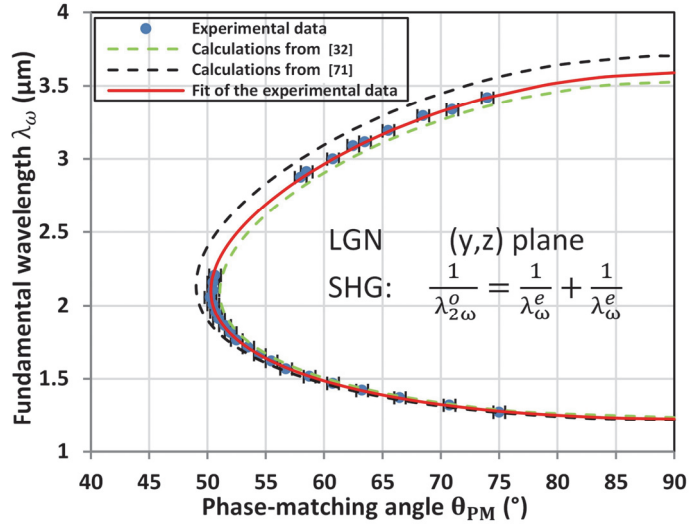
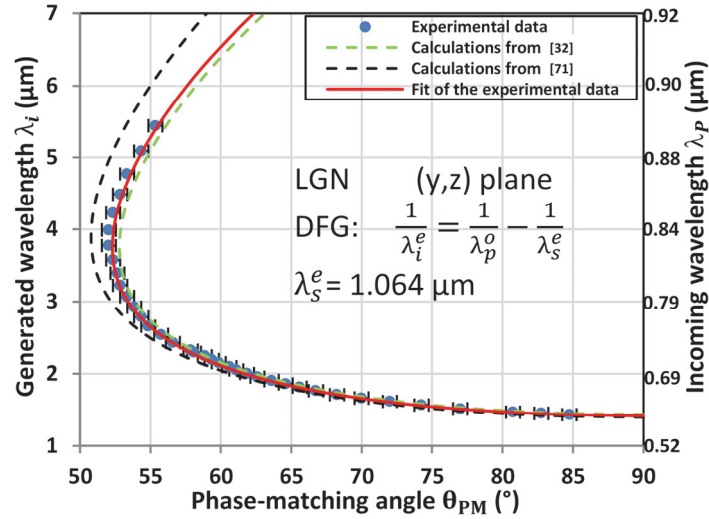


Figure 3.18 Type I SHG tuning curve in the (y, z) plane of LGN. The wavelength accuracy is within dots size.

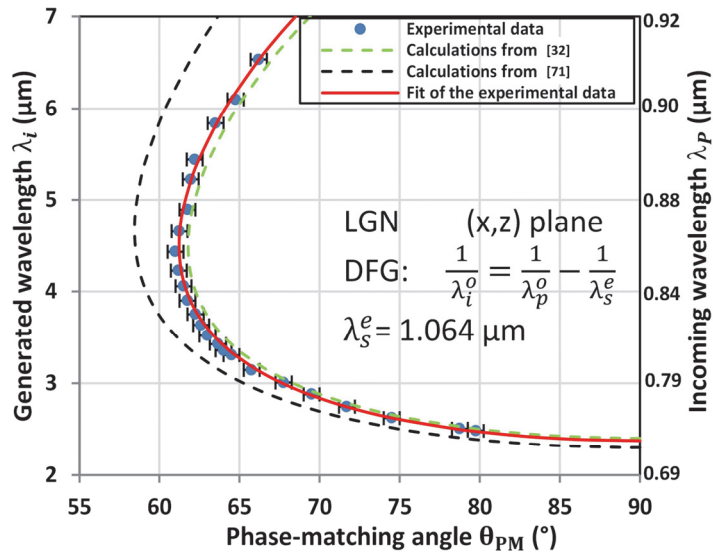
We performed the experiments of Type II DFG ($1/\lambda_i^e = 1/\lambda_p^o - 1/\lambda_s^e$) in the (y, z) plane, and type III DFG ($1/\lambda_i^o = 1/\lambda_p^o - 1/\lambda_s^e$) in the (x, z) plane. λ_p , λ_s and λ_i are respectively the pump, signal and idler wavelengths

verifying the following relation of order: $\lambda_p < \lambda_s \leq \lambda_i$, with $\lambda_p, \lambda_s, \lambda_i \rightarrow \lambda_3, \lambda_2, \lambda_1$. The DFG measurements could cover from 0.6 to 6.5 μm which is almost the entire transparency range of LGN.

The recorded DFG phase-matching tuning curves are presented in Fig. 3.19 [70].



(a)



(b)

Figure 3.19 DFG tuning curve (a) in the (y, z) and (b) in the (x, z) plane of LGN.

The wavelength accuracy is within dots size.

3.5.2.3 Refinement of the Sellmeier equations from the fit of the phase-matching angles

We refined the Sellmeier equations of LGN by the simultaneous fit of all our SHG and DFG experimental data shown in Figures 3.18 and 3.19. We used the Levenberg-Marquardt algorithm encoded with Matlab. Among the several possible forms of Sellmeier equations to fit the ordinary and extraordinary refractive indices, the best one was that previously used in Refs. [32, 71], *i.e.*:

$$n_j^2(\lambda) = A_j + \frac{B_j}{\lambda^2 - C_j} - D_j\lambda^2 \quad (3.16)$$

where λ is in μm and j stands for o or e . The precision of our angular measurements is $\pm 0.5^\circ$, which leads to a relative accuracy $\Delta n_j/n_j$ better than 10^{-4} , where j stands for o and e [60]. The numerical values of the best fit parameters A_j , B_j , C_j and D_j are summarized in Table 3.5. Our interpolated tuning curves using the Sellmeier equations of the present work correspond to the solid red lines shown Figures 3.18 and 3.19 [70]. They clearly show a much better agreement with our experimental data than using the calculations from Refs. [71] and [32].

Table 3.5. Refined Sellmeier Coefficients of the Two Principal Refractive Indices n_o and n_e of LGN

Sellmeier coefficients	A_j	B_j	C_j	D_j
$j = o$	3.6836	0.0460	0.0296	0.0094
$j = e$	3.7952	0.0483	0.0314	0.0102

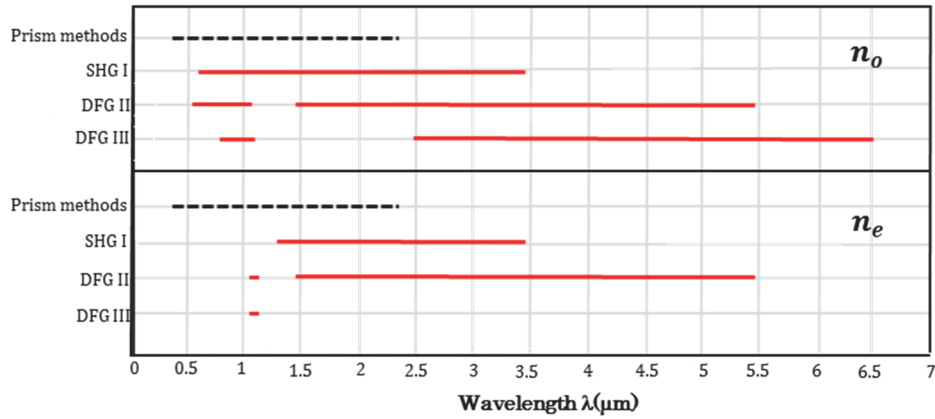


Figure 3.20 Spectral ranges where the principal refractive indices of LGN, n_o and n_e , are involved, using the sphere method (red lines), and the prism technique from [71] and [32] (black dashed lines).

Figures. 3.18 and 3.19 also show the calculated phase-matching curves using the Sellmeier equations from Refs. [71] and [32]. It highlights discrepancies between our experimental data and both sets of calculations, even if calculations using [32] are closer to our experimental data. This discrepancy is true especially above $2.3 \mu\text{m}$ that corresponds to the limit of the spectral range over which the ordinary and extraordinary principal refractive indices were determined in Refs. [71] and [32]. As shown in Fig. 3.20, by performing our measurements with the sphere method up to $6.5 \mu\text{m}$, we widely extended the wavelength range where the two principal refractive indices of LGN are involved. Such a difference might explain the discrepancies between the measurements made with the sphere method and the prism method.

3.5.3 Measurements of the nonlinear coefficient d_{11}

3.5.3.1 Non-phase-matching measurements

A Maker Fringes setup [72, 73] was implemented to determine the second-order electric susceptibility coefficient d_{11} of LGN relatively to d_{36} of potassium dihydrogen phosphate (KDP) at the same fundamental wavelength. The incoming beam was delivered by a Q-switched Nd:YAG laser (Spectra-Physics, Model Pro 230) at the fundamental wavelength $\lambda_\omega = 1.064 \mu\text{m}$ with a 10-Hz repetition rate and 10-ns pulse width. The averaged power $P(\lambda_\omega)$ was set at 20 mW and focused inside the LGN and KDP slabs. The corresponding beam waist radius was $w_0 = 0.2 \text{ mm}$ in the samples, which ensures a propagation in the parallel beam approximation since the Rayleigh length ($z_R = 11.8 \text{ cm}$) is much longer than the crystal length ($L = 1 \text{ mm}$). The slabs were cut with uncoated surface dimensions of $10 \times 12 \text{ mm}^2$ polished to optical quality, the optical parallelism being less than $0.5'$ of arc. These samples were stuck on a rotation plate with a precision of 0.00125° (RAK100, Zolix Inc.) ensuring a continuous rotation of the crystals in the (y, z) and (x, y) planes. At room temperature, the power of the SHG generated beam, $P(\lambda_{2\omega})$, was measured as a function of the sample orientation by using a photomultiplier tube (PMT, Hamamatsu, Model R105). It was averaged by a fast-gated integrator combined with a boxcar (Stanford Research Systems), and recorded using a software.

Using the Maker Fringes setup, we selected type I SHG ($1/\lambda_{2\omega}^o = 1/\lambda_\omega^e + 1/\lambda_\omega^e$) in the (y, z) plane of LGN, the corresponding effective coefficient being $d_{11}(\lambda_{2\omega})\cos^2[\theta_{PM} - \rho(\lambda_\omega, \theta_{PM})]\sin(3\varphi)$: θ is the phase-matching angle of spherical coordinate from the z -axis, φ is the spherical coordinates from the x -axis, $\lambda_\omega = 1.064 \mu\text{m}$, $\lambda_{2\omega} = 0.532 \mu\text{m}$, and ρ is the spatial walk-off. For this purpose, a 1-mm-length LGN slab was cut oriented along the three axes of the dielectric frame: the axis of rotation of the sample is the x -axis the y -axis is the direction of polarization of the incoming fundamental beam. The direction of propagation will range from either side of the z -axis in the (y, z) , as shown in

Fig. 3.21(a). We performed the measurement relatively to the nonlinear coefficient $d_{36}(\text{0.532 } \mu\text{m}) = 0.57 \pm 0.02 \text{ pm/V}$ of the uniaxial crystal KDP [74]: we implemented type I SHG ($1/\lambda_{2\omega}^e = 1/\lambda_{\omega}^o + 1/\lambda_{\omega}^o$) in the (x, y) plane of KDP where there is no spatial walk-off. The corresponding effective coefficient is $d_{36}(\lambda_{2\omega})\sin(2\varphi)$ where φ is the angle of spherical coordinate from the x -axis. We used a 1.5 mm-length $[110]$ -cut KDP slab ($\varphi = 45^\circ$) rotated around the z -axis, the incoming beam being polarized perpendicularly to this axis (see Fig. 3.21(b)).

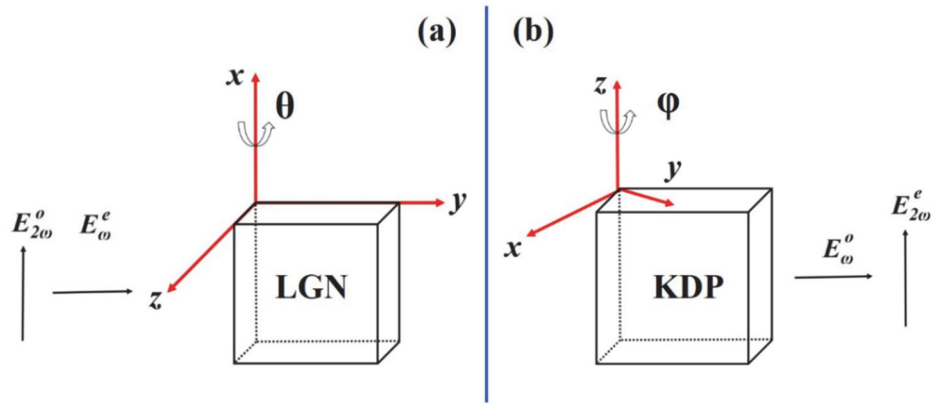


Figure 3.21 Orientation and polarization schemes of LGN (a) and KDP (b) slabs for the Maker fringes measurements. The waves propagate in the (y, z) plane of LGN and in the (x, y) plane of KDP.

The recorded fringes pattern involving d_{ii} of LGN is shown in Fig. 3.22. The figure also gives a fit of our data, using the Eqs. (2.27) and (2.28) presented in § 2.3 and Ref. [72]:

$$P(\lambda_{2\omega}, \alpha) = \beta f(\alpha) d_{ij}^2 P^2(\lambda_{\omega}) \frac{L^2}{w^2} \text{sinc}^2[\psi(\alpha)] \quad (3.17)$$

with

$$f(\alpha) = \cos(\alpha) \frac{2366 T(\lambda_{2\omega}, \alpha) T^2(\lambda_{\omega}, \alpha)}{\lambda_{\omega}^2 A(\lambda_{2\omega}, \alpha) A^2(\lambda_{\omega}, \alpha)} \quad (3.18)$$

and

$$\psi(\alpha) = \frac{2\pi L}{\lambda_\omega} [\sqrt{n^2(\lambda_{2\omega}, \alpha) - \sin^2(\alpha)} - \sqrt{n^2(\lambda_\omega, \alpha) - \sin^2(\alpha)}] \quad (3.19)$$

where α stands for θ in LGN and $(\varphi - 45^\circ)$ in KDP. L is the sample thickness, and P_ω and w are respectively the power and beam waist radius of the incoming beam. $T(\lambda_i, \alpha)$ is the sample Fresnel transmission coefficient and $n(\lambda_i, \alpha)$ is the refractive index, where the index $i = \omega$ stands for the input beam, and $i = 2\omega$ for the generated beam. The correction factor (β) has been added in Eq. (3.17) for LGN in order to take into account the absorption of the Second harmonic wave. $\beta = 1.15$ calculated from $\beta = e^{-(l_2/l_1)\ln T_1} = T_1^{-(l_2/l_1)}$ where T_1 is the transmittance of a 2 mm-length sample ($l_1 = 2$ mm) while l_2 is the length of the LGN sample used in the Maker Fringes measurement.

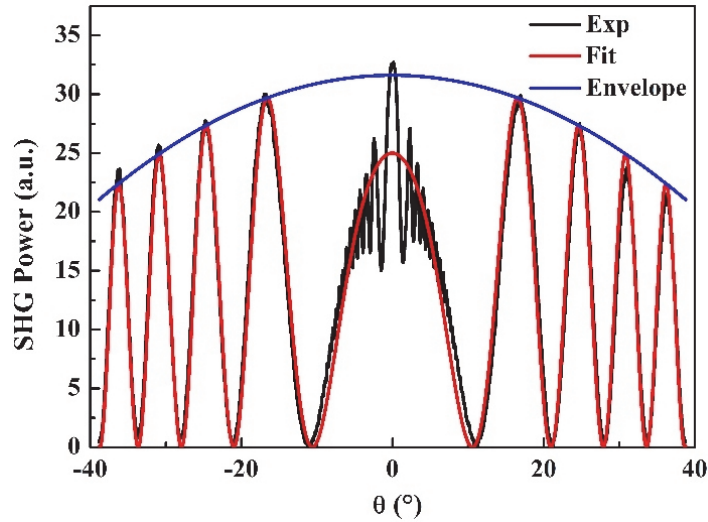


Figure 3.22 Recorded (black points), fit of experimental data (red line) and of the envelope (blue line) of the Maker Fringes pattern involving d_{11} coefficient of LGN.

By fitting the envelope of the Maker fringes pattern of Fig. 3.22 using Eq. (3.8) and (3.9), and Eqs. (3.17)-(3.19), we determined the magnitude of its

maximum value at normal incidence ($\alpha=0^\circ$), relatively to that of KDP measured in the same condition, using:

$$\frac{d_{11}^2(\lambda_{2\omega})}{d_{36}^2(\lambda_{2\omega})} = \frac{P_{LGN}(\lambda_{2\omega}, 0) L_{KDP}^2 f_{KDP}(0) \text{sinc}^2[\psi_{KDP}(0)]}{P_{KDP}(\lambda_{2\omega}, 0) L_{LGN}^2 f_{LGN}(0) \text{sinc}^2[\psi_{LGN}(0)]} \quad (3.20)$$

with

$$\psi_{LGN}(0) = \frac{2\pi L_{LGN}}{\lambda_\omega} [n_o(\lambda_{2\omega}) - n_e(\lambda_\omega)] \quad (3.21)$$

and

$$\psi_{KDP}(0) = \frac{2\pi L_{KDP}}{\lambda_\omega} [n_e(\lambda_{2\omega}) - n_o(\lambda_\omega)] \quad (3.22).$$

According to the measurement of the ratio $P_{LGN}(\lambda_{2\omega}, 0)/P_{KDP}(\lambda_{2\omega}, 0)$ and Eqs. (3.17)-(3.22), we found that the second-order nonlinear coefficient of LGN is : $d_{11}(\lambda_{2\omega} = 0.532 \mu\text{m}) = 3.0 \pm 0.1 \text{ pm/V}$.

3.5.3.2 Phase-matching measurements

In this part, the absolute value of the d_{11} nonlinear coefficient of LGN has been determined from phase-matched type I SHG in the (y, z) plane. Owing to the simplicity of the LGN tensor $d^{(2)}$ which possesses only the element $d_{11} = d_{xxx}$ (see matrix (3.9)), it is not necessary to determine the sign of this element, because it keeps squared in the generated energy expression (see Eq. (2.27)).

As shown in Eqs. (2.27) and (2.29) written for a SHG process, the effective coefficient can be measured directly from the ratio ζ between the energy $P(\lambda_{2\omega}, L)$ generated at $\lambda_{2\omega}$ and the square of the energy $P(\lambda_\omega, 0)$ incident to λ_ω :

$$\zeta = \frac{P(\lambda_{2\omega}, L)}{P^2(\lambda_{\omega}, 0)} \quad (3.23).$$

We carried out a relative measurement of the nonlinear coefficient d_{11} of LGN with respect to the reference d_{24} of the KTP crystal, regarding the type II SHG in the (x, z) plane [67]. Both crystals were studied under the same experimental conditions so that the spatial-temporal parameters of the beam are identical in the samples. Two slabs were then prepared with the same thickness $L = 0.52$ mm in order to neglect the effect of the double refraction (see § 2.3.4). The fundamental beam emitted by the OPG was focused on the crystals with a 100-mm-focal length CaF_2 lens. The corresponding beam waist diameter inside the crystals was $w_0 = 120 \mu\text{m}$, which gives a Rayleigh length of 30 mm much longer than L . Then parallel beam propagation was ensured, and non-collinear SHG is avoid. The orientations of LGN and KTP, $(\theta_{PM}^{LGN}, \varphi = 90^\circ)$ and $(\theta_{PM}^{KTP}, \varphi = 0^\circ)$ respectively, were chosen so that the corresponding fundamental wavelengths, λ_{ω}^{LGN} and λ_{ω}^{KTP} , are very close, *i.e.* $\Delta\lambda = |\lambda_{\omega}^{KTP} - \lambda_{\omega}^{LGN}| < 0.05 \mu\text{m}$. This value can be determined by comparing Type I SHG phase-tuning curve of LGN in the (y, z) plane shown in Fig. 3.18, and Type II SHG phase-tuning curve of KTP in the (x, z) plane [70].

A LGN slab was then cut at $(\theta_{PM_1} = 70.4^\circ, \varphi_{PM_1} = 90^\circ)$, which corresponds to $\lambda_{\omega}^{LGN} = 1.32 \mu\text{m}$, and a KTP slab was cut at $(\theta_{PM_2} = 58.5^\circ, \varphi_{PM_2} = 0^\circ)$ corresponding to $\lambda_{\omega}^{KTP} = 1.32 \mu\text{m}$. The difference of phase-matching wavelength is then very small, *i.e.* $\Delta\lambda = 0.003 \mu\text{m}$. The effective coefficient of LGN has been calculated in the previous part in this chapter, and that of KTP is given by:

$$d_{eff}^{KTP} = d_{24}^{KTP}(\lambda_{2\omega_2}) \sin[\theta_{PM_2} - \rho^e(\theta_{PM_2}, \lambda_{\omega_2})]$$

(3.24)

where the nonlinear coefficient of KTP is $d_{24}^{KTP}(\lambda_{2\omega_2} = 0.66 \mu\text{m}) = 2.37 \pm 0.17$ pm/V as a reference [59].

The type I SHG experiments in LGN at λ_{ω}^{LGN} and type II SHG in KTP at λ_{ω}^{KTP} were performed using the parametric source in picosecond regime described above in § 3.5.2.1.2. The half-wave plate allowed us to control the polarization of the incident beam in order to achieve type I SHG in LGN and type II SHG in KTP. A semi-reflective plate (UVFS 50/50 900-2600 nm) was used to collect half of the incident energy $P(\lambda_{\omega}, 0)$. A filter for cutting the fundamental beam was placed behind the crystals in order to measure only the energy $P(\lambda_{2\omega}, L)$ of the generated Second-Harmonic wave. The simultaneous measurement of the incident fundamental energy and of the generated Second-Harmonic energy enabled to determine the ratio ζ defined by Eq. (3.23) in each slab.

We took care of the maximization of the ratio ζ , which corresponds to phase-matching, by measuring its variation as a function of the fundamental wavelength around λ_{ω}^{LGN} for LGN and around λ_{ω}^{KTP} for KTP. This measurement also provided an estimate of the spectral acceptance, which is 19.8 mm.nm for LGN as shown in Fig. 3.23, and 19.2 mm.nm for KTP as shown in Fig. 3.24 [70]. Figure 3.23 also shows the very good agreement between the experimental points and the calculations based on our refined Sellmeier equations given in § 3.5.2.3. The small difference is due to the cutting orientation of the slab compared with the requested one. Actually the measured phase-matching wavelength, corresponding to the peak value, is equal to 1.317 μm , which is very close to the expected 1.32 μm . The same comment for KTP as shown in Fig. 3.24: the measured fundamental wavelength is 1.32 μm . The peak

magnitude of ζ for LGN and KTP allowed us to determine d_{11} of LGN relatively to d_{24} of KTP, considering that the wavelengths are the same in the two cases.

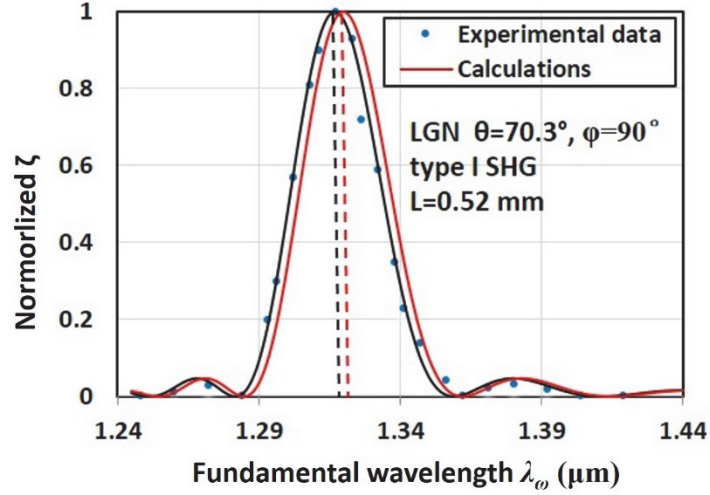


Figure 3.23 Calculated (red line) and measured (dots linked with black line) ratio ζ in LGN as a function of the fundamental wavelength.

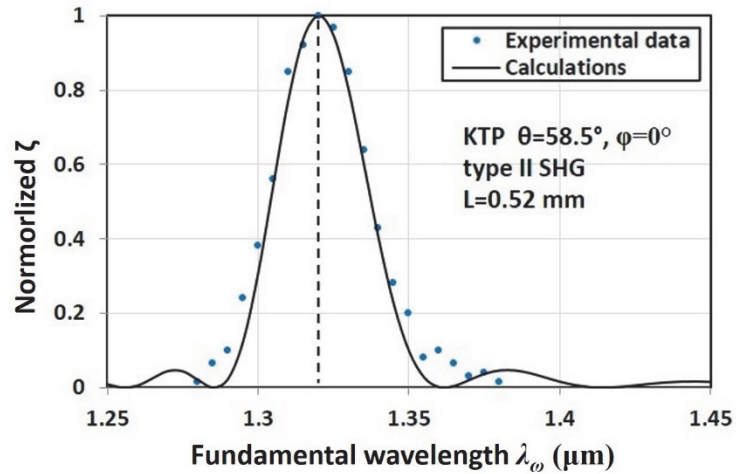


Figure 3.24 Calculated (black line) and measured (dots) ratio ζ in KTP, as a function of the fundamental wavelength.

Once the fundamental wavelength was determined for each sample, the incident energy at the wavelength λ_{ω}^i (with $i = \text{LGN or KTP}$) was measured with the J4-09 Molelectron pyroelectric joulemeter placed behind a beam splitter

through a lens with a focal length of 50 mm, while the energy at $\lambda_{2\omega}^i$ in LGN and KTP was measured with the J3-05 Molelectron pyroelectric joulemeter combined with a PEM531 amplifier, a filter removing the input beam.

Under the phase-matching condition ($\Delta k = 0$) and according to Eqs (2.27), (2.28) and (2.29) described in § 2.3, the ratio between ζ_{LGN} and ζ_{KTP} is:

$$\frac{\zeta_{LGN}}{\zeta_{KTP}} = \frac{L_{LGN}^2 \frac{A^{LGN}}{(\lambda_{\omega}^{LGN})^2} G^{LGN} (d_{eff}^{LGN})^2}{L_{KTP}^2 \frac{A^{KTP}}{(\lambda_{\omega}^{KTP})^2} G^{KTP} (d_{eff}^{KTP})^2} \quad (3.25).$$

Due to the same thickness of the LGN and KTP slabs, we have $L_{LGN}^2/L_{KTP}^2=1$, so that the effective coefficient of LGN becomes according to the Eq. 2.28:

$$(d_{eff}^{LGN})^2 = \frac{\zeta_{LGN}}{\zeta_{KTP}} \frac{(\lambda_{\omega}^{LGN})^2}{(\lambda_{\omega}^{KTP})^2} \frac{G_{II}^{KTP}}{G_I^{LGN}} \frac{A_{II}^{KTP}}{A_I^{LGN}} (d_{eff}^{KTP})^2 \quad (3.26)$$

with

$$A_I^{LGN} = \frac{T_o^{LGN}(\lambda_{2\omega}^{LGN}, \theta_{PM_1})}{n_o^{LGN}(\lambda_{2\omega}^{LGN}, \theta_{PM_1})} \left[\frac{T_e^{LGN}(\lambda_{\omega}^{LGN})}{n_e^{LGN}(\lambda_{\omega}^{LGN})} \right]^2 \quad (3.27)$$

and

$$A_{II}^{KTP} = \frac{T_o^{KTP}(\lambda_{2\omega}^{KTP})}{n_o^{KTP}(\lambda_{2\omega}^{KTP})} \frac{T_e^{KTP}(\lambda_{\omega}^{KTP}, \theta_{PM_2})}{n_e^{KTP}(\lambda_{\omega}^{KTP}, \theta_{PM_2})} \frac{T_o^{KTP}(\lambda_{\omega}^{KTP})}{n_o^{KTP}(\lambda_{\omega}^{KTP})} \quad (3.28).$$

In equation (3.26), the G_I^{LGN} and G_{II}^{KTP} parameters correspond to the attenuation due to double refraction defined in § 2.3.4. Equations (2.39) for type I SHG in LGN and (2.40) for type II SHG in KTP lead to: $G_I^{LGN} = 0.999$ and

$G_{II}^{KTP} = 0.987$ [4, 59], corresponding to a spatial walk-off angle $\rho^e(\theta_{PM_1}, \lambda_\omega^{LGN}) = 0.55^\circ$ for LGN, and $\rho^e(\theta_{PM_1}, \lambda_\omega^{KTP}) = 2.57^\circ$ for KTP. T_o and T_e are the corresponding Fresnel transmission coefficients. The maximum value of ζ^{LGN}/ζ^{KTP} was measured to be 0.021. According to Eq. (3.26), we found that $|d_{11}(0.659 \text{ } \mu\text{m})| = 2.9 \pm 0.5 \text{ pm/V}$ for LGN [70].

3.5.3.3 Analysis

For comparing the absolute magnitude of d_{11} from Maker fringes and the one from phase-matching measurements, we took $0.532 \text{ } \mu\text{m}$ to be the generated wavelength. Therefore the Miller relation has to be used for calculating d_{11} at $0.532 \text{ } \mu\text{m}$ from d_{11} measured at different wavelengths.

In the framework of the Lorentz model applied to the anharmonic oscillator, it can be shown that the second-order electrical susceptibility tensor depends on the circular frequency (ω). The Miller relation is then defined as following [75]:

$$\chi_{ijk}^{(2)}(\lambda_3) = \delta_{ijk} \chi_{ii}^{(1)}(\lambda_3) \chi_{jj}^{(1)}(\lambda_1) \chi_{kk}^{(1)}(\lambda_2) \quad (3.29)$$

where δ_{ijk} is called the Miller index which is independent of ω , and $1/\lambda_3 = 1/\lambda_1 \pm 1/\lambda_2$. Thus any element of the second-order nonlinear electrical susceptibility tensor ($\chi_{ijk}^{(2)}$) can be expressed as a function of the elements of the first-order electrical susceptibility tensor ($\chi_{aa}^{(1)}$), that depends on the principle refractive index n_a through $\chi_{aa}^{(1)} = n_a^2 - 1$ (with $a = i, j$ or k).

Then the $|d_{11}(0.532 \mu\text{m})|$, which is the contracted notation of $|d_{xxx}(0.532 \mu\text{m})|$, can be calculated from $|d_{11}(0.659 \mu\text{m})|$ by using Miller relation (Eq. (3.29)) and the Sellmeier equations given by Eq. 3.16 and Tab. 3.5, *i.e.*:

$$\begin{aligned} & |d_{11}(0.532 \mu\text{m})| \\ = & |d_{11}(0.659 \mu\text{m})| \frac{(n_x^2(0.532\mu\text{m}) - 1)(n_x^2(1.064\mu\text{m}) - 1)^2}{(n_x^2(0.659\mu\text{m}) - 1)(n_x^2(1.318\mu\text{m}) - 1)^2} \end{aligned} \quad (3.30).$$

The value of $|d_{11}(0.532 \mu\text{m})|$ from phase-matching measurement is found to be 3.02 ± 0.52 pm/V, while the value is 3.0 ± 0.1 pm/V measured by the Maker fringes method. The agreement is then perfect. This value is also very close to $|d_{24}(0.532 \mu\text{m})| = 2.51 \pm 0.13$ pm/V of KTP [59], and to $|d_{11}(0.532 \mu\text{m})| = 2.62 \pm 0.44$ pm/V of LGT [33].

3.5.4 Calculation of supercontinuum conditions

The previous parts refer to the main basic optical properties of LGN. It is now interesting to study the potentiality of LGN for generating a supercontinuum by optical parametric generation, *i.e.* OPG ($1/\lambda_p = 1/\lambda_s + 1/\lambda_i$). Here λ_p stands for the pump wavelength, λ_s is the wavelength of the signal, and λ_i is for the idler wavelength, with $\lambda_p < \lambda_s \leq \lambda_i$.

A supercontinuum can be generated only during a type II interaction, *i.e.*, λ_i^e , λ_s^e and λ_p^o where “o” and “e” refer to the ordinary and extraordinary polarizations, respectively [76]. The pump wavelength, that we write λ_p^* , for which a broadband spectrum (supercontinuum) is generated, corresponds to the wavelength for which the dispersion of the extraordinary refractive index n^e of a positive uniaxial crystal as LGN has an inflection point, *i.e.* [76, 77]:

$$\left. \frac{\partial^2 n^e(\lambda, \theta)}{\partial \lambda^2} \right|_{\lambda^* = 2\lambda_p^*} = 0 \quad (3.31).$$

Using our refined Sellmeier equations (Eq. 3.16, Fig. 3.18) [70] and the method described in ref [76], we showed that a supercontinuum can be generated when LGN is pumped at $\lambda_p = 0.982 \mu\text{m}$ and cut at $(\theta_{PM} = 52^\circ, \varphi = 90^\circ)$: Figure 3.25 shows that the emission ranges between 1.4 and $3.45 \mu\text{m}$. Concerning the pump laser to use, Figure 3.25 shows that the tuning curve of LGN exhibits a quasi-supercontinuum behavior when the crystal is pumped at the Nd:YAG wavelength ($\lambda_p = 1.064 \mu\text{m}$), while it is not anymore the case at the Ti:Sapphire wavelength ($\lambda_p = 0.8 \mu\text{m}$).

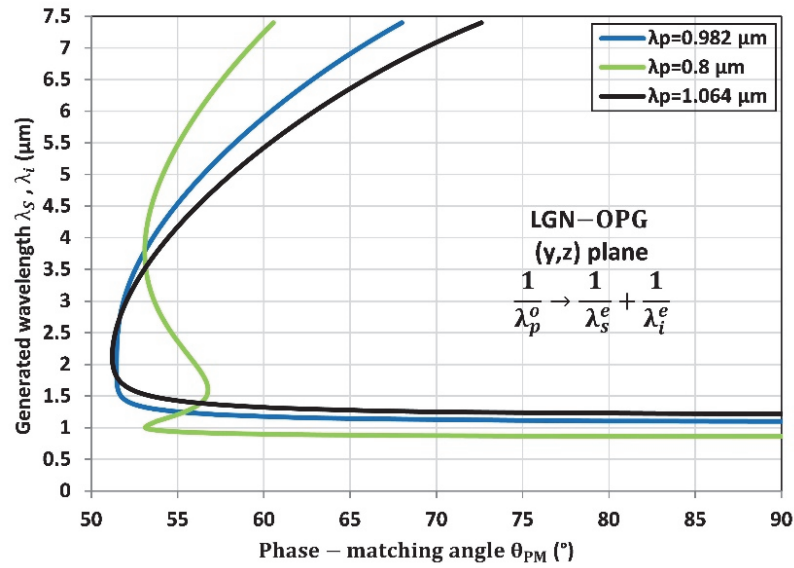


Figure 3.25 Calculated OPG tuning curves in the (y, z) plane of LGN at different values of the pump wavelength λ_p .

3.6 Summary and discussion

We grew large size of the new Langanite crystal $\text{La}_3\text{Ga}_{5.5}\text{Nb}_{0.5}\text{O}_{14}$ (LGN). The linear and second-order nonlinear optical properties have been studied in detail: we found that the transparency is ranging between 0.28 and 7.4 μm , we determined accurate Sellmeier equations, and we determined that the nonlinear coefficient d_{ii} is around 3.0 pm/V. Using our Sellmeier equations, we identified the possibility of generating a supercontinuum in the mid-IR by pumping LGN at the standard wavelength of emission of the Nd:YAG laser. From these results, LGN appears as a promising crystal for high energy generation in band II of transmission of the atmosphere, for Lidar applications for example. It gives also inspiration for the study and development of other nonlinear crystals from the same chemical family.

The relevant parameters of the reference nonlinear crystals for the emission between 2 and 6 μm *i.e.* PPLN, PPKTP, LBO, KTP, LGT and LGN are depicted in Table 3.6. We show that LGN has a transparent range covering the atmosphere transparency range band II. Furthermore, we report phase-matching tuning curves over this transparency range, and a relatively high damage threshold of this crystal. The nonlinear coefficient d_{ii} of LGN is a little bit higher than that of LGT. However, LGN crystallizes in the 32 point group as LGT, which leads to an unfavorable trigonometric function at the level of the effective coefficient d_{eff} when compared to other nonlinear crystals of Table 3.6. Fortunately, this disadvantage can be compensated by the fact that LGN (as LGT) can be grown with large dimensions. Then LGN permits firstly the use of a large beam diameter so that a very high energy can be considered while remaining below the intensity damage threshold, and secondly it enables a long interacting length that is favorable for maximizing the conversion efficiency. Note that nowadays, the biggest aperture for a LGS crystal is 52 mm \times 100 mm

[78]. Then we think that LGN can be grown as large as LGS after optimizing our crystal growth techniques.

Table 3.6 Comparison of LGN with other nonlinear crystals that can be used in OPG for an emission between 2 μm and 6 μm .

Crystal	PPLN	PPKTP	LBO	KTP	LGT	LGN
Point Group	3m	mm2	mm2	mm2	32	32
Transmission range (μm)	0.33~5.5	0.35~4.5	0.16~2.6	0.35~4.5	0.3~6.8	0.28~7.4
Nonlinear coefficient (pm/V)	$d_{33}=31.8$ @0.659 μm	$d_{33}=10.6$ @0.66 μm	$d_{32}=1.17$ @0.54 μm	$d_{24}=2.51$ @0.532 μm	$d_{11}=2.4$ @0.67 μm	$d_{11}=2.9$ @0.659 μm
Damage threshold (GW/cm ²)	0.05~0.06 (1.064 μm ; 10 ns)	>0.9 (1.064 μm ; 5 ns)	25 (1.064 μm ; 0.1 ns)	4.29 (1.064 μm ; 5 ns)	4.34 (1.064 μm ; 5 ns)	2.9 (1.064 μm ; 5 ns)
Idler tunability (μm)	3.2~3.8/3.8~4.3	2.128~4	1.08~2.85	0.9~4.5	1.4~4.7	1.4~6.5
References	[79-83]	[59, 84, 85]	[25, 79, 86, 87]	[5, 59, 88-93]	[33, 34, 94]	[70, 71, 92]

4 PPRKTP crystal

4.1 State of the art and motivations

As seen in Chapter II, nonlinear optics deals with a strong coupling between light and matter. Its ability to convert and tune the frequency range of existing laser sources is of prime importance in optical devices [12, 95]. It was also explained in Chapter II that phase-matching conditions have to be fulfilled in order to obtain and improve frequency conversion during the nonlinear process. The common way for obtaining phase-matching is to use birefringence phase-matching (BPM) as it was done in the case of LGN and described in Chapter III [12, 71, 92, 96]. The present chapter is devoted to the study of quasi-phase-matching (QPM) that is performed in an artificial medium in which there is a periodic modulation of the sign of the crystal's second-order nonlinear coefficient. This modulation can be realized in one or two dimensions [15, 97], and it gives the possibility to access to the highest coefficient of the second-order electric susceptibility tensor [15, 16] or to shape the spatial and spectral properties of light [98]. Recently, significant improvement of the electric field poling or bonding techniques have led to larger aperture QPM crystals. For example, few-millimeters-thick periodically poled 5%MgO:LiNbO₃ (5%MgO:PPLN) [99], LiTaO₃ (PPLT) [100], KTiOPO₄ (PPKTP) [101], Rb-doped KTiOPO₄ (PPRKTP) [102] and orientation-patterned GaAs (OP-GaAs) [103] have been successfully obtained. Such large-size artificial materials not only allow laser beams with large apertures and high energies to be used, but they also give the possibility to implement the angular quasi-phase-matching (AQPM) scheme proposed in 2007 [2]. It corresponds to a generalization of QPM since it can be achieved at any angle with respect to the grating vector of the artificial nonlinear medium. This scheme was validated for the first time in

2009 by using a uniaxial crystal, concretely a sphere shaped 5% MgO:PPLN [66]. By studying second-harmonic generation (SHG) and difference-frequency generation (DFG), it had been shown in particular that AQPM brings giant spectral acceptances compared with BPM.

In this chapter, we report the first general validation of the AQPM scheme in the case of a biaxial crystal using SHG. We considered a crystal of PPRKTP because it can be obtained in larger size than PPKTP [101] and with a reliable control of the ferroelectric-domain structures [102]. The composition of the crystal we study is $\text{Rb}_{0.003}\text{K}_{0.997}\text{TiOPO}_4$, and its grating period is $\Lambda = 38.52 \mu\text{m}$ [104].

4.2 Theoretical analysis

The AQPM condition is given by the following equation described in § 2.3.2 of Chapter II [2]:

$$\frac{n_3^\pm(\theta, \varphi)}{\lambda_3} - \frac{n_2^\pm(\theta, \varphi)}{\lambda_2} - \frac{n_1^\pm(\theta, \varphi)}{\lambda_1} - \frac{1}{\Lambda_{\text{eff}}(\theta, \varphi)} = 0 \quad (4.1)$$

θ and φ are the angles of spherical coordinates in the dielectric frame (x, y, z) . λ_1 , λ_2 and λ_3 are the wavelengths of the three interacting waves that are linked by energy conservation, *i.e.* $\lambda_3^{-1} = \lambda_2^{-1} + \lambda_1^{-1}$; n_1^\pm , n_2^\pm and n_3^\pm are the corresponding refractive indices in the considered AQPM direction (θ, φ) , the signs + and - denoting the two possible values of the refractive index according to birefringence. In the following, the notations $\lambda_\omega (= \lambda_1 = \lambda_2)$ and $\lambda_{2\omega} (= \lambda_3)$ for the fundamental and second-harmonic (SH) wavelengths respectively will be used.

$\Lambda_{\text{eff}}(\theta, \varphi) = \Lambda |\sin(\theta) \cos(\varphi)|^{-1}$ is the effective grating periodicity in the

direction (θ, φ) that has been defined in § 2.3.2 : it ranges from a minimal value corresponding to a propagation of the interacting waves along the x -axis, *i.e.* $\Lambda_{\text{eff}}(\theta = 90^\circ, \varphi = 0^\circ) = \Lambda$, to a maximal one obtained when propagation occurs in the y - z plane, *i.e.* $\Lambda_{\text{eff}}(\theta, \varphi = 90^\circ) \rightarrow \infty$. Note that AQPM authorizes six possible combinations of refractive indices in Eq. (4.1) for SHG, which defines the six SHG AQPM types, BPM exhibiting only two of them[2, 96].

The Sellmeier equations of RKTP are not known, therefore we used those of KTP since the Rubidium (Rb) concentration is small (0.3%). Then we used the Sellmeier equations of Ref. [105] for the calculation of the SHG AQPM angles. We found that only four SHG AQPM types are allowed among the six possible types, and that for fundamental wavelengths above $2.098 \mu\text{m}$. At this wavelength, type V AQPM exists only along the x -axis, and it disappears for smaller wavelengths. We chose $2.15 \mu\text{m}$ as fundamental wavelength, which was close to the cut-off of the source we used. The four AQPM relations are given in Tab. 4.1, as well as those of types I and II BPM that are allowed in RKTP. Note that the corresponding phase-matching relations can be obtained from those of types I and II AQPM given in Tab. 4.1 by doing $\Lambda_{\text{eff}}(\theta, \varphi) \rightarrow \infty$. The consideration of BPM in this framework of AQPM is relevant from the experimental point of view as it will be shown hereafter.

Figure 4.1 shows the tuning curves of the corresponding AQPM and BPM angular tuning curves at $\lambda_\omega = 2.15 \mu\text{m}$.

Table 4.1 Possible SHG AQPM and BPM types in PPRKTP; n^+ and n^- are the two possible values of the refractive index at the fundamental or second harmonic wavelengths, λ_ω and $\lambda_{2\omega}$ respectively, in the PM direction (θ, φ) .

Types	AQPM relations
I	$n_{2\omega}^-(\theta, \varphi) \lambda_{2\omega}^{-1} = 2n_{\omega}^+(\theta, \varphi) \lambda_{\omega}^{-1} + \Lambda_{eff}^{-1}(\theta, \varphi)$
II	$n_{2\omega}^-(\theta, \varphi) \lambda_{2\omega}^{-1} = n_{\omega}^+(\theta, \varphi) \lambda_{\omega}^{-1} + n_{\omega}^-(\theta, \varphi) \lambda_{\omega}^{-1} + \Lambda_{eff}^{-1}(\theta, \varphi)$
IV	$n_{2\omega}^-(\theta, \varphi) \lambda_{2\omega}^{-1} = 2n_{\omega}^-(\theta, \varphi) \lambda_{\omega}^{-1} + \Lambda_{eff}^{-1}(\theta, \varphi)$
V	$n_{2\omega}^+(\theta, \varphi) \lambda_{2\omega}^{-1} = 2n_{\omega}^+(\theta, \varphi) \lambda_{\omega}^{-1} + \Lambda_{eff}^{-1}(\theta, \varphi)$

Types	BPM relations
I	$n_{2\omega}^-(\theta, \varphi) \lambda_{2\omega}^{-1} = 2n_{\omega}^+(\theta, \varphi) \lambda_{\omega}^{-1}$
II	$n_{2\omega}^-(\theta, \varphi) \lambda_{2\omega}^{-1} = n_{\omega}^+(\theta, \varphi) \lambda_{\omega}^{-1} + n_{\omega}^-(\theta, \varphi) \lambda_{\omega}^{-1}$

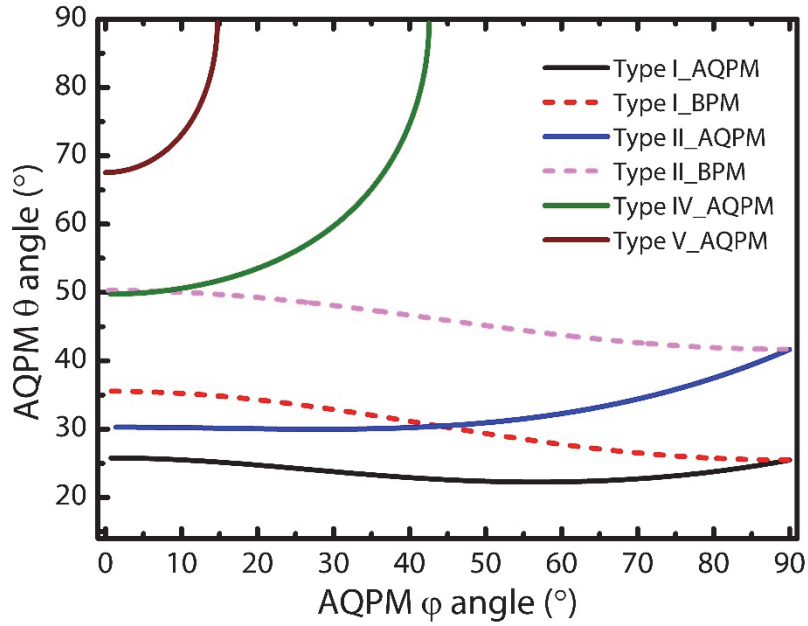


Figure 4.1 All the possible SHG AQPM and BPM curves calculated in PPRKTP pumped at a wavelength of $2.15 \mu\text{m}$ are shown as solid and dashed lines, respectively.

As PPRKTP belongs to the crystal class $mm2$, there exist five independent nonlinear coefficients in the case of SHG, *i.e.* using the contracted notation: d_{15} , d_{24} , d_{31} , d_{32} and d_{33} [4].

Thus the effective coefficient corresponding to any SHG AQPM direction (θ, φ) can be calculated using the following equation:

$$d_{eff}(\theta, \varphi) = \frac{2}{\pi} \left[\begin{array}{l} d_{15}(2\omega)(F_{xz}(\theta, \varphi) + F_{zxx}(\theta, \varphi)) \\ + d_{24}(2\omega)(F_{yyz}(\theta, \varphi) + F_{yzy}(\theta, \varphi)) \\ + d_{31}(2\omega)F_{zxx}(\theta, \varphi) + d_{32}(2\omega)F_{zyy}(\theta, \varphi) \\ + d_{33}(2\omega)F_{zzz}(\theta, \varphi) \end{array} \right] \quad (4.2)$$

with

$$F_{ijk}(\theta, \varphi) = e_i^\pm(2\omega, \theta, \varphi) e_j^\pm(\omega, \theta, \varphi) e_k^\pm(\omega, \theta, \varphi) \quad (4.3).$$

The index i stands for x, y or z , and e_a^\pm ($a = i, j, k$) represent the unit vectors of the electric fields of the different interacting waves corresponding to the refractive indices of Tab. 4.1 according to the type that is considered. The expressions of unit electric field vectors \vec{e}^\pm and the field tensors F_{ijk} are presented as in Eqs. (2.13) and (2.25) of Chapter II. The expressions of the five relevant coefficients in the contracted notation are the following:

$$\begin{aligned} F_{15}(\theta, \varphi) &= F_{xz}(\theta, \varphi) + F_{zxx}(\theta, \varphi) = 2e_x^\pm(2\omega, \theta, \varphi) e_x^\pm(\omega, \theta, \varphi) e_z^\pm(\omega, \theta, \varphi) \\ F_{24}(\theta, \varphi) &= F_{yyz}(\theta, \varphi) + F_{yzy}(\theta, \varphi) = 2e_y^\pm(2\omega, \theta, \varphi) e_y^\pm(\omega, \theta, \varphi) e_z^\pm(\omega, \theta, \varphi) \\ F_{31}(\theta, \varphi) &= F_{zxx}(\theta, \varphi) = e_z^\pm(2\omega, \theta, \varphi) e_x^\pm(\omega, \theta, \varphi) e_x^\pm(\omega, \theta, \varphi) \\ F_{32}(\theta, \varphi) &= F_{zyy}(\theta, \varphi) = e_z^\pm(2\omega, \theta, \varphi) e_y^\pm(\omega, \theta, \varphi) e_y^\pm(\omega, \theta, \varphi) \\ F_{33}(\theta, \varphi) &= F_{zzz}(\theta, \varphi) = e_z^\pm(2\omega, \theta, \varphi) e_z^\pm(\omega, \theta, \varphi) e_z^\pm(\omega, \theta, \varphi) \end{aligned} \quad (4.4)$$

These field tensor coefficients are calculated using the Sellmeier equations of reference[105] for the four AQPM types of PPRKTP pumped at the

fundamental wavelength $\lambda_\omega = 2.15 \mu\text{m}$. They are plotted as a function of the phase-matching angle φ in Fig. 4.2.

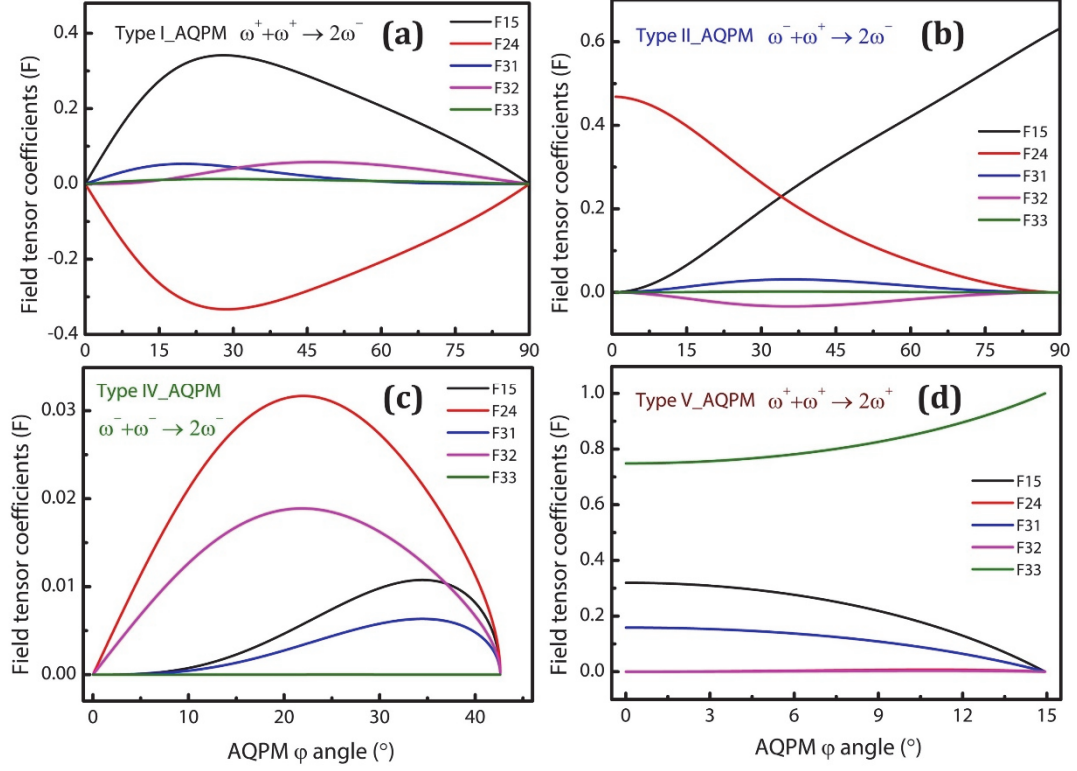


Figure 4.2 Field tensor coefficients as a function of the AQPM angle φ for the four SHG AQPM types in PPRKTP pumped at a wavelength of $2.15 \mu\text{m}$.

The calculation of the effective coefficients d_{eff} corresponding to the field tensor coefficients of Fig. 4.2 requires to know the magnitude of the five independent nonlinear coefficients, *i.e.* d_{15} , d_{24} , d_{31} , d_{32} and d_{33} of PPRKTP at the SH working wavelength, *i.e.* $\lambda_{2\omega} = \lambda_\omega/2 = 1.075 \mu\text{m}$. For that we used the Miller rule[75]. Using this law, it is indeed possible to calculate the value of any $\chi_{ijk}^{(2)}$ coefficient at any wavelength $\omega_A = \omega_{A1} \pm \omega_{A2}$ knowing the value of this coefficient at a given wavelength $\omega_B = \omega_{B1} \pm \omega_{B2}$ on the one hand, and the values of the principal refractive indices at all the wavelengths that are concerned. Then the coefficients $\chi_{ijk}^{(2)}(\omega_A)$ and $\chi_{ijk}^{(2)}(\omega_B)$ are related by the relation

$$\chi_{ijk}^{(2)}(\omega_A = \omega_{A1} \pm \omega_{A2}) = \chi_{ijk}^{(2)}(\omega_B = \omega_{B1} \pm \omega_{B2}) \cdot \frac{\chi_{ii}^{(1)}(\omega_A)\chi_{jj}^{(1)}(\omega_{A1})\chi_{kk}^{(1)}(\pm\omega_{A2})}{\chi_{ii}^{(1)}(\omega_B)\chi_{jj}^{(1)}(\omega_{B1})\chi_{kk}^{(1)}(\pm\omega_{B2})} \quad (4.5)$$

where $\chi_{aa}^{(1)}(\omega) = n_a^2(\omega) - 1$ ($a = i, j$ and k).

Using Eq. (4.5), the nonlinear coefficients at $\lambda_{\omega B} = 0.532 \mu\text{m}$ given in reference [106], we got for the nonlinear coefficients at $\lambda_{\omega A} = 1.075 \mu\text{m}$: $d_{15} = 1.199 \text{ pm/V}$, $d_{24} = 2.27 \text{ pm/V}$, $d_{31} = 1.19 \text{ pm/V}$, $d_{32} = 2.25 \text{ pm/V}$ and $d_{33} = 8.97 \text{ pm/V}$.

From these values the effective coefficients corresponding to the four SHG AQPM types in PPRKTP pumped at $\lambda_{\omega} = 2.15 \mu\text{m}$ are plotted in Fig. 4.3 as a function of the angle φ .

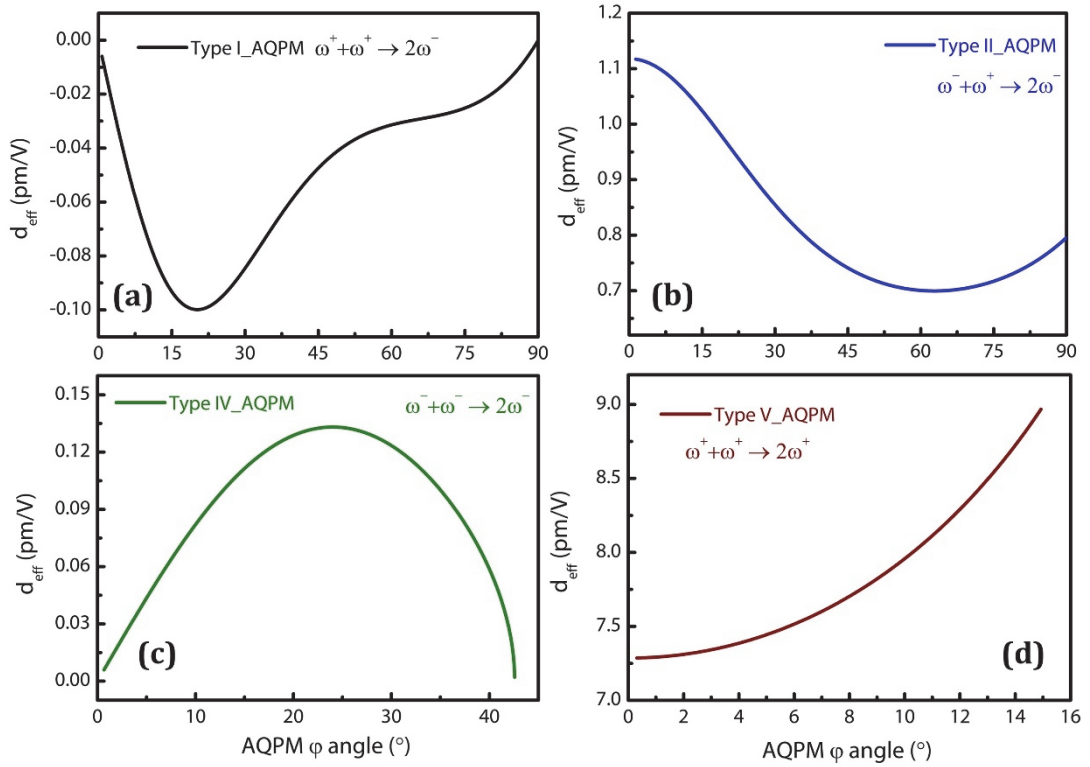


Figure 4.3 Effective coefficients d_{eff} as a function of the AQPM angle φ for the four SHG AQPM types in PPRKTP pumped at a wavelength of $2.15 \mu\text{m}$.

Note that the only cases for which the effective coefficient is zero are those of types I and IV in the principal planes, as shown in Fig. 4.3. Note also that in the case of a biaxial crystal, which is the case of PPRKTP, the effective coefficient has an analytical expression only in the principal planes. Table 4.2 gives the corresponding expressions of the types for which the effective coefficient is non zero, *i.e.* of types II and V.

Table 4.2 Non zero effective coefficients of the four types of SHG AQPM in the principle planes; ρ is the Poynting walk-off angle.

Types	Planes	Effective coefficients (d_{eff})
II	(x, z)	$(2/\pi) \cdot d_{24} \sin(\theta - \rho_\omega(\theta))$
	(y, z)	$(2/\pi) \cdot d_{15} \sin(\theta - \rho_\omega(\theta))$
V	(x, y)	$(2/\pi) \cdot d_{33}$
	(x, z)	$\left(\frac{2}{\pi}\right) \left[2d_{15} \sin(\theta - \rho_\omega(\theta)) \cos(\theta - \rho_\omega(\theta)) \cos(\theta - \rho_{2\omega}(\theta)) \right. \\ \left. + \sin(\theta - \rho_{2\omega}(\theta)) (d_{31} \cos^2(\theta - \rho_\omega(\theta)) + d_{33} \sin^2(\theta - \rho_\omega(\theta))) \right]$

The five coefficients of the field tensor of the BPM SHG can be calculated using the same equations than those of AQPM, *i.e.* Eqs. 4.4. They are plotted in Figs. 4.4(a) and (b) as a function of the BPM angle in the case of the SHG pumped at $2.15 \mu\text{m}$. From these coefficients it is easy to calculate the effective coefficients of the SHG of types I and II using Eqs. 4.2 without the factor $2/\pi$, and the Miller rule described above; they are plotted in Figs. 4.4 (c) and (d), respectively.

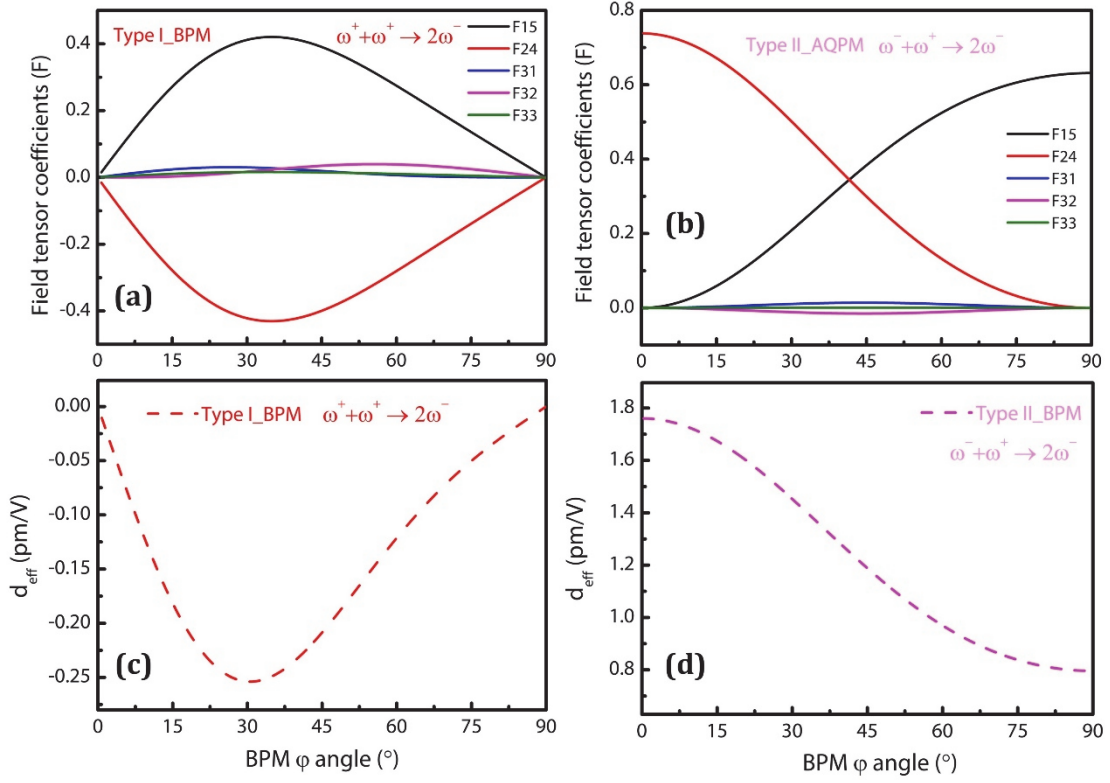


Figure 4.4 Field tensor coefficients for Type I (a) and II (b) SHG BPM, and effective coefficients for Type I (c) and II (d) SHG BPM as a function of the BPM angle φ in PPRKTP pumped at a wavelength of $2.15 \mu\text{m}$.

4.3 Measurements

In order to determine at best the full angular distribution of AQPM, we shaped the PPRKTP crystal as a sphere using a specific technique allowing us to get a perfect polishing and an asphericity below 1% [58]. We got a sphere with a diameter of 4.76 mm, as shown in Fig. 4.5 (a), the volume of the sphere being fully periodically poled as shown in Fig. 4.5 (b).

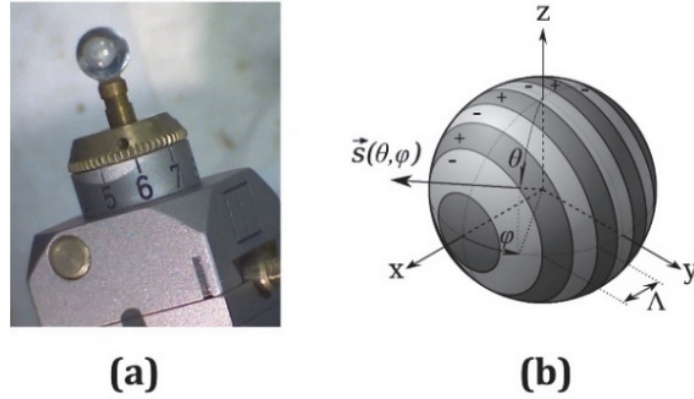


Figure 4.5 (a) PPRKTP sphere used for the experiments. (b) Scheme of AQPM in the sphere where Λ is the grating periodicity along the x -axis and $\vec{s}(\theta, \varphi)$ is the unit vector of the wave vectors of the interacting waves where (θ, φ) are the angle of spherical coordinates in the dielectric frame (x, y, z) .

As seen in Fig. 4.1, all the tuning curves range between the (x, z) and the (x, y) or (y, z) planes, which determine a specific strategy for scanning the space in order to measure at best the corresponding phase-matching angles, as shown in Fig. 4.6. The method consists in rotating the sphere around the z -axis by incremental values of the angle φ (φ -Scanning), and, for each value of φ , the sphere is then rotated by the angle θ (θ -Scanning) until the fundamental beam and the phase-matching direction are in coincidence in the plane that is considered. The best choice was to stick the sphere along the y -axis since one cone surrounds the x -axis and the other one the z -axis. A Laue orientation of the sphere gives us a precision better than 0.05° .

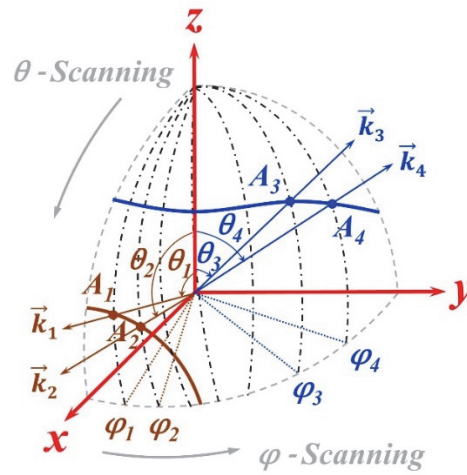


Figure 4.6 Schematic diagram of the scanning mode for determining the two possible topologies of phase-matching cones, i.e. around the x -axis (brown) or z -axis (blue). The \vec{k}_i ($i = 1, 2, 3, 4$) correspond to the phase-matching directions at the angles θ_i and φ_i crossing the cones at A_i . (x, y, z) is the dielectric frame.

The sphere was then placed at the center of a Kappa circle described in Fig.

4.7.

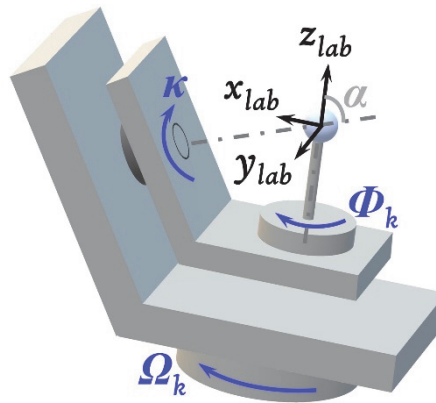


Figure 4.7 Kappa circle consisting of three rotation angles marked by the axes κ , Φ_k and Ω_k ; $(x_{lab}, y_{lab}, z_{lab})$ is the laboratory frame.

The Kappa circle is motorized by stepper motors with an accuracy of 0.003° and is electronically controlled. It has three rotation axes κ , Φ_k and Ω_k . The three

rotation axes κ , Φ_k and Ω_k are arranged in such a way that the axis of rotation κ is placed at a non-zero angle (α) with respect to the vertical direction. This arrangement enables multiple combinations between the three axes for a same direction, which allowed us to choose the combination for which we had no “blind spot”.

The phase-matching angles have to be known in terms of their angle of spherical coordinates (θ , φ) in the dielectric frame (x , y , z), but their measurement is performed using the Kappa circle that gives the three angles (Ω_k , κ , Φ_k) defined according to the laboratory frame (x_{lab} , y_{lab} , z_{lab}) as shown in Fig. 4.7. The relative orientation between the laboratory and dielectric frames is described in shown in Fig. 4.8.

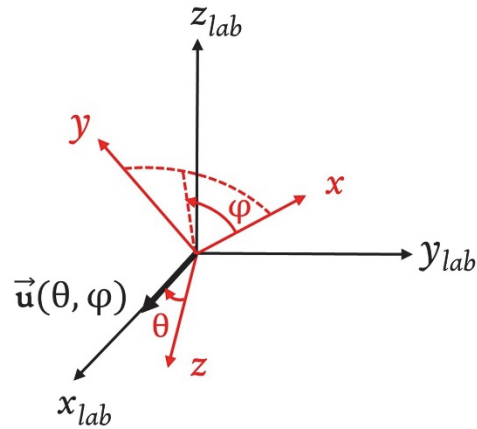


Figure 4.8 (x_{lab} , y_{lab} , z_{lab}) are the principal axes of the laboratory frame ; the spherical coordinates (θ , φ) are relative to the propagation direction $\vec{u}(\theta, \varphi)$ in the dielectric frame (x , y , z).

A change of the reference is then required for determining the relationship between the spherical coordinate angles (θ , φ) and the Kappa angles (Ω_k , κ , Φ_k). We use the following equation between the Cartesian coordinates (u_x, u_y, u_z) in the dielectric frame and the Cartesian coordinates ($u_{xlab}, u_{ylab}, u_{zlab}$) in the laboratory frame :

$$\begin{bmatrix} u_x \\ u_y \\ u_z \end{bmatrix} = M \begin{bmatrix} u_{xlab} \\ u_{ylab} \\ u_{zlab} \end{bmatrix} \quad (4.6)$$

where

$$M = \Gamma_{Zlab}(\Phi_k) \cdot \Gamma_{Ylab}(\alpha) \cdot \Gamma_{Zlab}(\kappa) \cdot \Gamma_{Ylab}(-\alpha) \cdot \Gamma_{Zlab}(\Omega_k) \quad (4.7)$$

with

$$\Gamma_{Zlab}(\Phi_k) = \begin{bmatrix} \cos\Phi_k & -\sin\Phi_k & 0 \\ \sin\Phi_k & \cos\Phi_k & 0 \\ 0 & 0 & 1 \end{bmatrix}$$

$$\Gamma_{Ylab}(\alpha) = \begin{bmatrix} \cos\alpha & 0 & -\sin\alpha \\ 0 & 1 & 0 \\ \sin\alpha & 0 & \cos\alpha \end{bmatrix} \quad (4.8)$$

$$\Gamma_{Zlab}(\kappa) = \begin{bmatrix} \cos\kappa & -\sin\kappa & 0 \\ \sin\kappa & \cos\kappa & 0 \\ 0 & 0 & 1 \end{bmatrix}$$

$$\Gamma_{Zlab}(\Omega_k) = \begin{bmatrix} \cos\Omega_k & -\sin\Omega_k & 0 \\ \sin\Omega_k & \cos\Omega_k & 0 \\ 0 & 0 & 1 \end{bmatrix} \quad (4.9)$$

And finally we get:

$$\begin{cases} \theta = \arccos(u_z) \\ \phi = \arctan\left(\frac{u_y}{u_x}\right) \end{cases} \quad (4.10).$$

For this change of frame, we have written a usable interfacing program with a command system of a motor positioning allowing a given direction (θ , φ) to be selected. For all possible combinations (Ω_k , κ , Φ_k), the program ensures the following steps: 1) calculation of the coordinates of $\vec{u}(\theta, \varphi)$ in the dielectric frame according to the Eq. 4.6 using Eqs. 4.7, 4.8 and 4.9; 2) calculation of the corresponding solutions (θ , φ) from Eq. (4.10); 3) test of the correspondence of the solutions with the command for each combination. Afterwards, a procedure will run for finding solutions by means of iteration and quick targeting. The

program will repeat this operation until the accuracy of the solution is well matched with the initial command.

The advantage of Kappa circle is that there are a large number of combinations $(\Omega_k, \kappa, \Phi_k)$ corresponding to the same (θ, φ) . Hence, if the mechanical support of the goniometer blocks the laser beam, which corresponds to a dead angle situation, there is the possibility to move it in order to find new angles $(\Omega_k, \kappa, \Phi_k)$ enabling a position without blocking.

The PPRKTP sphere is cut along the y -axis and it was illuminated by a beam at the fundamental wavelength $\lambda_\omega = 2.15 \mu\text{m}$. It was emitted by an optical parametric oscillator that delivers 5-ns-FWHM pulses at 10-Hz-repetition rate. A half-wave plate allowed the incident beam to be polarized according to the chosen AQPM types. A focusing lens was properly located at the entrance of the sphere, ensuring the quasi-parallel propagation of the beams inside the sample. The energy of the generated beam was measured at the exit of the sphere by an amplified Si Hamamatsu C2719 photodiode placed after a 75-mm-focusing lens, a filter removing the fundamental beam. The experimental setup was presented in Fig. 4.9. The phase-matching wavelengths were controlled by a NIRquest 512 Ocean Optics spectrometer with an accuracy of $\pm 3 \text{ nm}$. The SHG phase-matching angles are detected when the associated conversion efficiency is maximal. The corresponding angular accuracy is of $\pm 0.5^\circ$.

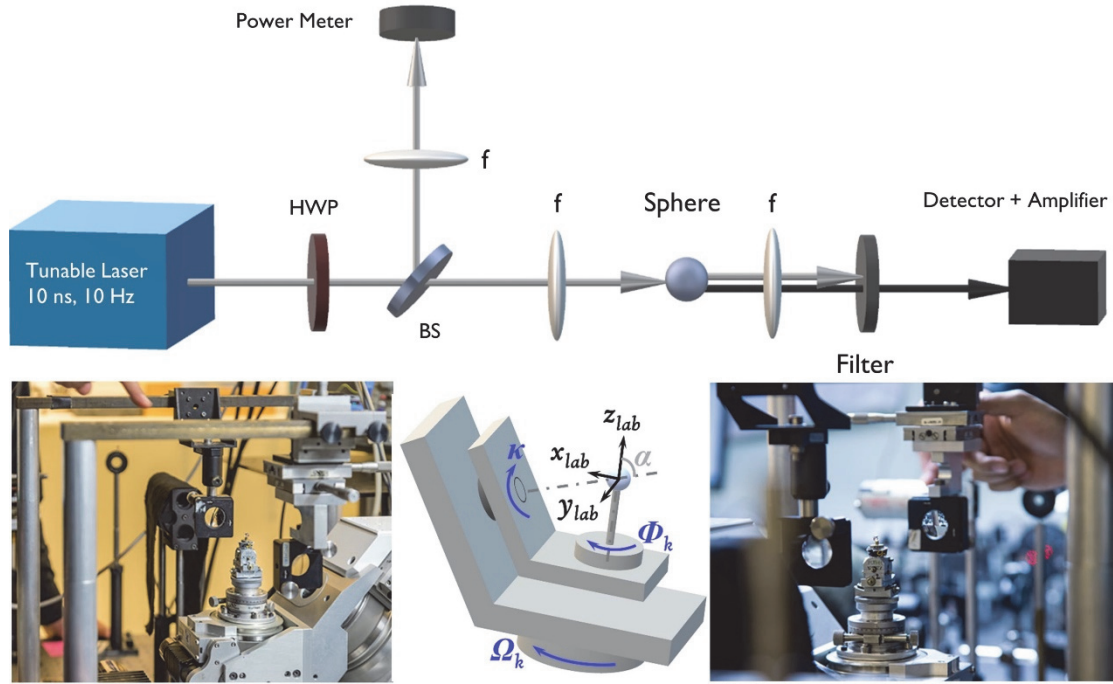


Figure 4.9 Experimental setup for the AQPM measurements in the PPRKTP sphere.

4.4 Results and discussions

Figure 4.10 (a) gives the example of the determination of the type V AQPM angle at $\lambda_\omega = 2.15 \mu\text{m}$ in the (x, z) plane of the PPRKTP sphere. Meanwhile, the conversion efficiency as a function of the fundamental wavelength (λ_ω) is also measured for validating the angular measurement: actually the peak of the AQPM curve is well at $\lambda_\omega = 2.15 \mu\text{m}$ as shown in Fig. 4.10 (b). The same determinations in the (x, z) plane for Type II AQPM and Type II BPM are presented in Fig. 4.11 and 4.12, respectively.

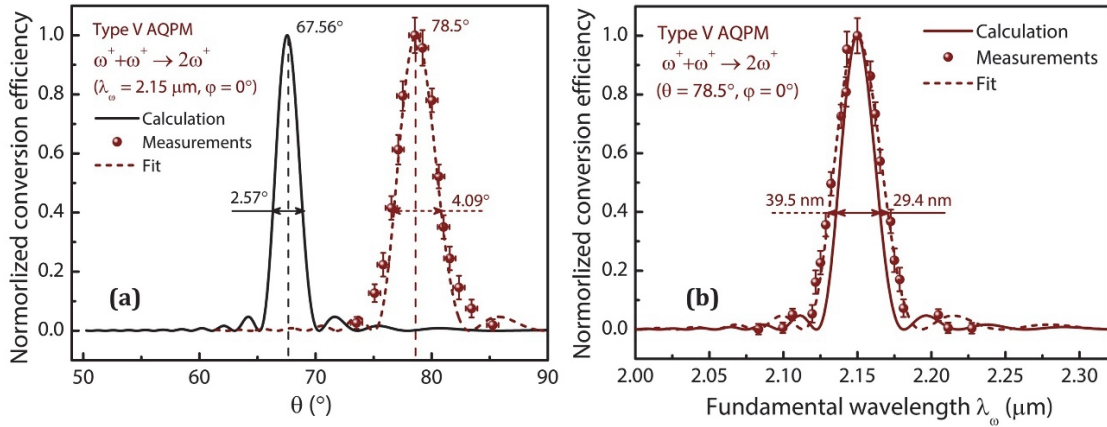


Figure 4.10 (a) Measured (dots fitted by dashed line) and calculated (solid line) SHG conversion efficiency as a function of θ angle for Type V AQPM; (b) Measured (dots fitted by dashed line) and calculated (solid line) SHG conversion efficiency as a function of the fundamental wavelength (λ_ω) for Type V AQPM.

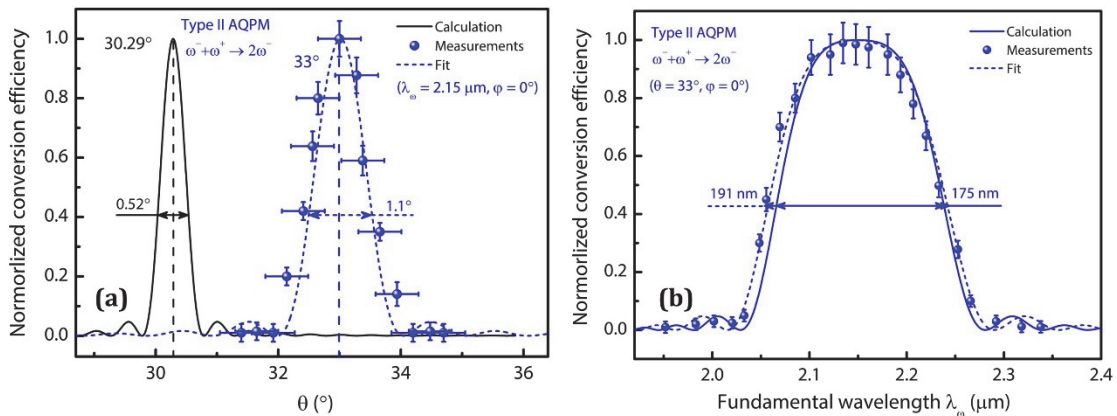


Figure 4.11 (a) Measured (dots fitted by dashed line) and calculated (solid line) SHG conversion efficiency as a function of θ angle for Type II AQPM; (b) Measured (dots fitted by dashed line) and calculated (solid line) SHG conversion efficiency as a function of the fundamental wavelength (λ_ω) for Type II AQPM.

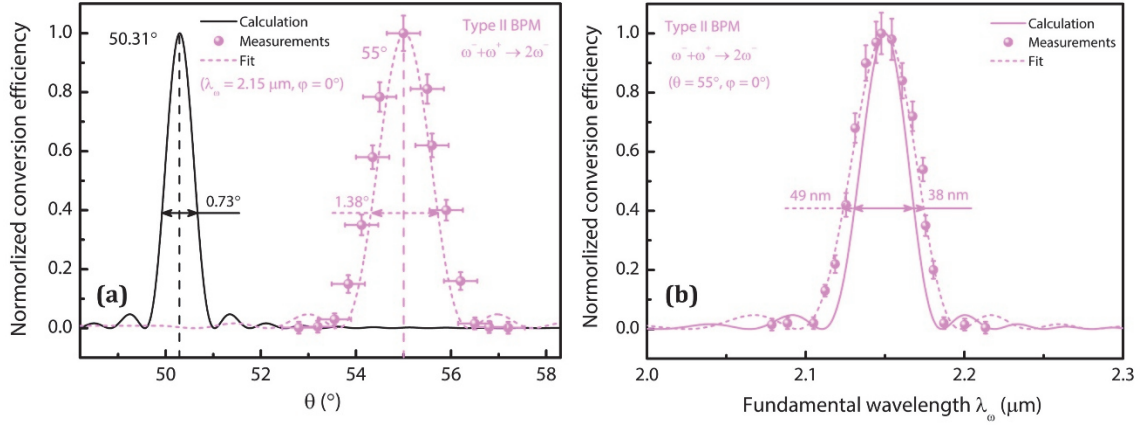


Figure 4.12 (a) Measured (dots fitted by dashed line) and calculated (solid line) SHG conversion efficiency as a function of θ angle for Type II BPM; (b) Measured (dots fitted by dashed line) and calculated (solid line) SHG conversion efficiency as a function of the fundamental wavelength (λ_ω) of Type II BPM.

Fig. 4.10 clearly shows that the experimental type V AQPM SHG angle in the (x, z) plane is $\theta = 78.5 \pm 0.5^\circ$, which is bigger than the calculated one, *i.e.* 67.56° . This discrepancy is due to the fact that the Sellmeier equations we used for the calculation are those of KTP [105] and not those of PPRKTP that are not yet known, as mentioned above. The experimental and calculated angular and spectral acceptances are also larger than the calculated values, but it is probably mainly due to a small divergence inside the sphere, of about several mrad. Following the scanning process described by Fig. 4.6, we measured the entire angular tuning curves of types I, II, IV and V. As shown in Fig. 4.13, there is a shift of a couple of degrees between measurements and calculations. But the behaviors are the same, and we also confirm the fact that no more than the four calculated AQPM types are allowed, which was the first step in the validation of the AQPM theory in a biaxial crystal.

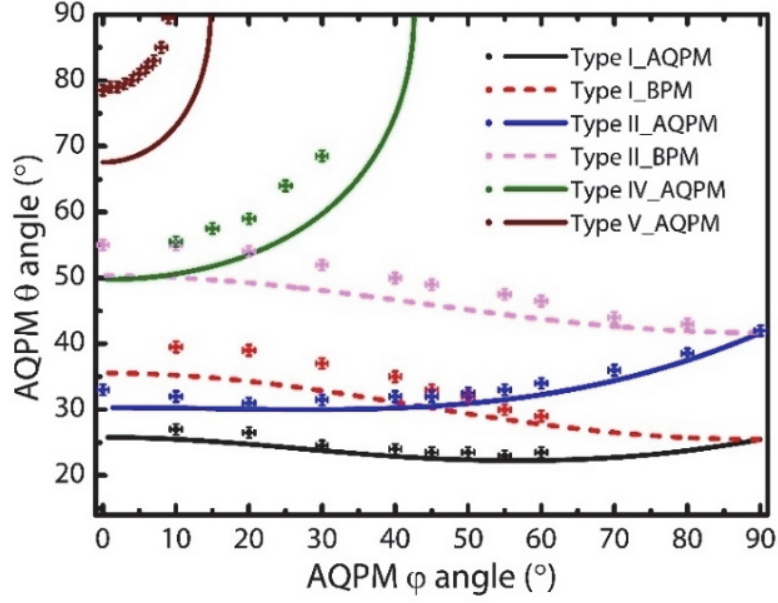


Figure 4.13 All the possible SHG AQPM and BPM curves calculated in PPRKTP pumped at a wavelength of $2.15 \mu\text{m}$ are shown as solid and dashed lines, respectively. Cross dots stands for the experimental data.

The second step of validation has concerned the angular evolution of the effective coefficient. The later one acts at the level of the Figure of Merit (FOM) through the following equation [4]:

$$\text{FOM}(\theta, \varphi) = \frac{d_{\text{eff}}^2(\theta, \varphi)}{n_{\omega}^{\pm}(\theta, \varphi) \cdot n_{\omega}^{\pm}(\theta, \varphi) \cdot n_{2\omega}^{\pm}(\theta, \varphi)} \quad (4.11).$$

In order to avoid the difficulties associated with absolute measurements, we considered a normalized SH intensity defined as follows:

$$I_{2\omega}^N(\theta, \varphi) = \frac{I_{2\omega}(\theta, \varphi)}{I_{2\omega}(\theta, \varphi = 0^\circ / 10^\circ)} \approx \frac{\text{FOM}(\theta, \varphi)}{\text{FOM}(\theta, \varphi = 0^\circ / 10^\circ)} \quad (4.12).$$

It corresponds to the ratio between the SH intensities at different AQPM angles (θ, φ) and the SH intensity at the minimal value of φ corresponding to

the different types: $\varphi = 0^\circ$ for types II and V AQPM, and $\varphi = 10^\circ$ for types I and IV since the corresponding effective coefficients are zero in the principal planes as mentioned above. The calculated and measured normalized SH intensities are plotted in Fig. 4.14 as a function of the AQPM angle φ for the four AQPM types. The corresponding AQPM angles θ are given by the four curves of Fig. 4.1. Figure 4.14 confirms the very good agreement between theory and experimental results.

Note that there is an abnormal peak on the type II AQPM curve of Fig. 4.14(b) for φ ranging from 40° to 60° . That can be well explained by the crossing of this curve with that of type I BPM, as shown in Fig. 4.1. Actually, BPM can exist in a periodically-poled medium since birefringence exists.

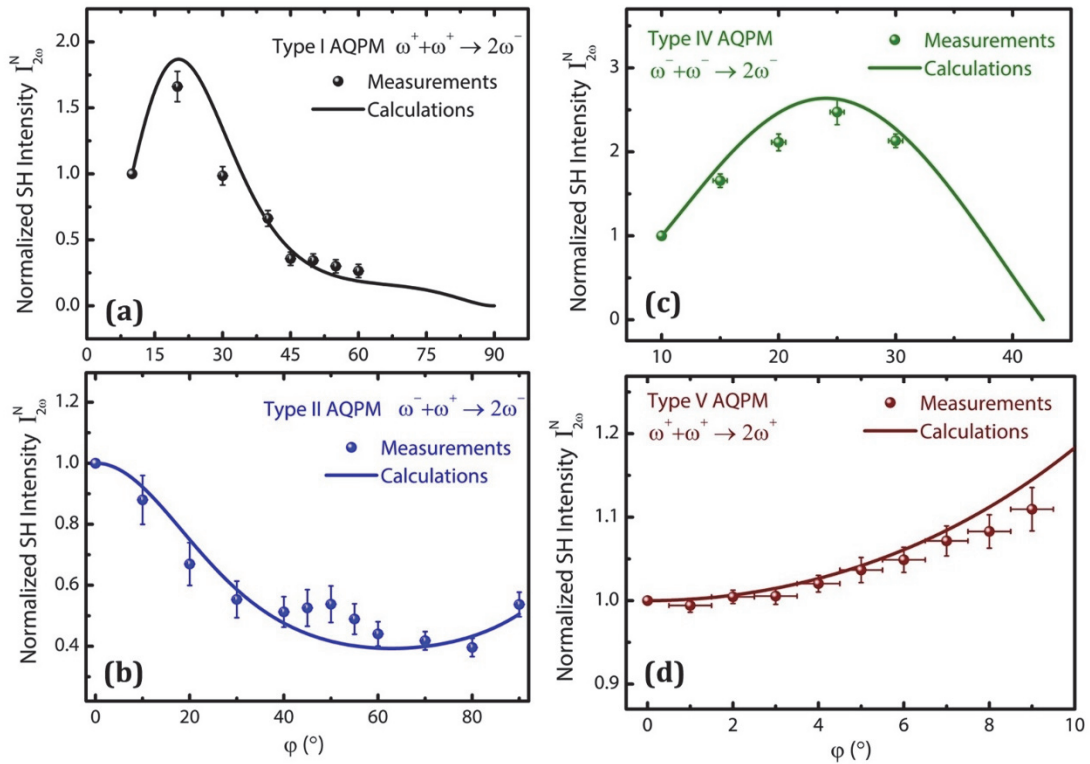


Figure 4.14 Normalized SH intensities as a function of types I, II, IV and V AQPM angles φ for a fundamental wavelength $\lambda_\omega = 2.15 \mu\text{m}$.

The coexistence of BPM and AQPM is then possible if the phase-matching directions are in coincidence, and if there are the required common polarization states, which is the case for type I BPM and type II AQPM in PPRKTP. One of the polarization states of the fundamental waves for generating type I BPM ($\omega^+ + \omega^+ \rightarrow 2\omega^+$) is the same as that of type II AQPM ($\omega^+ + \omega^- \rightarrow 2\omega^+$), *i.e.* the (+) mode, therefore, type I BPM is automatically excited during a type II AQPM experiment due to the common fundamental mode (+). Figure 4.1 also shows an intersection between the angular tuning curves of type IV AQPM ($\omega^- + \omega^- \rightarrow 2\omega^-$) and type II BPM ($\omega^- + \omega^+ \rightarrow 2\omega^-$) for φ ranging from 0° to 10° . But in that case, type II BPM cannot be excited during a type IV AQPM because the fundamental (+) mode is missing. Then type II BPM cannot influence the tuning curve of type IV AQPM, which can be verified in Fig. 4.14 (c).

4.5 Conclusions and perspectives

As a conclusion, we experimentally validated the theory of AQPM in the case of a biaxial crystal by performing SHG at a fundamental wavelength of $2.15 \mu\text{m}$ in a large-aperture PPRKTP shaped as a sphere. The angles of the four possible AQPM types were measured by the sphere method using a Kappa circle. Meanwhile, the measured SH generated intensities matched perfectly well with the calculations. The next step of this work will be the measurement of the AQPM angles as a function of wavelength followed by the fitting of these data, which should allow us to determine the proper Sellmeier equations of RKTTP. By this way, we can find out for example if there is some giant spectral acceptance situations in PPRKTP as in the case of PPLN [68].

5 Conclusion

This work was motivated by the investigation of the nonlinear crystal LGN suited for the generation using birefringence phase-matching (BPM) in the mid-infrared, and of the validation of the scheme of angular quasi-phase-matching (AQPM) in biaxial crystal, *i.e.* PPRKTP. These two crystals were shaped as polished spheres allowing any direction of propagation to be addressed. By this way it has been possible to fully and directly characterized the angular distribution of the BPM and AQPM properties of LGN and PPRKTP, respectively.

We grew large size $45 \times 45 \times 100 \text{ mm}^3$ of the new Langanite crystal $\text{La}_3\text{Ga}_{5.5}\text{Nb}_{0.5}\text{O}_{14}$ (LGN). The linear and quadratic optical properties have been studied in detail: we found that the transparency is ranging between $0.28 \mu\text{m}$ and $7.4 \mu\text{m}$, we determined accurate Sellmeier equations, and we found that the absolute magnitude of the nonlinear coefficient d_{ii} is equal to 3.0 pm/V , which is of the same order of magnitude of other oxides like KTP for example. Using our Sellmeier equations, we identified the possibility of generating a super continuum in the mid-Infrared by pumping LGN at the standard wavelength of emission of the Nd:YAG laser. From these results, LGN appears as a promising crystal for high energy generation. The immediate following of the optical experiments will be the generation of a super continuum from $1.5 \mu\text{m}$ to $3.5 \mu\text{m}$ using a pump beam at $1.064 \mu\text{m}$. This study gives also inspiration for the study and development of other nonlinear crystals belonging to the same chemical family, which will be done in the longer term.

We performed for the first time the experimental validation of the AQPM theory in the case of a biaxial crystal by performing SHG at a fundamental

wavelength of $2.15 \mu\text{m}$ in a large-aperture PPRKTP. This scheme is a generalization of QPM using a unidirectional grating where the pump beam is allowed to propagate in any direction with respect to the grating vector. The experimental demonstration of such a scheme had been completely achieved in the case of the uniaxial optical class in 2009. The well-known PPLN had been then considered for that purpose. Here we study the AQPM scheme in the case of the biaxial optical class by taking the example of PPRKTP. We measured the angular distribution of the loci as well of the conversion efficiency of the four possible SHG AQPM types allowed in PPRKTP. The experiments matched perfectly well with the calculations. The next direct step of this work will be the measurement of the SHG AQPM angles of types II and IV in the principle planes as a function of wavelength followed by the fitting of these data, which should allow us to determine the Sellmeier equations of PPRKTP that are unknown nowadays. We will also look for the directions for which the spectral acceptance is giant, as it exists in the case of PPLN. And finally the completion of the validation of the AQPM theory will require addressing the case of the third optical class, *i.e.* the isotropic one. OP-GaAs is the natural candidate for such a study, but its current thinness, no more than 1 mm, will not allow the shaping of a sphere, but of a cylinder.

6 References

- [1] N. Bloembergen, *Nonlinear optics*. World Scientific, 1996.
- [2] Y. Petit, B. Boulanger, P. Segonds, and T. Taira, "Angular quasi-phase-matching," *Physical Review A*, vol. 76, no. 6, p. 063817, 12/20 2007.
- [3] A. Yariv and P. Yeh, *Optical waves in crystals*. Wiley, New York, 1984.
- [4] B. Boulanger and J. Zyss, *International Table for Crystallography*. Kluwer Academic Publishers, 2006.
- [5] J. Q. Yao and T. S. Fahlen, "Calculations of optimum phase match parameters for the biaxial crystal KTiOPO_4 ," *Journal of Applied Physics*, vol. 55, no. 1, pp. 65-68, 1984.
- [6] J. F. Nye, *Physical properties of crystals: their representation by tensors and matrices*. Oxford university press, 1985.
- [7] A. J. Schell and N. Bloembergen, "Laser studies of internal conical diffraction. II. Intensity patterns in an optically active crystal, α -iodic acid*," *Journal of the Optical Society of America*, vol. 68, no. 8, pp. 1098-1106, 08/01 1978.
- [8] J. P. Fève, B. Boulanger, and G. Marnier, "Experimental study of internal and external conical refractions in KTP," *Optics Communications*, vol. 105, no. 3, pp. 243-252, 02/01/ 1994.
- [9] L. Shuvalov, *Physical Properties of Crystals*. Heidelberg: Springer Verlag, 1981.
- [10] P. Segonds, B. Boulanger, L. Ferrier, B. Ménaert, and J. Zaccaro, "Refractive indices determination of a small-size nonlinear biaxial crystal by use of double-refraction measurements with a laser beam," *Journal of the Optical Society of America B*, vol. 23, no. 5, pp. 852-856, 05/01 2006.
- [11] B. Boulanger and J.-P. Fève, "Méthodes de caractérisation des propriétés optiques non linéaires de conversion de fréquence des cristaux," *Collection de la Société Française d'Optique*, vol. 8, pp. 99-132, 2003.
- [12] J. A. Armstrong, N. Bloembergen, J. Ducuing, and P. S. Pershan, "Interactions

- between Light Waves in a Nonlinear Dielectric," *Physical Review*, vol. 127, no. 6, pp. 1918-1939, 09/15 1962.
- [13] B. Boulanger and G. Marnier, "Field factor calculation for the study of the relationships between all the three-wave nonlinear optical interactions in uniaxial and biaxial crystals," *Journal of Physics: Condensed Matter*, vol. 3, no. 43, p. 8327, 1991.
- [14] M. V. Hobden, "Phase - Matched Second - Harmonic Generation in Biaxial Crystals," *Journal of Applied Physics*, vol. 38, no. 11, pp. 4365-4372, 1967.
- [15] M. M. Fejer, G. A. Magel, D. H. Jundt, and R. L. Byer, "Quasi-phase-matched second harmonic generation: tuning and tolerances," *IEEE Journal of Quantum Electronics*, vol. 28, no. 11, pp. 2631-2654, 1992.
- [16] H. Karlsson and F. Laurell, "Electric field poling of flux grown KTiOPO₄," *Applied Physics Letters*, vol. 71, no. 24, pp. 3474-3476, 1997.
- [17] P. G. Schunemann, L. A. Pomeranz, Y. E. Young, L. Mohnkern, and A. Vera, "Recent advances in all-epitaxial growth and properties of orientation-patterned gallium arsenide (OP-GaAs)," in *Lasers and Electro-Optics, 2009 and 2009 Conference on Quantum electronics and Laser Science Conference. CLEO/QELS 2009. Conference on*, 2009, pp. 1-2: IEEE.
- [18] Shinji Koh, Takashi Kondo, Minoru Ebihara, Tetsuya Ishiwada, Hidetaka Sawada, Hideki Ichinose, Ichiro Shoji, and Ryoichi Ito, "GaAs/Ge/GaAs Sublattice Reversal Epitaxy on GaAs (100) and (111) Substrates for Nonlinear Optical Devices," *Japanese Journal of Applied Physics*, vol. 38, no. 5A, p. L508, 1999.
- [19] Y. Petit, "Nouvelles approhes en optique cristalline : distributions angulaires de l'absorption et de l'emission, auto-doublage, quasi-accord de phase angulaire," PhD, Universié Joseph Fourier, Grenoble, 2007.
- [20] J.-J. Zondy, "Comparative theory of walkoff-limited type-II versus type-I second harmonic generation with gaussian beams," *Optics Communications*, vol.

- 81, no. 6, pp. 427-440, 03/15/ 1991.
- [21] A. Godard, "Infrared (2-12 μm) solid-state laser sources: a review," *Comptes Rendus Physique*, vol. 8, no. 10, pp. 1100-1128, 12/01/ 2007.
- [22] W. R. H. A. Gebbie, C. Hilsum, A. W. Pryce, V. Roberts, "Atmospheric transmission in the 1 to 14 μm region," *Proceedings of the Royal Society of London. Series A. Mathematical and Physical Sciences*, vol. 206, no. 1084, pp. 87-107, 1951.
- [23] A. Schliesser, N. Picqué, and T. W. Hänsch, "Mid-infrared frequency combs," Review Article vol. 6, p. 440, 06/28/online 2012.
- [24] R. Soref, "Mid-infrared photonics in silicon and germanium," vol. 4, p. 495, 08/01/online 2010.
- [25] C. Chen, Y. Wu, A. Jiang, B. Wu, G. You, R. Li, and S. Lin, "New nonlinear-optical crystal: LiB_3O_5 ," *Journal of the Optical Society of America B*, vol. 6, no. 4, pp. 616-621, 04/01 1989.
- [26] T. Sasaki, Y. Mori, I. Kuroda, S. Nakajima, K. Yamaguchi, S. Watanabe, and S. Nakai, "Caesium Lithium Borate: a New Nonlinear Optical Crystal," *Acta Crystallographica Section C*, vol. 51, no. 11, pp. 2222-2224, 1995.
- [27] V. Petrov, "Progress in 1- μm Pumped Mid-IR Optical Parametric Oscillators Based on Non-Oxide Nonlinear Crystals," *IEEE Journal of Selected Topics in Quantum Electronics*, vol. 21, no. 1, pp. 193-206, 2015.
- [28] L. Arizmendi, "Photonic applications of lithium niobate crystals," *physica status solidi (a)*, vol. 201, no. 2, pp. 253-283, 2004.
- [29] D. von der Linde, O. F. Schirmer, and H. Kurz, "Intrinsic photorefractive effect of LiNbO_3 ," *Applied physics*, journal article vol. 15, no. 2, pp. 153-156, 02/01 1978.
- [30] Y. Yang, Y. Zhang, Q. Gu, H. Zhang, and X. Tao, "Growth and annealing characterization of ZnGeP_2 crystal," *Journal of Crystal Growth*, vol. 318, no. 1, pp. 721-724, 03/01/ 2011.
- [31] K. L. Vodopyanov, F. Ganikhanov, J. P. Maffetone, I. Zwieback, and W. Ruderman, " ZnGeP_2 optical parametric oscillator with 3.8-12.4- μm tunability,"

- Optics Letters*, vol. 25, no. 11, pp. 841-843, 06/01 2000.
- [32] J. Stade, L. Bohatý, M. Hengst, and R. B. Heimann, "Electro-optic, Piezoelectric and Dielectric Properties of Langasite ($\text{La}_3\text{Ga}_5\text{SiO}_{14}$), Langanite ($\text{La}_3\text{Ga}_{5.5}\text{Nb}_{0.5}\text{O}_{14}$) and Langataite ($\text{La}_3\text{Ga}_{5.5}\text{Tao}_{.5}\text{O}_{14}$)," *Crystal Research and Technology*, vol. 37, no. 10, pp. 1113-1120, 2002.
- [33] E. Boursier, P. Segonds, B. Boulanger, C. Félix, J. Debray, D. Jegouso, B. Ménaert, D. Roshchupkin, and I. Shoji, "Phase-matching directions, refined Sellmeier equations, and second-order nonlinear coefficient of the infrared Langatate crystal $\text{La}_3\text{Ga}_{5.5}\text{Tao}_{.5}\text{O}_{14}$," *Optics Letters*, vol. 39, no. 13, pp. 4033-4036, 07/01 2014.
- [34] H. Kong, J. Wang, H. Zhang, and X. Yin, "Growth and characterization of $\text{La}_3\text{Ga}_{5.5}\text{Nb}_{0.5}\text{O}_{14}$ crystal," *Journal of Crystal Growth*, vol. 292, no. 2, pp. 408-411, 07/01/ 2006.
- [35] M. P. Da Cunha and S. D. A. Fagundes, "Investigation on recent quartz-like materials for SAW applications," *IEEE transactions on ultrasonics, ferroelectrics, and frequency control*, vol. 46, no. 6, pp. 1583-1590, 1999.
- [36] J. Bohm, R. B. Heimann, M. Hengst, R. Roewer, and J. Schindler, "Czochralski growth and characterization of piezoelectric single crystals with langasite structure: $\text{La}_3\text{Ga}_5\text{SiO}_{14}$ (LGS), $\text{La}_3\text{Ga}_{5.5}\text{Nb}_{0.5}\text{O}_{14}$ (LGN), and $\text{La}_3\text{Ga}_{5.5}\text{Tao}_{.5}\text{O}_{14}$ (LGT): Part I," *Journal of Crystal Growth*, vol. 204, no. 1, pp. 128-136, 07/01/ 1999.
- [37] J. Bohm, E. Chilla, C. Flannery, H. J. Fröhlich, T. Hauke, R. B. Heimann, M. Hengst, and U. Straube, "Czochralski growth and characterization of piezoelectric single crystals with langasite structure: $\text{La}_3\text{Ga}_5\text{SiO}_{14}$ (LGS), $\text{La}_3\text{Ga}_{5.5}\text{Nb}_{0.5}\text{O}_{14}$ (LGN) and $\text{La}_3\text{Ga}_{5.5}\text{Tao}_{.5}\text{O}_{14}$ (LGT) II. Piezoelectric and elastic properties," *Journal of Crystal Growth*, vol. 216, no. 1, pp. 293-298, 06/15/ 2000.
- [38] A. Pavlovska, S. Werner, B. Maximov, and B. Mill, "Pressure-induced phase

- transitions of piezoelectric single crystals from the langasite family: $\text{La}_3\text{Nb}_{0.5}\text{Ga}_{5.5}\text{O}_{14}$ and $\text{La}_3\text{Tao}_{0.5}\text{Ga}_{5.5}\text{O}_{14}$," *Acta Crystallographica Section B*, vol. 58, no. 6, pp. 939-947, 2002.
- [39] T. F. Veremeichik, "Optical activity and crystalline structure of crystals of the langasite family," *Crystallography Reports*, journal article vol. 56, no. 6, pp. 1060-1065, 11/01 2011.
- [40] G. M. Kuz'micheva, E. A. Tyunina, E. N. Domoroshchina, V. B. Rybakov, and A. B. Dubovskii, "X-ray diffraction study of $\text{La}_3\text{Ga}_{5.5}\text{Tao}_{0.5}\text{O}_{14}$ and $\text{La}_3\text{Ga}_{5.5}\text{Nb}_{0.5}\text{O}_{14}$ langasite-type single crystals," *Inorganic Materials*, journal article vol. 41, no. 4, pp. 412-419, 04/01 2005.
- [41] R. H. French, J. W. Ling, F. S. Ohuchi, and C. T. Chen, "Electronic structure of $\beta\text{-BaB}_2\text{O}_4$ and LiB_3O_5 nonlinear optical crystals," *Physical Review B*, vol. 44, no. 16, pp. 8496-8502, 10/15/ 1991.
- [42] C. Chen, Y. Wu, and R. Li, "The anionic group theory of the non-linear optical effect and its applications in the development of new high-quality NLO crystals in the borate series," *International Reviews in Physical Chemistry*, vol. 8, no. 1, pp. 65-91, 01/01 1989.
- [43] K. Nassau, "Dr. A. V. L. Verneuil: The man and the method," *Journal of Crystal Growth*, vol. 13-14, no. Supplement C, pp. 12-18, 05/01/ 1972.
- [44] J. Czochralski, "Ein neues Verfahren zur Messung der Kristallisationsgeschwindigkeit der Metalle," in *Zeitschrift für Physikalische Chemie* vol. 92U, ed, 1918, p. 219.
- [45] H. v. Wartenberg, "Elastische Nachwirkung in Metallen," *Deut. phys. Gesell*, vol. 20, p. 113, 1918.
- [46] G. K. Teal and J. Little, "Growth of germanium single crystals," in *Physical review*, 1950, vol. 78, no. 5, pp. 647-647: AMERICAN PHYSICAL SOC ONE PHYSICS ELLIPSE, COLLEGE PK, MD 20740-3844 USA.
- [47] H. E. Buckley, *Crystal growth*. John Wiley and Sons, 1952.

- [48] InfraCrystal, "Infracrystal. Setting the growth of germanium crystals.," ed. <http://infracrystal.ru/hist>.
- [49] J. Wang, G. Zhang, H. Yu, Y. Wang, and C. Chen, "5 - Czochralski and Flux Growth of Crystals for Lasers and Nonlinear Optics A2 - Rudolph, Peter," in *Handbook of Crystal Growth (Second Edition)* Boston: Elsevier, 2015, pp. 169-208.
- [50] Z. Pan, "Development of the Key Borate Crystals for OPCPA Technique," Doctor, Institute of Crystal Materials, Shandong University, 2013.
- [51] Y. Terada, K. Shimamura, and T. Fukuda, "Growth and optical properties of RE doped bulk and fiber single crystals by Czochralski and micro pulling down methods," *Journal of Alloys and Compounds*, vol. 275-277, no. Supplement C, pp. 697-701, 07/24/ 1998.
- [52] K. Chow and H. G. McKnight, "The growth and characterization of pure and rare-earth-substituted YVO₄," *Materials Research Bulletin*, vol. 8, no. 12, pp. 1343-1350, 12/01/ 1973.
- [53] H. Kong, J. Wang, H. Zhang, X. Yin, S. Zhang, Y. Liu, X. Cheng, L. Gao, X. Hu, and M. Jiang, "Growth, properties and application as an electrooptic Q-switch of langasite crystal," *Journal of Crystal Growth*, vol. 254, no. 3, pp. 360-367, 07/01/ 2003.
- [54] Y. Yu, "Numerical Simulation, Growth and Properties Investigation of Several Oxide Crystals " Doctor, Institute of Crystal Materials, Shandong University, 2009.
- [55] A. G. Ostrogorsky and G. Müller, "A model of effective segregation coefficient, accounting for convection in the solute layer at the growth interface," *Journal of Crystal Growth*, vol. 121, no. 4, pp. 587-598, 08/01/ 1992.
- [56] M. Kitaura, K. Mochizuki, Y. Inabe, M. Itoh, H. Nakagawa, and S. Oishi, "Fundamental optical properties and electronic structure of langasite La₃Ga₅SiO₁₄ crystals," *Physical Review B*, vol. 69, no. 11, p. 115120, 03/26/ 2004.
- [57] G. Marnier and B. Boulanger, "The sphere method: A new technique in linear

- and non-linear crystalline optical studies," *Optics Communications*, vol. 72, no. 3, pp. 139-143, 07/15 1989.
- [58] B. Ménaert, J. Debray, J. Zaccaro, P. Segonds, and B. Boulanger, "Bulk cylinders and spheres: from shaping to the use for linear and nonlinear optics," *Optical Materials Express*, vol. 7, no. 8, pp. 3017-3022, 08/01 2017.
- [59] B. Boulanger, J. P. Fève, G. Marnier, C. Bonnin, P. Villeval, and J. J. Zondy, "Absolute measurement of quadratic nonlinearities from phase-matched second-harmonic generation in a single KTP crystal cut as a sphere," *Journal of the Optical Society of America B*, vol. 14, no. 6, pp. 1380-1386, 06/01 1997.
- [60] Y. Guillien, B. Ménaert, J. P. Fève, P. Segonds, J. Douady, B. Boulanger, and O. Pacaud, "Crystal growth and refined Sellmeier equations over the complete transparency range of RbTiOPO_4 ," *Optical Materials*, vol. 22, no. 2, pp. 155-162, 04/01 2003.
- [61] J.-P. Fève, B. t. Boulanger, O. Pacaud, I. Rousseau, B. Ménaert, G. Marnier, P. Villeval, C. Bonnin, G. M. Loiacono, and D. N. Loiacono, "Phase-matching measurements and Sellmeier equations over the complete transparency range of KTiOAsO_4 , RbTiOAsO_4 , and CsTiOAsO_4 ," *Journal of the Optical Society of America B*, vol. 17, no. 5, pp. 775-780, 05/01 2000.
- [62] V. Kemlin, P. Brand, B. Boulanger, P. Segonds, P. G. Schunemann, K. T. Zawilski, B. Ménaert, and J. Debray, "Phase-matching properties and refined Sellmeier equations of the new nonlinear infrared crystal CdSiP_2 ," *Optics Letters*, vol. 36, no. 10, pp. 1800-1802, 05/15 2011.
- [63] P. Segonds, B. Boulanger, J.-P. Fève, B. Ménaert, J. Zaccaro, G. Aka, and D. Pelenc, "Linear and nonlinear optical properties of the monoclinic $\text{Ca}_4\text{YO}(\text{BO}_3)_3$ crystal," *Journal of the Optical Society of America B*, vol. 21, no. 4, pp. 765-769, 04/01 2004.
- [64] F. Guo, P. Segonds, B. Ménaert, J. Debray, G. Aka, P. Loiseau, and B. Boulanger, "Dielectric frame, Sellmeier equations, and phase-matching

- properties of the monoclinic acentric crystal $\text{GdCa}_4\text{O}(\text{BO}_3)_3$," *Optics Letters*, vol. 41, no. 22, pp. 5290-5293, 11/15 2016.
- [65] E. Boursier, P. Segonds, B. Ménaert, V. Badikov, V. Panyutin, D. Badikov, V. Petrov, and B. Boulanger, "Phase-matching directions and refined Sellmeier equations of the monoclinic acentric crystal BaGa_4Se_7 ," *Optics Letters*, vol. 41, no. 12, pp. 2731-2734, 06/15 2016.
- [66] P. Brand, B. Boulanger, P. Segonds, Y. Petit, C. Félix, B. Ménaert, T. Taira, and H. Ishizuki, "Angular quasi-phase-matching experiments and determination of accurate Sellmeier equations for 5%MgO:PPLN," *Optics Letters*, vol. 34, no. 17, pp. 2578-2580, 09/01 2009.
- [67] B. Boulanger, J. P. Feve, G. Marnier, G. M. Loiacono, D. N. Loiacono, and C. Bonnin, "SHG and internal conical refraction experiments in CsTiOAsO_4 , comparison with KTiOPO_4 and KTiOAsO_4 , for $1.32 \mu\text{m}$ type II SHG," *IEEE Journal of Quantum Electronics*, vol. 33, no. 6, pp. 945-949, 1997.
- [68] P. Brand, "Study of 5%MgO:PPLN and CdSiP_2 for infrared parametric generation," PhD, L'ECOLE DOCTORALE EEATS, Université de Grenoble, 2010.
- [69] A. E. Siegman, *Lasers*. University Science Books, 1986.
- [70] F. Guo, D. Lu, P. Segonds, J. Debray, T. Xu, H. Yu, Q. Fu, H. Zhang, J. Wang, and B. Boulanger, "Quadratic nonlinear optical properties of the new crystal $\text{La}_3\text{Ga}_{5.5}\text{Nb}_{0.5}\text{O}_{14}$," *Optical Materials Express*, Vol. 8, no. 4, pp. 858-864, 09/03 2018.
- [71] D. Lu, T. Xu, H. Yu, Q. Fu, H. Zhang, P. Segonds, B. Boulanger, X. Zhang, and J. Wang, "Acentric langanite $\text{La}_3\text{Ga}_{5.5}\text{Nb}_{0.5}\text{O}_{14}$ crystal: a new nonlinear crystal for the generation of mid-infrared parametric light," *Optics Express*, vol. 24, no. 16, pp. 17603-17615, 08/08 2016.
- [72] J. Jerphagnon and S. K. Kurtz, "Maker Fringes: A Detailed Comparison of Theory and Experiment for Isotropic and Uniaxial Crystals," *Journal of Applied*

- Physics*, vol. 41, no. 4, pp. 1667-1681, 1970.
- [73] X. Zhang, X. a. Wang, G. Wang, Y. Wu, Y. Zhu, and C. Chen, "Determination of the nonlinear optical coefficients of the $\text{Li}_x\text{Cs}_{(1-x)}\text{B}_3\text{O}_5$ crystals," *Journal of the Optical Society of America B*, vol. 24, no. 11, pp. 2877-2882, 11/01 2007.
- [74] D. Eimerl, "Electro-optic, linear, and nonlinear optical properties of KDP and its isomorphs," *Ferroelectrics*, vol. 72, no. 1, pp. 95-139, 03/01 1987.
- [75] R. C. Miller, "Optical second harmonic generation in piezoelectric crystals," *Applied Physics Letters*, vol. 5, no. 1, pp. 17-19, 1964.
- [76] V. Petrov, M. Ghotbi, O. Kokabee, A. Esteban-Martin, F. Noack, A. Gaydardzhiev, I. Nikolov, P. Tzankov, I. Buchvarov, K. Miyata, A. Majchrowski, I. V. Kityk, F. Rotermund, E. Michalski, and M. Ebrahim-Zadeh, "Femtosecond nonlinear frequency conversion based on BiB_3O_6 ," *Laser & Photonics Reviews*, vol. 4, no. 1, pp. 53-98, 2010.
- [77] V. Kemlin, "Parametric infrared generation : from crystals to devices," PhD, L'ECOLE DOCTORALE EEATS, Université Grenoble Alpes, 2013.
- [78] J. Wang, H. Yu, Y. Wu, and R. Boughton, "Recent Developments in Functional Crystals in China," *Engineering*, vol. 1, no. 2, pp. 192-210, 06/01/ 2015.
- [79] V. G. Dmitriev, G. G. Gurzadyan, and D. N. Nikogosyan, *Handbook of Nonlinear Optical Crystals*. Springer Berlin Heidelberg, 2013.
- [80] M. M. Choy and R. L. Byer, "Accurate second-order susceptibility measurements of visible and infrared nonlinear crystals," *Physical Review B*, vol. 14, no. 4, pp. 1693-1706, 08/15/ 1976.
- [81] R. L. Byer, Y. K. Park, R. S. Feigelson, and W. L. Kway, "Efficient second-harmonic generation of Nd:YAG laser radiation using warm phasematching LiNbO_3 ," *Applied Physics Letters*, vol. 39, no. 1, pp. 17-19, 1981.
- [82] A. Boucon, B. Hardy-Baranski, and F. Bretenaker, "Compact infrared continuous-wave double-pass single-frequency doubly-resonant OPO," *Optics*

- Communications*, vol. 333, pp. 53-57, 12/15/ 2014.
- [83] B. Hardy, A. Berrou, S. Guilbaud, M. Raybaut, A. Godard, and M. Lefebvre, "Compact, single-frequency, doubly resonant optical parametric oscillator pumped in an achromatic phase-adapted double-pass geometry," *Optics Letters*, vol. 36, no. 5, pp. 678-680, 03/01 2011.
- [84] F. C. Zumsteg, J. D. Bierlein, and T. E. Gier, "K_xRb_{1-x}TiOPO₄: A new nonlinear optical material," *Journal of Applied Physics*, vol. 47, no. 11, pp. 4980-4985, 1976.
- [85] Y. F. Chen, Y. S. Chen, and S. W. Tsai, "Diode-pumped Q-switched laser with intracavity sum frequency mixing in periodically poled KTP," *Applied Physics B*, journal article vol. 79, no. 2, pp. 207-210, 07/01 2004.
- [86] S. Lin, Z. Sun, B. Wu, and C. Chen, "The nonlinear optical characteristics of a LiB₃O₅ crystal," *Journal of Applied Physics*, vol. 67, no. 2, pp. 634-638, 1990.
- [87] F. Kienle, P. S. Teh, D. Lin, S.-u. Alam, J. H. V. Price, D. C. Hanna, D. J. Richardson, and D. P. Shepherd, "High-power, high repetition-rate, green-pumped, picosecond LBO optical parametric oscillator," *Optics Express*, vol. 20, no. 7, pp. 7008-7014, 03/26 2012.
- [88] W. Quan Zhang, "Optical parametric generation for biaxial crystal," *Optics Communications*, vol. 105, no. 3, pp. 226-232, 02/01/ 1994.
- [89] L. K. Cheng and J. D. Bierlein, "KTP and isomorphs - recent progress in device and material development," *Ferroelectrics*, vol. 142, no. 1, pp. 209-228, 01/01 1993.
- [90] J. D. Bierlein, H. Vanherzeele, and A. A. Ballman, "Linear and nonlinear optical properties of flux-grown KTiOAsO₄," *Applied Physics Letters*, vol. 54, no. 9, pp. 783-785, 1989.
- [91] R. J. Bolt and M. van der Mooren, "Single shot bulk damage threshold and conversion efficiency measurements on flux grown KTiOPO₄ (KTP)," *Optics Communications*, vol. 100, no. 1, pp. 399-410, 07/01/ 1993.

- [92] F. Guo, D. Lu, P. Segonds, J. Debray, H. Yu, H. Zhang, J. Wang, and B. Boulanger, "Phase-matching properties and refined Sellmeier equations of $\text{La}_3\text{Ga}_{5.5}\text{Nb}_{0.5}\text{O}_{14}$," *Optical Materials Express*, vol. 8, no. 4, pp. 858-864, 04/01 2018.
- [93] Q. Fu, G. Mak, and H. M. van Driel, "High-power, 62-fs infrared optical parametric oscillator synchronously pumped by a 76-MHz Ti:sapphire laser," *Optics Letters*, vol. 17, no. 14, pp. 1006-1008, 07/15 1992.
- [94] E. Boursier, G. M. Archipovaite, J.-C. Delagnes, S. Petit, G. Ernotte, P. Lassonde, P. Segonds, B. Boulanger, Y. Petit, F. Légaré, D. Roshchupkin, and E. Cormier, "Study of middle infrared difference frequency generation using a femtosecond laser source in LGT," *Optics Letters*, vol. 42, no. 18, pp. 3698-3701, 09/15 2017.
- [95] V. Petrov, "Parametric down-conversion devices: The coverage of the mid-infrared spectral range by solid-state laser sources," *Optical Materials*, vol. 34, no. 3, pp. 536-554, 01/01/ 2012.
- [96] J. P. Fève, B. Boulanger, and G. Marnier, "Calculation and classification of the direction loci for collinear types I, II and III phase-matching of three-wave nonlinear optical parametric interactions in uniaxial and biaxial acentric crystals," *Optics Communications*, vol. 99, no. 3, pp. 284-302, 06/01/ 1993.
- [97] V. Berger, "Nonlinear Photonic Crystals," *Physical Review Letters*, vol. 81, no. 19, pp. 4136-4139, 11/09/ 1998.
- [98] R. Remez, N. Shapira, C. Roques-Carmes, R. Tirole, Y. Yang, Y. Lereah, M. Soljačić, I. Kaminer, and A. Arie, "Spectral and spatial shaping of Smith-Purcell radiation," *Physical Review A*, vol. 96, no. 6, p. 061801, 12/06/ 2017.
- [99] H. Ishizuki and T. Taira, "High-energy quasi-phase-matched optical parametric oscillation in a periodically poled $\text{MgO}:\text{LiNbO}_3$ device with a $5\text{mm}\times 5\text{mm}$ aperture," *Optics Letters*, vol. 30, no. 21, pp. 2918-2920, 11/01 2005.
- [100] H. Ishizuki and T. Taira, "High energy quasi-phase matched optical

- parametric oscillation using Mg-doped congruent LiTaO₃ crystal," *Optics Express*, vol. 18, no. 1, pp. 253-258, 01/04 2010.
- [101] J. Hellström, V. Pasiskevicius, H. Karlsson, and F. Laurell, "High-power optical parametric oscillation in large-aperture periodically poled KTiOPO₄," *Optics Letters*, vol. 25, no. 3, pp. 174-176, 02/01 2000.
- [102] A. Zukauskas, N. Thilmann, V. Pasiskevicius, F. Laurell, and C. Canalias, "5 mm thick periodically poled Rb-doped KTP for high energy optical parametric frequency conversion," *Optical Materials Express*, vol. 1, no. 2, pp. 201-206, 06/01 2011.
- [103] T. Kubota, H. Atarashi, and I. Shoji, "Fabrication of quasi-phase-matching stacks of GaAs plates using a new technique: room-temperature bonding," *Optical Materials Express*, vol. 7, no. 3, pp. 932-938, 03/01 2017.
- [104] F. Masiello, T. A. Lafford, P. Pernot, J. Baruchel, D. S. Keeble, P. A. Thomas, A. Zukauskas, G. Stromqvist, F. Laurell, and C. Canalias, "Investigation by coherent X-ray section topography of ferroelectric domain behaviour as a function of temperature in periodically poled Rb:KTP," *Journal of Applied Crystallography*, vol. 44, no. 3, pp. 462-466, 2011.
- [105] K. Kato and E. Takaoka, "Sellmeier and thermo-optic dispersion formulas for KTP," *Applied Optics*, vol. 41, no. 24, pp. 5040-5044, 08/20 2002.
- [106] B. Boulanger, J. P. Fève, G. Marnier, B. Ménaert, X. Cabirol, P. Villeval, and C. Bonnin, "Relative sign and absolute magnitude of d(2) nonlinear coefficients of KTP from second-harmonic-generation measurements," *Journal of the Optical Society of America B*, vol. 11, no. 5, pp. 750-757, 05/01 1994.

7 Appendix

- D. Lu, T. Xu, H. Yu, Q. Fu, H. Zhang, P. Segonds, B. Boulanger, X. Zhang, and J. Wang, “Acentric langanite $La_3Ga_{5.5}Nb_{0.5}O_{14}$ crystal: a new nonlinear crystal for the generation of mid-infrared parametric light” *Optics Express* 24 (16), 17603 (2016);
- F. Guo, D. Lu, P. Segonds, J. Debray, H. Yu, H. Zhang, J. Wang, and B. Boulanger, “Phase-matching properties and refined Sellmeier equations of $La_3Ga_{5.5}Nb_{0.5}O_{14}$ ” *Optical Materials Express* 8(4), 858 (2018);
- D. Lu, A. Peña, P. Segonds, J. Debray, S. Joly, F. Laurell, V. Pasiskevicius, H. Yu, H. Zhang, J. Wang, C. Canalias and B. Boulanger, “Validation of the Angular Quasi-Phase-Matching theory for the biaxial optical class using PPRKTP”, *Optics Letters*, accepted (2018).

Acentric langanite $\text{La}_3\text{Ga}_{5.5}\text{Nb}_{0.5}\text{O}_{14}$ crystal: a new nonlinear crystal for the generation of mid-infrared parametric light

DAZHI LU,¹ TIANXIANG XU,¹ HAOHAI YU,^{1,4} QIANG FU,² HUIJIN ZHANG,^{1,5} PATRICIA SEGONDS,³ BENOIT BOULANGER,^{3,6} XINGYU ZHANG,² AND JIYANG WANG¹

¹State Key Laboratory of Crystal Materials and Institute of Crystal Materials, Shandong University, Jinan 250100, China

²School of Information Science and Engineering, Shandong University, Jinan, 250100, China

³Institut Néel Centre National de la Recherche Scientifique — Université Joseph Fourier BP 166, F38402 Grenoble Cedex 9, France

⁴haohaiyu@sdu.edu.cn

⁵huaijinzhang@sdu.edu.cn

⁶benoit.boulanger@neel.cnrs.fr

Abstract: The mid-infrared spectral range extending from 2 to 6 μm is significant for scientific and technological applications. A promising nonlinear oxide crystal $\text{La}_3\text{Ga}_{5.5}\text{Nb}_{0.5}\text{O}_{14}$ (LGN) is proposed and fully characterized for the first time to our knowledge. The transparency range extends between 0.28 and 7.4 μm . The two principal refractive indices were measured and we found that the nonlinear coefficient $d_{11} = 3.0 \pm 0.1$ pm/V at 0.532 μm . The simultaneous fit of data allowed us to refine the Sellmeier equations of LGN and to calculate the tuning curves for optical parametric generation (OPG) pumped at 1.064 μm . Calculations are consistent with recorded data and also show the generation of a supercontinuum between 1.5 and 3.5 μm when pumped at 0.98 μm by a Ti:Sapphire laser.

©2016 Optical Society of America

OCIS codes: (190.0190) Nonlinear optics; (190.4400) Nonlinear optics, materials; (190.4223) Nonlinear wave mixing; (190.4975) Parametric processes.

References and links

1. A. Godard, "Infrared (2–12 μm) solid-state laser sources: a review," *C. R. Phys.* **8**(10), 1100–1128 (2007).
2. H. A. Gebbie, W. R. Harding, C. Hilsum, A. W. Pryce, and V. Roberts, "Atmospheric Transmission in the 1 to 14 μm Region," *P. Roy. Soc. A: Math. Phys.* **206**(1084), 87–107 (1951).
3. A. Schliesser, N. Picque, and T. W. Hansch, "Mid-infrared frequency combs," *Nat. Photonics* **6**(7), 440–449 (2012).
4. R. Soref, "Mid-infrared photonics in silicon and germanium," *Nat. Photonics* **4**(8), 495–497 (2010).
5. S. Cussat-Blanc, A. Ivanov, D. Lupinski, and E. Freysz, "KTiOPO₄, KTiOAsO₄, and KNbO₃ crystals for mid-infrared femtosecond optical parametric amplifiers: analysis and comparison," *Appl. Phys. B* **70**(1), 247–252 (2000).
6. K. Fradkin, A. Arie, A. Skliar, and G. Rosenman, "Tunable midinfrared source by difference frequency generation in bulk periodically poled KTiOPO₄," *Appl. Phys. Lett.* **74**(7), 914–916 (1999).
7. J. P. Fève, B. Boulanger, B. Ménaert, and O. Pacaud, "Continuous tuning of a microlaser-pumped optical parametric generator by use of a cylindrical periodically poled lithium niobate crystal," *Opt. Lett.* **28**(12), 1028–1030 (2003).
8. S. C. Kumar, M. Jelinek, M. Baudisch, K. T. Zawilski, P. G. Schunemann, V. Kubeček, J. Biegert, and M. Ebrahim-Zadeh, "Tunable, high-energy, mid-infrared, picosecond optical parametric generator based on CdSiP₂," *Opt. Express* **20**(14), 15703–15709 (2012).
9. S. Wang, M. Zhan, G. Wang, H. Xuan, W. Zhang, C. Liu, C. Xu, Y. Liu, Z. Wei, and X. Chen, "4H-SiC: a new nonlinear material for midinfrared lasers," *Laser Photonics Rev.* **7**(6), 1–8 (2013).
10. E. Boursier, P. Segonds, B. Boulanger, C. Félix, J. Debray, D. Jegouso, B. Ménaert, D. Roshchupkin, and I. Shoji, "Phase-matching directions, refined Sellmeier equations, and second-order nonlinear coefficient of the infrared Langatate crystal $\text{La}_3\text{Ga}_{5.5}\text{Ta}_{0.5}\text{O}_{14}$," *Opt. Lett.* **39**(13), 4033–4036 (2014).
11. H. Kong, J. Wang, H. Zhang, X. Yin, X. Cheng, Y. Lin, X. Hu, X. Xu, and M. Jiang, "Growth and characterization of $\text{La}_3\text{Ga}_{5.5}\text{Ta}_{0.5}\text{O}_{14}$ crystal," *Cryst. Res. Technol.* **39**(8), 686–691 (2004).
12. J. Stade, L. Bohatý, M. Hengst, and R. B. Heimann, "Electro-optic, Piezoelectric and Dielectric Properties of Langasite ($\text{La}_3\text{Ga}_5\text{SiO}_{14}$), Langanite ($\text{La}_3\text{Ga}_{5.5}\text{Nb}_{0.5}\text{O}_{14}$) and Langataite ($\text{La}_3\text{Ga}_{5.5}\text{Ta}_{0.5}\text{O}_{14}$)," *Cryst. Res. Technol.* **37**(10), 1113–1120 (2002).

13. B. Boulanger and J. Zyss, *International Tables for Crystallography* (Academic Publisher, 2006).
14. J. Jerphagnon and S. Kurtz, "Maker fringes: a detailed comparison of theory and experiment for isotropic and uniaxial crystals," *J. Appl. Phys.* **41**(4), 1667–1681 (1970).
15. X. Zhang, X. Wang, G. Wang, Y. Wu, Y. Zhu, and C. Chen, "Determination of the nonlinear optical coefficients of the $\text{Li}_x\text{Cs}_{(1-x)}\text{B}_3\text{O}_5$ crystals," *J. Opt. Soc. Am. B* **24**(11), 2877–2882 (2007).
16. "Lasers and laser-related equipment-determination of laser-induced damage threshold of optical surface-part 1: 1-on-1 test" ISO Report No. 11254–1-2000.
17. A. Pavlovska, S. Werner, B. Maximov, and B. Mill, "Pressure-induced phase transitions of piezoelectric single crystals from the langasite family: $\text{La}_3\text{Nb}_{0.5}\text{Ga}_{5.5}\text{O}_{14}$ and $\text{La}_3\text{Ta}_{0.5}\text{Ga}_{5.5}\text{O}_{14}$," *Acta Crystallogr. B* **58**(Pt 6), 939–947 (2002).
18. R. H. French, J. W. Ling, F. S. Ohuchi, and C. T. Chen, "Electronic structure of β - BaB_2O_4 and LiB_3O_5 nonlinear optical crystals," *Phys. Rev. B Condens. Matter* **44**(16), 8496–8502 (1991).
19. T. Veremeichik, "Optical Activity and Crystalline Structure of Crystals of the Langasite Family," *Crystallogr. Rep.* **56**(6), 1129–1134 (2011).
20. G. Kuz'micheva, E. Tyunina, E. Domoroshchina, V. Rybakov, and A. Dubovskii, "X-ray Diffraction Study of $\text{La}_3\text{Ga}_{5.5}\text{Ta}_{0.5}\text{O}_{14}$ and $\text{La}_3\text{Ga}_{5.5}\text{Nb}_{0.5}\text{O}_{14}$ Langasite-Type Single Crystals," *Inorg. Mater.* **41**(4), 485–492 (2005).
21. C. Chen, Y. Wu, and R. Li, "The anionic group theory of the non-linear optical effect and its applications in the development of new high-quality NLO crystals in the borate series," *Int. Rev. Phys. Chem.* **8**(1), 65–91 (1989).
22. C. Chen, A. Jiang, B. Wu, G. You, R. Li, and S. Lin, "New nonlinear-optical crystal: LiB_3O_5 ," *J. Opt. Soc. Am. B* **6**(4), 616–621 (1989).
23. D. N. Nikogosyan, "Beta barium borate (BBO)," *Appl. Phys., A Mater. Sci. Process.* **52**(6), 359–368 (1991).
24. H. Ishizuki and T. Taira, "Mg-doped congruent LiTaO_3 crystal for large-aperture quasi-phase matching device," *Opt. Express* **16**(21), 16963–16970 (2008).
25. V. G. Dmitriev, G. G. Gurzadyan, and D. N. Nikogosyan, *Handbook of Nonlinear Optical Crystals* (Springer, 2013).
26. M. Kitaura, K. Mochizuki, Y. Inabe, M. Itoh, H. Nakagawa, and S. Oishi, "Fundamental optical properties and electronic structure of langasite $\text{La}_3\text{Ga}_5\text{SiO}_{14}$ crystals," *Phys. Rev. B* **69**(11), 115120 (2004).
27. J. E. Jaffe and A. Zunger, "Theory of the band-gap anomaly in ABC_2 chalcopyrite semiconductors," *Phys. Rev. B* **29**(4), 1882–1906 (1984).
28. J. Yao, D. Mei, L. Bai, Z. Lin, W. Yin, P. Fu, and Y. Wu, " BaGa_4Se_7 : a new congruent-melting IR nonlinear optical material," *Inorg. Chem.* **49**(20), 9212–9216 (2010).
29. G. D. Boyd, E. Buehler, and F. G. Storz, "Linear and nonlinear optical properties of ZnGeP_2 and CdSe ," *Appl. Phys. Lett.* **18**(7), 301–304 (1971).
30. J. Tauc, R. Grigorovici, and A. Vancu, "Optical Properties and Electronic Structure of Amorphous Germanium," *Phys. Status Solidi* **15**(2), 627–637 (1966).
31. H. Kong, J. Wang, H. Zhang, and X. Yin, "Growth and characterization of $\text{La}_3\text{Ga}_{5.5}\text{Nb}_{0.5}\text{O}_{14}$ crystal," *J. Cryst. Growth* **292**(2), 408–411 (2006).
32. D. Eimerl, "Electro-optic, linear, and nonlinear optical properties of KDP and its isomorphs," *Ferroelectrics* **72**(1), 95–139 (1987).
33. B. Boulanger and G. Marnier, "Field factor calculation for the study of the relationships between all the three-wave nonlinear optical interactions in uniaxial and biaxial crystals," *J. Phys. Condens. Matter* **3**(43), 8327–8350 (1991).
34. J. Wang, H. Yu, Y. Cheng, and R. Boughton, "Recent Developments in Functional Crystals in China," *Engineering* **1**(2), 192–210 (2015).
35. W. F. Hagen and P. C. Magnante, "Efficient Second Harmonic Generation with Diffraction Limited and High Spectral Radiance Nd Glass Lasers," *J. Appl. Phys.* **40**(1), 219–224 (1969).
36. W. Q. Zhang, "Optical parametric generation for biaxial crystal," *Opt. Commun.* **105**(3), 226–232 (1994).
37. J. Q. Yao and T. S. Fahlen, "Calculations of optimum phase match parameters for the biaxial crystal KTiOPO_4 ," *J. Appl. Phys.* **55**(1), 65–68 (1984).
38. L. K. Cheng and J. D. Bierlein, "KTP and isomorphs-recent progress in device and material development," *Ferroelectrics* **142**(1), 209–228 (1993).
39. J. D. Bierlein, H. Vanherzele, and A. A. Ballman, "Linear and nonlinear optical properties of flux-grown KTiOAsO_4 ," *Appl. Phys. Lett.* **54**(9), 783–785 (1989).
40. J. T. Murray, N. Peyghambarian, and R. C. Powell, "Near infrared optical parametric oscillators," *Opt. Mater.* **4**(1), 55–60 (1994).
41. H. Zhu, G. Zhang, C. Huang, H. Wang, Y. Wei, Y. Lin, L. Huang, G. Qiu, and Y. Huang, "Electro-optic Q-switched intracavity optical parametric oscillator at 1.53 μm based on KTiOAsO_4 ," *Opt. Commun.* **282**(4), 601–604 (2009).
42. W. R. Bosenberg, L. K. Cheng, and J. D. Bierlein, "Optical parametric frequency conversion properties of KTiOAsO_4 ," *Appl. Phys. Lett.* **65**(22), 2765–2767 (1994).
43. H. Sato, M. Abe, I. Shoji, J. Suda, and T. Kondo, "Accurate measurements of second-order nonlinear optical coefficients of 6H and 4H silicon carbide," *J. Opt. Soc. Am. B* **26**(10), 1892–1896 (2009).

1. Introduction

Optical parametric generation emitting in the near infrared from 2 to 6 μm is a real need for various applications like trace gas monitoring or laser surgery [1–4]. But there is still a lack of

appropriate nonlinear crystals for high energy applications. For example, KTiOPO_4 (KTP) or the periodically-poled KTP (PPKTP) [5, 6], the periodically-poled LiNbO_3 (PPLN) [7], as well as the new CdSiP_2 (CSP) crystal [8] have very good nonlinear optical properties but they suffer from the difficulty to fabricate large samples, which forbids to use large laser beams. Nowadays, a lot of efforts have been made for investigating new kinds of nonlinear crystals for high power mid-infrared lasers. For example, 4H-SiC with a high damage threshold ($>3.0 \text{ GW/cm}^2$) has been explored to be a promising crystal for producing high-power mid-infrared lasers [9]. Recently, the Langatate $\text{La}_3\text{Ga}_{5.5}\text{Ta}_{0.5}\text{O}_{14}$ (LGT) was also reported as a novel mid-infrared nonlinear crystal with very good indicators compared to KTP [10] and with an easier crystal growth leading to very high quality and several-centimeters-size crystals thanks to the Czochralski method [11].

In the same langasite family, we identified $\text{La}_3\text{Ga}_{5.5}\text{Nb}_{0.5}\text{O}_{14}$ (LGN) [12]. LGN belongs to the 32 trigonal point group, where 3 and 2 stand for a 3-fold and a 2-fold axis respectively, leading to four non-zero and independent coefficients of the second order electric susceptibility tensor according to Neumann principal [13]. These coefficients under Kleinmann assumption are: $d_{xxx} = -d_{yyy} = -d_{yyx} = -d_{xyx}$ ($=d_{11}$) where d_{11} stands for the contracted notation [13]. The ordinary and extraordinary principal refractive indices of LGN, written n_o and n_e respectively, have been previously determined as a function of the wavelength between $0.36 \mu\text{m}$ and $2.32 \mu\text{m}$ using an oriented prism [12]. It has enabled to show that LGN is a positive uniaxial crystal ($n_o < n_e$), and the determined Sellmeier equations have been used to calculate birefringence phase-matching directions of second harmonic generation (SHG) [12]. To the best of our knowledge, no value of d_{11} and damage threshold have been reported.

In this work, we report crystal growth, transmission spectra, and accurate values of the two principal refractive indices of LGN as a function of wavelength measured using the minimum deviation technique in a prism. The fit of these data allowed us to refine the Sellmeier equations of LGN and worked out calculations for all possible phase-matched quadratic processes associated with a non-zero effective coefficient, and corresponding devices based on optical parametric generation (OPG). The second-order nonlinear coefficient d_{11} was determined using the Maker Fringe Technique, and we measured the damage threshold. We also discuss the interest of this crystal for second-order frequency conversion in the infrared range from the structural point of view.

2. Experimental methods

LGN crystal was grown using the Czochralski method. The raw materials were prepared from a mixture of La_2O_3 , Ga_2O_3 , and Nb_2O_5 powders with a purity of 99.99% in stoichiometric ratio. During the crystal growth process, an argon-oxygen atmosphere with an oxygen concentration of 2% was chosen to reduce the evaporation of the gallium sub-oxide from the melt, and an extra 2 wt% Ga_2O_3 was added to reduce the volatilization.

The transmission spectra were recorded using a 2 mm-thick x -cut slab with aperture dimensions of $4 \times 4 \text{ mm}^2$. It was uncoated and polished to optical quality. We used an ultraviolet-visible-NIR spectrometer (JASCO, Model V-570) emitting polarized light between 190 nm and 2500 nm, and a FT-IR spectrometer (NEXUS 670, Thermo Nicolet Co.) emitting unpolarized light between 2500 nm and 8000 nm.

For the measurement of refractive indices, a high optical quality LGN crystal was cut as a few centimeters prism with a vertex angle of $25.05 \pm 0.112^\circ$. The edge was cut along the c (or z) axis, so that the incidence plane corresponds to the (x,y) plane that is parallel to (a,b) plane. It has the advantage of a birefringence, *i.e.* $\Delta n = n_e - n_o$, independent of the direction of propagation, and without any spatial walk-off. The LGN prism was placed in a high precision automatic spectrometer goniometer (HR Spectro Master UV-VIS-IR from Trioptics). This commercial device provides measurements of the minimum deviation in polarized light, for eleven sets of discrete wavelengths ranging between 0.43 and $2.33 \mu\text{m}$ which values are known with a precision of 10^{-5} . By adjusting the proper orientation of the linear polarization of the input beam, it has been possible to determine the values of the ordinary and

extraordinary principal refractive indices of LGN, *i.e.* n_o and n_e , respectively, with an accuracy of 10^{-5} .

A Maker Fringe setup [14, 15] was implemented to determine the second-order electric susceptibility coefficient d_{11} of LGN relatively to d_{36} of potassium dihydrogen phosphate (KDP) at the same wavelength. The incoming beam was delivered by a Q-switched Nd:YAG laser (Spectra-Physics, Model Pro 230) at the fundamental wavelength $\lambda_\omega = 1.064 \mu\text{m}$ with a 10-Hz repetition rate and 10-ns pulse width. The averaged power $P(\lambda_\omega)$ was set at 20 mW and focused inside the LGN and KDP slabs. The corresponding beam waist radius was $w = 0.2$ mm in the samples, which ensures a propagation in the parallel beam approximation since the Rayleigh length ($z_R = 11.8$ cm) is much longer than the crystal length ($L = 1$ mm). The slabs were cut with uncoated surface dimensions of $10 \times 12 \text{ mm}^2$ polished to optical quality, the optical parallelism being less than $0.5'$ of arc. These samples were stuck on a turntable with a precision of 0.00125° (RAK100, Zolix Inc.) ensuring a continuous rotation of the crystals in the (z, y) and (x, y) planes. At room temperature, the power of the SHG generated beam, $P(\lambda_{2\omega})$ was measured as a function of the sample orientation, by using a photomultiplier tube (PMT, Hamamatsu, Model R105). It was averaged by a fast-gated integrator combined with a boxcar (Stanford Research Systems), and recorded using a software.

The optical damage was studied using a Q-switched Nd:YAG laser (ICT Laser Work Station, Piano 2000) with 10-ns pulse width and 1-Hz repetition rate. The laser beam was focused onto a polished 2-mm-thick LGN slab with aperture dimensions of $4 \times 4 \text{ mm}^2$ using a 100-mm-focal lens. The sample was moved toward the beam waist plane using a precision translation stage (Zolix Inc.), until damage was observed at the input surface of the crystal. This damage was checked by an optical microscope and this test mode is according to the International Standard Organization 11254-1 [16].

For the optical parametric generation (OPG), the pump source was a homemade Q-switched Nd:YAG laser at $1.064 \mu\text{m}$ with a pulse width of 10 ns. The input beam polarization was set ordinary. The spectrum of the light generated by the OPG was measured using two spectrometers for presenting the generated fluorescence clearly (OSA205, Thorlabs Inc. & YOKOGAWA AQ 6315A, 0.05 nm resolution).

3. Results and discussions

3.1 Crystal growth and structure

An as-grown LGN crystal weighting 410 g, with 45 mm in diameter and 100 mm in length, is shown in Fig. 1(a). Since LGN belongs to the 32 trigonal point group, the c axis of the crystallographic frame is perpendicular to the two other axis, *i.e.* a and b , making an angle of 120° . Consequently, the crystallographic frame does not correspond to the orthonormal dielectric frame (x, y, z) ; we used the following convention: a is parallel to x while y is located at 30° from b , as shown in Fig. 1(b).

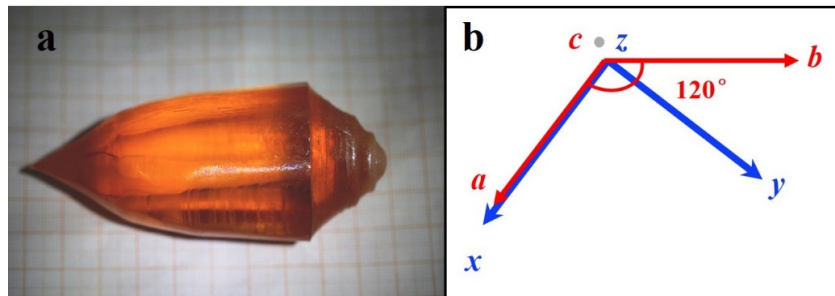


Fig. 1. (a) An as-grown LGN crystal using the Czochralski method; (b) Orientation between the crystallographic (red) and the dielectric (blue) frames.

The langasite crystallographic structure $A_3BC_3D_2O_{14}$ contains 4 cationic sites that can be occupied by different ions [17], the displacements of ions and their electron shells playing a

key role in optical effects [18]. In LGT, the Ta^{5+} ions are located in two sites (octahedral and trigonal-pyramidal) by substitution of Ga^{3+} ions thanks to the ion polarizabilities. But the structure of LGN is different: the La^{3+} ions sit in the center of (LaO_8) dodecahedron (yellow), the Ga^{3+} ions have two positions, *i.e.* (GaO_4) tetrahedron (deep green) and trigonal-pyramid (light green), and the Nb^{5+} ions are in forms of (NbO_6) octahedron, as shown in Fig. 2. The structure of LGN is formed along the shortest distance between the (LaO_8) dodecahedron and (NbO_6) octahedron. Meanwhile, the (LaO_8) dodecahedron and (NbO_6) octahedron share the O-O edge. Then the two types of (GaO_4) situated around the octahedra according to the threefold axis law. The ionic radii of Ga^{3+} (6) and Nb^{5+} (6) are 0.62 and 0.68 Å, respectively, which are close and these cations possessing ns^2np^6 electron shells could produce less localized chemical bonds which are beneficial for substituting. Then the Ga^{3+} (6) sites could be occupied by Nb^{5+} (6) forming (NbO_6) octahedra [19, 20]. Note that the Nb^{5+} ions are located only in the octahedral site that results in the deviation of the rotation of opposite faces of octahedron, these faces being normal to the *c*-axis [18]. Moreover, the octahedra are distorted, which induces a high nonlinear polarizability and also influences the infrared (IR) cut-off of the compound [21]. For comparison with other famous nonlinear oxide crystals, the borates like LiB_3O_5 (LBO) and β - BaB_2O_4 (BBO) with π -orbital borate systems have an IR cut-off around 3.2 μm [22, 23]; $LiNbO_3$ (LN) and $LiTaO_3$ (LT) [24], where (NbO_6) and (TaO_6) octahedrons exist, can reach 5.5 μm [25]. On the other hand, the IR cut-off of LGT is 6 μm [10], which is larger than that of borates. Based on the anion group theory [21, 25], LGN should have enough polarizability and a comparable transmission range to that of LGT. Another important property is that the langasite family has a much higher band gap (~6.6 eV [26] than $AgGaS_2$ (2.51 eV), $AgGaSe_2$ (1.83 eV) [27] and $ZnGeP_2$ (~2 eV) [28, 29], which indicates that LGN should have a much higher optical damage threshold.

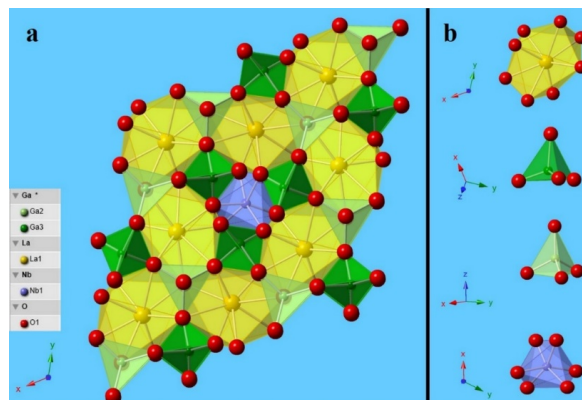


Fig. 2. (a) The fragment of the structure of LGN crystal; (b) polyhedrons of (LaO_8) , (GaO_4) and (NbO_6) .

3.2 Transmission spectra, refractive indices and Sellmeier equations

The transmission spectra are depicted in Fig. 3(a) and 3(b) respectively, the inset of Fig. 3(a) corresponding to a zoom of the ultraviolet edge. Through using the Tuac's equations $ahv = A(hv - E_g)^2$, where a is the absorption coefficient, A is an energy independent constant [30], the ultraviolet and infrared cut-offs could be estimated. The $(ahv)^2$ versus $h\nu$ has been plotted, then the indirect band-gaps were found by extrapolating the linear portion to $(ahv)^2 = 0$ (see the green indicative line in the inset of Fig. 3 (b)). Then the band-gaps are determined to be 4.43 eV and 0.167 eV and the ultraviolet cut-off could be calculated to be 0.28 μm and the infrared one should be 7.4 μm . Then LGN is transparent between 0.28 and 7.4 μm , despite a strong and narrow polarized absorption peak located at 1.85 μm due to oxygen defects during crystal growth. A smaller absorption peak exists at 3 μm because of Ga-O bonds [31]. From the transmission point of view, Fig. 3 shows that LGN could enable optical parametric

generation (OPG) covering band II of transmission of the atmosphere when pumped with femtosecond Ti:Sapphire or nanosecond Nd:YAG lasers, and that without any two photon absorption (TPA) of the pump.

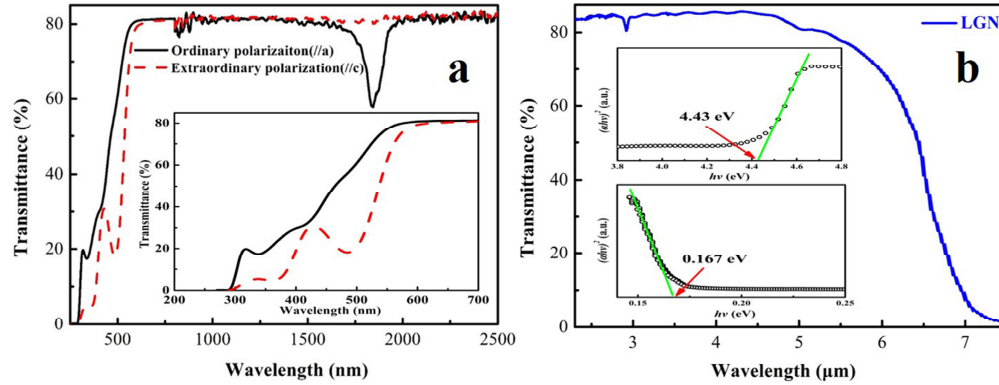


Fig. 3. LGN polarized (a) and unpolarized (b) transmission spectra as a function of wavelength through a 2-mm-thick and *x*-cut slab. The inset of (a) corresponds to a zoom of the ultraviolet edge and the insets of (b) are the $(ahv)^2$ versus hv curves for determining the ultraviolet (above) and infrared (below) cut-offs.

Table 1. Ordinary (n_o) and extraordinary (n_e) principal refractive indices, and corresponding maximal value of birefringence $\Delta n = (n_e - n_o)$ as a function of wavelength in LGN.

λ (nm)	n_e	n_o	$\Delta n = (n_e - n_o)$
435.8350	2.028173	1.992677	0.035496
479.9920	2.012033	1.978113	0.033920
546.0750	1.995363	1.962867	0.032496
587.5620	1.988239	1.956393	0.031846
643.8470	1.980643	1.949400	0.031243
706.5190	1.974146	1.943494	0.030652
768.1943	1.969443	1.939087	0.030356
852.1100	1.964365	1.934405	0.029960
1013.9800	1.958660	1.928771	0.029889
1529.5800	1.948163	1.919266	0.028897
2325.4199	1.936976	1.908830	0.028146

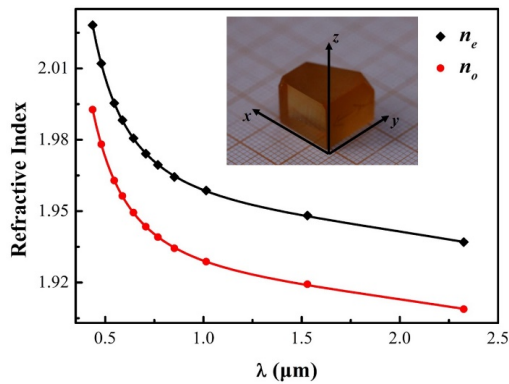


Fig. 4. Measured principal refractive indices n_o and n_e plotted as a function of wavelength (dots), and fit of these experimental data (continuous lines). The picture shows the oriented centimeter-size LGN prism that was used.

Ordinary and extraordinary principal refractive indices, n_o and n_e , respectively, were determined as a function of the wavelength presented in Fig. 4 (the inset is the LGN prism). The measured data are displayed in Table 1 for eleven sets of discrete wavelengths, showing that LGN is a positive uniaxial crystal ($n_o < n_e$) with a strong birefringence $\Delta n \sim 0.03$. By using the Levenberg-Marquardt algorithm, we fitted simultaneously the refractive indices values of Table 1 with the same form of Sellmeier equation than that given in [12] where λ is expressed in μm , which gives:

$$n_e^2(\lambda) = 3.79511 + \frac{0.0500}{\lambda^2 - 0.03405} - 0.00964\lambda^2 \quad (1)$$

$$n_o^2(\lambda) = 3.68270 + \frac{0.0464}{\lambda^2 - 0.02980} - 0.00870\lambda^2 \quad (2)$$

3.3 Nonlinear coefficient and damage threshold

Using the Maker Fringe setup, we selected type I second harmonic generation (SHG) ($1/\lambda_{2\omega}^o = 1/\lambda_\omega^e + 1/\lambda_\omega^e$) in the (y, z) plane of LGN, the corresponding effective coefficient being $d_{\text{eff}}^{yz}(\lambda_{2\omega}^o, \theta) = d_{11}(\lambda_{2\omega}^o) \cos^2(\theta - \rho(\theta, \lambda_\omega^e))$: θ is the angle of spherical coordinate from the z -axis, $\lambda_\omega = 1.064 \mu\text{m}$ which is the fundamental wavelength, $\lambda_{2\omega} = 0.532 \mu\text{m}$ which is the second harmonic wavelength, and ρ is the spatial walk-off. For this purpose, a 1-mm-length LGN slab was cut oriented along the three axes of the dielectric frame and rotated around the x -axis with the incoming beam polarized along the y -axis, as shown in Fig. 5(a). In order to perform a relative measurement relatively to the nonlinear coefficient d_{36} ($0.532 \mu\text{m}$) = 0.57 ± 0.02 pm/V of KDP [32], we implemented type I SHG ($1/\lambda_{2\omega}^e = 1/\lambda_\omega^o + 1/\lambda_\omega^o$) in the (x, y) plane of KDP where there is no spatial walk-off. The corresponding effective coefficient is $d_{\text{eff}}^{xy}(\lambda_{2\omega}^e, \varphi) = d_{36}(\lambda_{2\omega}^e) \sin(2\varphi)$ where φ is the angle of spherical coordinate from the x -axis. We used a 1.5 mm-length [110]-cut KDP slab ($\varphi = 45^\circ$) rotated around the z -axis, the incoming beam being polarized perpendicularly to this axis (see Fig. 5(b)).

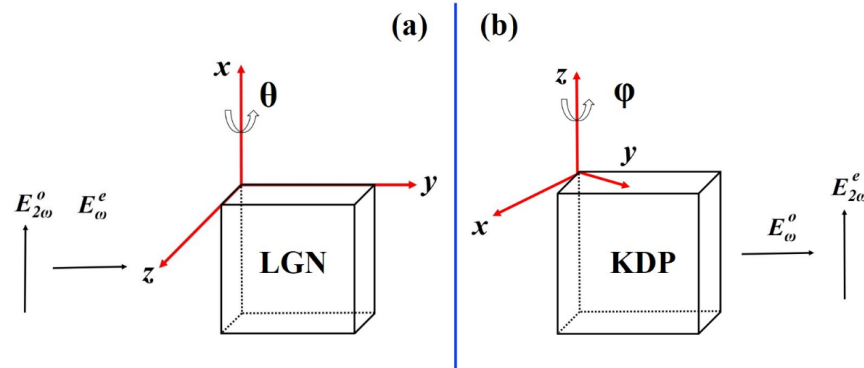


Fig. 5. Orientation and polarization schemes of LGN (a) and KDP (b) slabs.

The recorded fringe pattern involving d_{11} of LGN is shown in Fig. 6. The figure also gives a fit of our data, using [14]:

$$P(\lambda_{2\omega}, \alpha) = \beta f(\alpha) d_{ij}^2 P^2(\lambda_\omega) \frac{L^2}{w^2} \sin^2[\psi(\alpha)] \quad (3)$$

with

$$f(\alpha) = \cos(\alpha) \frac{2366 T(\lambda_{2\omega}, \alpha) T^2(\lambda_{\omega}, \alpha)}{\lambda_{\omega}^2 A(\lambda_{2\omega}, \alpha) A^2(\lambda_{\omega}, \alpha)} \quad (4)$$

and

$$\psi(\alpha) = \frac{2\pi L}{\lambda_{\omega}} \left[\sqrt{n^2(\lambda_{2\omega}, \alpha) - \sin^2(\alpha)} - \sqrt{n^2(\lambda_{\omega}, \alpha) - \sin^2(\alpha)} \right] \quad (5)$$

where α stands for θ in LGN and $(\varphi - 45^\circ)$ in KDP. L is the sample thickness, and P_{ω} and w are respectively the power and beam waist radius of the incoming beam. $T(\lambda_i, \alpha)$ is the sample Fresnel transmission coefficient and $n(\lambda_i, \alpha)$ is the refractive index, where the index $i = \omega$ stands for the input beam, and $i = 2\omega$ for the generated beam. On consideration of the absorption at the wavelength of SHG signal, the correction factor (β) has been added in Eq. (3). β could be calculated to be 1.15 by $\beta = e^{-(l_2/l_1)\ln T_1} = T_1^{(-l_2/l_1)}$ where T_1 is the transmittance of as-measured 2 mm-length sample ($l_1 = 2$ mm) in the transmission measurement, l_2 is the length of LGN sample in the Maker Fringe measurement.

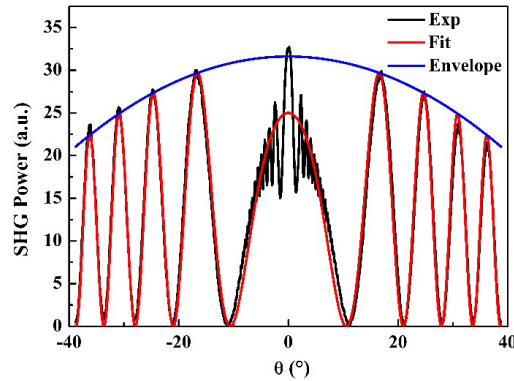


Fig. 6. Recorded (black points), fit of experimental data (red line) and of the envelope (blue line) of the Maker Fringes pattern involving d_{11} coefficient of LGN.

By fitting the envelope of the Maker fringes pattern of Fig. 6 using Eq. (1) and (2), and Eqs. (3)-(5), we determined the magnitude of its maximum value at normal incidence ($\alpha = 0^\circ$), relatively to that of KDP measured in the same condition, using:

$$\frac{d_{11}^2(\lambda_{2\omega})}{d_{36}^2(\lambda_{2\omega})} = \frac{P_{LGN}(\lambda_{2\omega}, 0) L_{KDP}^2 f_{KDP}(0) \sin^2 c^2 [\psi_{KDP}(0)]}{P_{KDP}(\lambda_{2\omega}, 0) L_{LGN}^2 f_{LGN}(0) \sin^2 c^2 [\psi_{LGN}(0)]} \quad (6)$$

with

$$\psi_{LGN}(0) = \frac{2\pi L_{LGN}}{\lambda_{\omega}} [n_o(\lambda_{2\omega}) - n_e(\lambda_{\omega})] \quad (7)$$

and

$$\psi_{KDP}(0) = \frac{2\pi L_{KDP}}{\lambda_{\omega}} [n_e(\lambda_{2\omega}) - n_o(\lambda_{\omega})] \quad (8)$$

From the measurement of the ratio $P_{LGN}(\lambda_{2\omega}, 0) / P_{KDP}(\lambda_{2\omega}, 0)$ and from Eqs. (3)-(8), we found that the second-order nonlinear coefficient of LGN is: $d_{11}(\lambda_{2\omega} = 0.532 \mu\text{m}) = 3.0 \pm 0.1$ pm/V.

The laser damage threshold was measured, using an input energy per pulse of 40 mJ at $1.064 \mu\text{m}$. Damage appeared when the beam diameter was 0.6 mm, which corresponds to a damage threshold intensity of $1.41\text{GW}/\text{cm}^2$.

3.4 Tuning curves and associated nonlinear coefficients

By using Eq. (1) and (2), we calculated all the possible tuning curves associated with a nonzero effective coefficient in the transparency range of LGN. It is the case of type I SHG ($1/\lambda_{2\omega}^o = 1/\lambda_\omega^e + 1/\lambda_\omega^o$), type I sum frequency generation (SFG) ($1/\lambda_3^o = 1/\lambda_1^e + 1/\lambda_2^e$) and type II difference-frequency generation (DFG) ($1/\lambda_1^e = 1/\lambda_3^o - 1/\lambda_2^e$) in the (y,z) plane [33]: superscripts o and e stand for the ordinary and extraordinary polarizations respectively, and we took the relation of order $\lambda_3 < \lambda_2 \leq \lambda_1$. The corresponding effective coefficient is the biggest in the (y,z) plane and given by $d_{\text{eff}}^{yz}(\lambda_i, \theta_{PM}) = d_{11}(\lambda_i) \cos^2(\theta_{PM})$ where $i = 2\omega$ (for SHG), 3 (for SFG) and 1 (for DFG) respectively, since $d_{\text{eff}}(\lambda_i, \theta_{PM}, \varphi) = d_{11}(\lambda_i) \cos^2(\theta_{PM}) \sin 3\varphi$ for arbitrary plane. Two more turning curves were found in the (x,z) plane which were type III SFG ($1/\lambda_3^o = 1/\lambda_1^e + 1/\lambda_2^e$) and type I DFG ($1/\lambda_1^e = 1/\lambda_3^o - 1/\lambda_2^e$). The corresponding effective coefficients which are the biggest in the (x,z) plane are given by $d_{\text{eff}}^{xz}(\lambda_i, \theta_{PM}) = d_{11}(\lambda_i) \cos(\theta_{PM})$ since $d_{\text{eff}}(\lambda_i, \theta_{PM}, \varphi) = d_{11}(\lambda_i) \cos(\theta_{PM}) \cos 3\varphi$ for arbitrary plane, where $i = 2\omega$ (for SHG), 3 (for SFG) and 1 (for DFG) respectively, and θ_{PM} is the phase-matching angle. The calculated phase-matching wavelength of type I SHG is shown as a function of θ_{PM} in Fig. 7. The cases of type I- and type III- SFG with $\lambda_2 = 1.5 \mu\text{m}$ are shown in Fig. 8(a) and 8(b) respectively. Figures 9(a) and 9(b) give the calculated tuning curves of type II- and type I- DFG with $\lambda_2 = 1.064 \mu\text{m}$ respectively. Figures 7 to 9 also give the tuning curves calculated by using Sellmeier equations of [12], which highlights a strong discrepancy with our calculations, probably due to a lower accuracy of data recorded in [12], especially above $1.5 \mu\text{m}$.

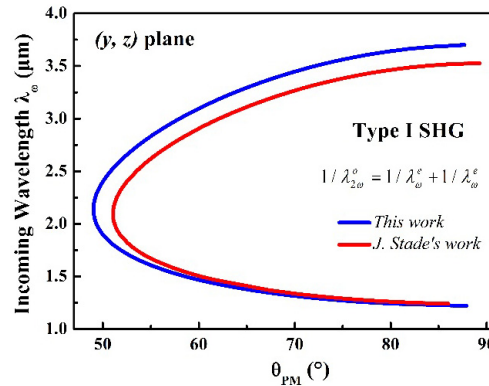


Fig. 7. Calculated type I SHG tuning curve as a function of the phase-matching angle θ_{PM} in the (y,z) plane of LGN.

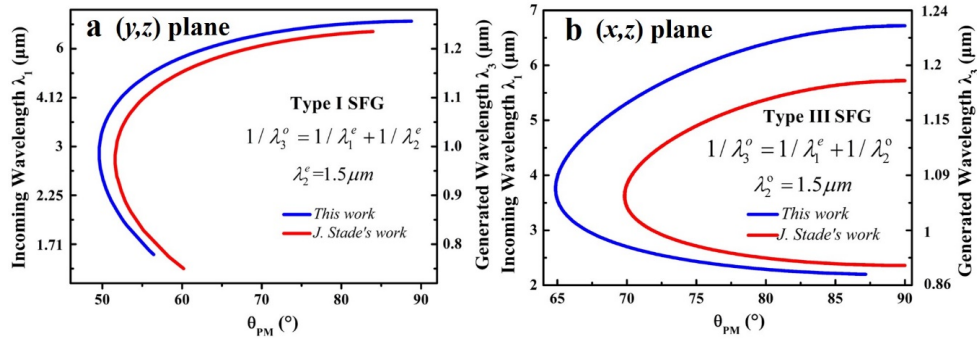


Fig. 8. Calculated tuning curves of (a) type I SFG and (b) type III SFG, with $\lambda_2 = 1.5 \mu\text{m}$ as a function of the phase-matching angle θ_{PM} in the (y,z) and (x,z) planes of LGN, respectively.

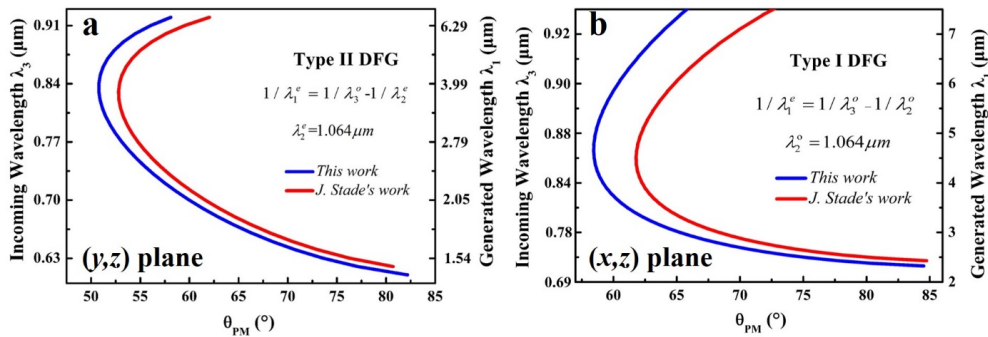


Fig. 9. (a) Calculated tuning curves of (a) type II DFG and (b) type I DFG, with $\lambda_2 = 1.064 \mu\text{m}$ as a function of the phase-matching angle θ_{PM} in the (y,z) and (x,z) planes of LGN, respectively.

We also calculated $d_{\text{eff}}^{yz}(\lambda_1, \theta_{PM})$ and $d_{\text{eff}}^{xz}(\lambda_1, \theta_{PM})$ associated to type II DFG and type I DFG tuning curves with $\lambda_2 = 1.064 \mu\text{m}$ in the (y,z) and (x,z) plane of LGN respectively. They are depicted in Fig. 10(a) as a function of the generated phase-matching wavelength λ_l . Fig. 10(a) also shows the calculated magnitude of the spatial walk-off angle ρ that is given by: $\tan \rho(\lambda_1, \theta) = \left[\sin \theta \cos \theta (n_e^2(\lambda_1) - n_o^2(\lambda_1)) \right] \cdot (n_e^2(\lambda_1) \cos^2 \theta + n_o^2(\lambda_1) \sin^2 \theta)^{-1}$ [25]. We used Eqs. (1) and (2), and the angle $\theta = 45^\circ$ where the spatial walk-off is maximum. The corresponding angular acceptance (expressed in mrad cm) and spectral acceptance (expressed in $10^{-2} \mu\text{m mm}$) defined for type II DFG and type I DFG are respectively given as:

$$(\Delta\theta \cdot L)^{yz} = \lambda_1 \lambda_2 \left\{ \frac{\sin 2\theta \cdot [\lambda_1 \cdot (n_o(\lambda_2)^{-2} - n_e(\lambda_2)^{-2}) \cdot n_e^3(\lambda_2, \theta)]}{+ \lambda_2 \cdot (n_o(\lambda_1)^{-2} - n_e(\lambda_1)^{-2}) \cdot n_e^3(\lambda_1, \theta)} \right\}^{-1} \quad (9)$$

$$(\Delta\theta \cdot L)^{xz} = \lambda_1 \left[\sin 2\theta \cdot (n_o(\lambda_1)^{-2} - n_e(\lambda_1)^{-2}) \cdot n_e^3(\lambda_1, \theta) \right]^{-1} \quad (10)$$

$$\Delta\lambda \cdot L = 0.5 \cdot \left\{ \frac{n_e(\lambda_1) \cdot (\lambda_1 - 0.9398\lambda_1\lambda_3)^{-2} - \left[0.00964 + 0.05(\lambda_1^2 - 0.03405)^{-2} \right] \cdot n_e(\lambda_1)^{-1}}{(1 - 0.9398\lambda_3)^{-2} - \left[0.0087 + 0.0464(\lambda_3^2 - 0.0298)^{-2} \right] \cdot n_o(\lambda_3) - n_o(\lambda_3) \cdot \lambda_3^{-2}} \right\}^{-1} \quad (11)$$

where $n^e(\lambda, \theta) = [n_o^{-2}(\cos \theta)^2 + n_e^{-2}(\sin \theta)^2]^{-0.5}$ is the extraordinary layer of the index surface. These acceptances are shown in Fig. 10(b) as a function of the incoming wavelength λ_3 [25]. The corresponding values of phase-matching angles can be found using Fig. 9.

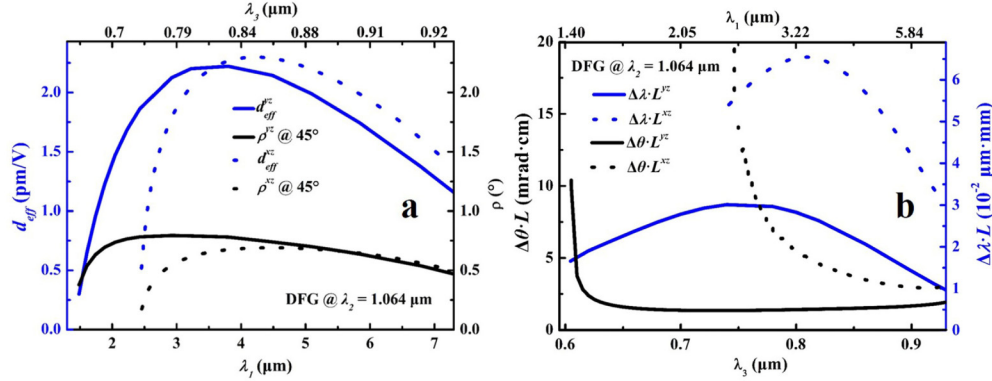


Fig. 10. (a) Second-order effective coefficients $d_{eff}^{yz}(\lambda_1, \theta_{PM})$ (blue continuous line) and $d_{eff}^{xz}(\lambda_1, \theta_{PM})$ (blue dashed line), and walk-off angle (black continuous line for (y,z) plane and black dashed line for (x,z) plane) as a function of the generated phase-matching wavelength λ_1 . (b) Angular and spectral acceptances (continuous line for (y,z) plane and dashed line for (x,z) plane) as a function of λ_3 in LGN. They are associated to type II- and type I- DFG tuning curves of Fig. 9 in LGN, respectively.

From the previous calculations, it appears that LGN will have a much higher conversion efficiency in the (x,z) than in the (y,z) plane, essentially because the trigonometric function is $\cos(\theta_{PM})$ for the former and $\cos^2(\theta_{PM})$ for the latter. However, in both planes, since $\theta_{PM} \geq 45^\circ$ is always fulfilled in LGN with $\lambda_2 = 1.064 \mu\text{m}$, the value of the walk-off angle remains lower than 0.8° and decreases when the generated wavelength λ_1 increases. On the other hand, the angular acceptances are always higher than 1.35 mrad cm , and the spectral acceptances are always lower than $7 \times 10^{-2} \mu\text{m mm}$, for type I and type II DFG. All these properties are in advantage of LGN, especially for DFG processes in the infrared range.

Using our refined Sellmeier equations, type II OPG tuning curves associated with a maximal conversion efficiency have been calculated in the (y, z) plane of LGN. Figure 11 gives the corresponding idler (λ_i) and signal (λ_s) wavelengths as a function of the phase-matching angle θ_{PM} , with $\lambda_p < \lambda_s < \lambda_i$ and $\lambda_s^{-1} + \lambda_i^{-1} = \lambda_p^{-1}$. We selected several pump wavelengths: $\lambda_p = 1.064 \mu\text{m}$ emitted by the Nd:YAG laser (see Fig. 11(a)), and $\lambda_p = 0.78 \mu\text{m}$, $0.88 \mu\text{m}$ and $0.98 \mu\text{m}$ emitted by the Ti:Sapphire laser (see Fig. 11(b)). Figure 11 shows that a LGN-OPG can emit over the whole transparency range of the crystal when rotated by an internal angle of the order of 40° . Furthermore, a super continuum is generated when LGN is pumped at $\lambda_p = 0.98 \mu\text{m}$ and oriented at $(\theta_{PM} = 51.5^\circ, \varphi_{PM} = 90^\circ)$: it corresponds to the highest value of the spectral acceptance in this crystal, which may lead to a super continuum ranging between $1.56 \mu\text{m}$ and $3.54 \mu\text{m}$. It is also associated to the maximal magnitude of the second-order effective coefficient: *i.e.* $d_{eff} = 2.19 \text{ pm/V}$ (see Fig. 10(a)).

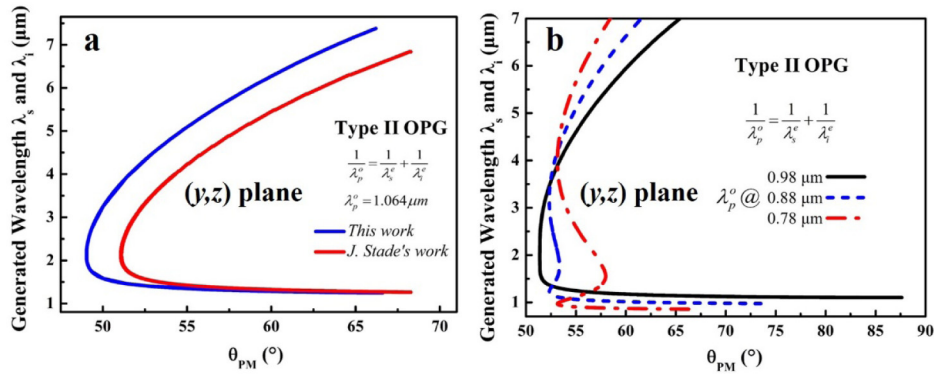


Fig. 11. Calculated type II-OPG tuning curves in the (y, z) plane of LGN with a pump wavelength of (a) $1.064 \mu\text{m}$, (b) $0.98 \mu\text{m}$, $0.88 \mu\text{m}$, and $0.78 \mu\text{m}$. λ_i and λ_s are the idler and signal wavelengths, respectively.

3.5. A Nd:YAG pumped LGN optical parametric generator

A type II OPG pumped at $1.064 \mu\text{m}$ was implemented, using a LGN slab with dimensions of $4 \times 4 \times 21 \text{ mm}^3$. It was cut in the (y, z) plane along the phase-matching direction ($\theta_{PM} = 52^\circ$, $\varphi_{PM} = 90^\circ$) polished to optical quality and uncoated. Figure 12 shows the recorded signal and idler spectrum of the type II LGN-OPG measuring by OSA205 (Thorlabs Inc.) ranging from $1.06 \mu\text{m}$ to $4.7 \mu\text{m}$. The inset of Fig. 12 shows the signal spectra from $1.43 \mu\text{m}$ to $1.46 \mu\text{m}$ measuring by YOKOGAWA AQ 6315A ranging from $1.4 \mu\text{m}$ to $1.475 \mu\text{m}$. The emission of a signal beam at $\lambda_s = 1.43 \mu\text{m}$ and an idler beam at $\lambda_i = 4.14 \mu\text{m}$ are expected in this direction by using our Eqs. (1) and (2). For comparison, we find $\lambda_s = 1.64 \mu\text{m}$ and $\lambda_i = 3.03 \mu\text{m}$, if Sellmeier equations of [12] are used. These two sets of calculated wavelengths are marked out in Fig. 12. It clearly shows that our experimental spectrum is consistent with our calculation, contrary to the calculations using Sellmeier equations from [12]. Further experiments will be devoted to optical parametric oscillation (OPO), using the proper cavity design and coating of the LGN crystal faces.

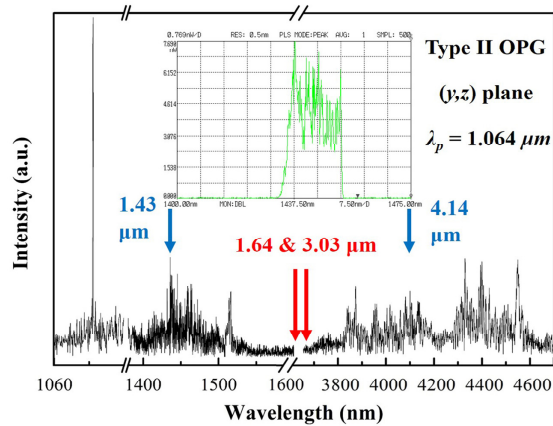


Fig. 12. Recorded spectra (black lines for the OSA205, Thorlabs Inc. and the inset for YOKOGAWA AQ 6315A spectrum analyzer) at the output of a LGN-OPG pumped by a Nd:YAG laser at $1.064 \mu\text{m}$. Arrows mark calculations using our Sellmeier equations (blue) and the dispersion equations of [12] (red).

3.6 Comparison with nonlinear crystals of references

The relevant parameters of the reference nonlinear crystals for the emission between 2 and 6 μm *i.e.* LN, KTP, KTA, 4H-SiC and LGT are depicted in Table 2. It shows that LGN has the largest transparency and phase-matching ranges. Furthermore, LGN has the following advantages like the walk-off angle and the angular acceptance. And its damage threshold is high (even if 4 times lower than that of LGT and 2 times lower than 4H-SiC). But the nonlinear coefficient d_{11} of LGN is a little bit higher than that of LGT. However, LGN crystallize in the 32 point group as LGT, which leads to a defavorable trigonometric function at the level of the effective coefficient d_{eff} when compared to other nonlinear crystals of Table 2. Fortunately, this disadvantage can be compensated by the fact that LGN (as LGT) can be grown with large dimensions. Nowadays, the biggest size of optical grade LGS crystal could reach $\Phi 52 \text{ mm} \times 100 \text{ mm}$ [34]. Then LGN (as LGT) can be grown as large as LGS after optimizing the crystal growth techniques. Thanks to these advantages, LGN permits at first the use of large beam size so that very high energy can be considered while remaining below the intensity damage threshold, and secondly it enables a long interacting length that is favorable for maximizing the conversion efficiency.

Table 2. Comparison of some parameters of LGN with other nonlinear crystals that can be used in OPG for an emission between 2 μm and 6 μm .

Crystal	LN	KTP	KTA	4H-SiC	LGT	LGN
Point Group	$3m$	$mm2$	$mm2$	$6mm$	32	32
Transmission range (μm)	0.35~5.5	0.35~4.5	0.35~5.3	0.37~6	0.3~6.8	0.28~7.4
Nonlinear coefficient (pm/V) @ 0.532 μm	$d_{31} = 4.35$	$d_{32} = 2.65$	$d_{32} = 4.5$	$d_{15} = 6.7$	$d_{11} = 2.4$	$d_{11} = 3.0$
Maximum spatial walk-off angle ($^\circ$) @ 3 μm	2	2.5	1.6			0.67
Angular acceptance (mrad cm) @ 1.5 μm	0.69	1.7	1.1			~2
Damage threshold (GW/cm ²) @ 1.064 μm	0.1	0.65	1.2	3.0	4.34	1.41
References	[25,35]	[36–39]	[39–42]	[9,43]	[10,11]	this work

4. Summary

The linear and nonlinear optical properties of nonlinear second-order frequency conversions have been studied in detail in the new Langanite crystal $\text{La}_3\text{Ga}_{5.5}\text{Nb}_{0.5}\text{O}_{14}$ (LGN). The crystal structure analysis predicted large transmission range, high hyperpolarizability and high damage threshold. We found that the transparency is ranging between 0.28 and 7.4 μm , the nonlinear coefficient $d_{11} = 3.0 \pm 0.1 \text{ pm/V}$ at 0.532 μm , and the optical damage threshold is 1.41 GW/cm². The fit of the measured principal refractive indices as a function of wavelength allowed us to calculate all possible tuning curves associated with a non-zero effective coefficient. A supercontinuum between 1.5 and 3.5 μm could be generated when pumped by a Ti:Sapphire laser. Furthermore, our calculations are consistent with the recorded spectrum at the output of a LGN-OPG pumped at 1.064 μm . From these results, LGN appears as a promising large size crystal for high energy generation in band II [3-5 μm] of transmission of the atmosphere, for Lidar applications for example. It gives also inspiration for the study and development of other nonlinear crystals from the same chemical family.

Funding

National Natural Science Foundation of China (51422205 and 51272131); Natural Science Foundation for Distinguished Young Scholars of Shandong Province (JQ201415); Taishan Scholar Foundation of Shandong Province, China.



Phase-matching properties and refined Sellmeier equations of $\text{La}_3\text{Ga}_{5.5}\text{Nb}_{0.5}\text{O}_{14}$

FENG GUO,^{1,3} DAZHI LU,^{1,2,3} PATRICIA SEGONDS,^{1,*} JÉRÔME DEBRAY,¹
HAOHAI YU,² HUAJIN ZHANG,² JIYANG WANG,² AND BENOÎT BOULANGER¹

¹Univ. Grenoble Alpes, CNRS, Grenoble INP, Institut Néel, 38000 Grenoble, France

²State Key Laboratory of Crystal Materials and Institute of Crystal Materials, Shandong University, Jinan 250100, China

³These authors contribute equally to this work.

*patricia.segons@neel.cnrs.fr

Abstract: We directly measured the phase-matching angles of second-harmonic generation and difference-frequency generation up to $6.5\ \mu\text{m}$ in the Langanate crystal $\text{La}_3\text{Ga}_{5.5}\text{Nb}_{0.5}\text{O}_{14}$ (LGN). We also determined the nonlinear coefficient and damage threshold. We refined the Sellmeier equations of the ordinary and extraordinary principal refractive indices, and calculated the conditions of supercontinuum generation.

© 2018 Optical Society of America under the terms of the [OSA Open Access Publishing Agreement](#)

OCIS codes: (190.2620) Harmonic generation and mixing; (190.4400) Nonlinear optics, materials; (190.4975) Parametric processes.

References and links

1. E. Boursier, P. Segonds, B. Boulanger, C. Félix, J. Debray, D. Jegouso, B. Ménaert, D. Roshchupkin, and I. Shoji, "Phase-matching directions, refined Sellmeier equations, and second-order nonlinear coefficient of the infrared Langatate crystal $\text{La}_3\text{Ga}_{5.5}\text{Ta}_{0.5}\text{O}_{14}$," *Opt. Lett.* **39**(13), 4033–4036 (2014).
2. D. Z. Lu, T. X. Xu, H. H. Yu, Q. Fu, H. J. Zhang, P. Segonds, B. Boulanger, X. Y. Zhang, and J. Y. Wang, "Acentric Langanite $\text{La}_3\text{Ga}_5\text{SiO}_{14}$ crystal: a new nonlinear crystal for the generation of mid-infrared parametric light," *Opt. Express* **24**(16), 17603–17615 (2016).
3. J. Stade, L. Bohaty, M. Hengst, and R. B. Heimann, "Electro-optic, piezoelectric and dielectric properties of Langasite ($\text{La}_3\text{Ga}_5\text{SiO}_{14}$), Langanite ($\text{La}_3\text{Ga}_{5.5}\text{Nb}_{0.5}\text{O}_{14}$) and Langataite ($\text{La}_3\text{Ga}_{5.5}\text{Ta}_{0.5}\text{O}_{14}$)," *Cryst. Res. Technol.* **37**(10), 1113–1120 (2002).
4. B. Boulanger, J. P. Fève, G. Marnier, C. Bonnin, P. Villeval, and J. J. Zondy, "Absolute measurement of quadratic nonlinearities from phase-matched second-harmonic generation in a single KTP crystal cut as a sphere," *J. Opt. Soc. Am. B* **14**(6), 1380–1386 (1997).
5. B. Boulanger and J. Zyss, in *International Tables for Crystallography*, A. Authier, ed., Vol. D of Physical Properties of Crystals (Kluwer Academic, 2004), pp. 178–219.
6. R. C. Miller, "Optical second harmonic generation in piezoelectric crystals," *Appl. Phys. Lett.* **5**(1), 17–19 (1964).
7. V. Petrov, M. Ghotbi, O. Kokabee, A. Esteban-Martin, F. Noack, A. Gaydardzhiev, I. Nikolov, P. Tzankov, I. Buchvarov, K. Miyata, A. Majchrowski, I. V. Kityk, F. Rotermund, E. Michalski, and M. Ebrahim-Zadeh, "Femtosecond nonlinear frequency conversion based on BiB_3O_6 ," *Laser Photonics Rev.* **4**(1), 53–98 (2010).

1. Introduction

We identified the Langatate $\text{La}_3\text{Ga}_{5.5}\text{Ta}_{0.5}\text{O}_{14}$ (LGT) as a serious candidate for the parametric generation between 3 and $6.5\ \mu\text{m}$ [1]. We then focused on a new compound of the same family, *i.e.* the Langanate $\text{La}_3\text{Ga}_{5.5}\text{Nb}_{0.5}\text{O}_{14}$ (LGN). We reported in a previous paper that when the transmittance is half its maximal value, the ultraviolet cut-off is down to $0.35\ \mu\text{m}$ and the infrared cut-off is up to $6.5\ \mu\text{m}$, in very high quality and large-size crystals grown with the Czochralski method [2]. Since LGN crystallizes in the 32 trigonal point group, there is only one nonzero element of its second-order electric susceptibility tensor under Kleinman symmetry, *i.e.* $d_{xxx} = -d_{yyy} = -d_{xyy} = -d_{yyx}$ ($=d_{11}$) where d_{11} stands for the contracted notation. We found that the absolute magnitude of d_{11} is equal to $3.0 \pm 0.1\ \text{pm/V}$ at $0.532\ \mu\text{m}$ using the Maker fringes method [2]. We also reported a damage threshold of $1.41\ \text{GW/cm}^2$ at $1.064\ \mu\text{m}$ in the nanosecond regime [2]. LGN is a positive uniaxial crystal, so that the ordinary principal refractive index (n_o) is smaller than the extraordinary one (n_e). Both indices

were previously measured as a function of the wavelength using an oriented prism, which enabled to determine Sellmeier equations valid between 0.36 and 2.32 μm [3]. Using the same method, we proposed an alternative set of equations valid between 0.43 and 2.3 μm [2].

Using sets of equations from [2] and [3], we did not find the same calculated phase-matching tuning curves in the principal dielectric planes of LGN for all the possible quadratic processes associated with a non-zero conversion efficiency [2]. Then we decided to directly record these curves, which is described in the present paper. We report for the first time to the best of our knowledge the direct measurement in LGN of the phase-matching tuning curves of second harmonic generation (SHG) and difference frequency generation (DFG). A simultaneous fit of all our data allowed us to refine the Sellmeier equations of the two principal refractive indices of LGN. We also determined the nonlinear coefficient d_{11} at another wavelength from [2] and the damage threshold. We could then calculate the conditions of supercontinuum generation.

2. Phase-matching angles and Sellmeier equations

The LGN crystal was cut and polished as a sphere with a diameter of 10.8 mm and asphericity below 1%. It was stuck on a goniometric head as shown in Fig. 1(a). It was successively oriented along the x - and y - dielectric axes with an accuracy better than 0.5° , using the X-ray backscattered Laue method. Then the LGN sphere was placed at the center of an Euler circle to be rotated in any direction. Thus any directions of the two (y, z) and (x, z) principal dielectric planes can be addressed successively in the same sample.

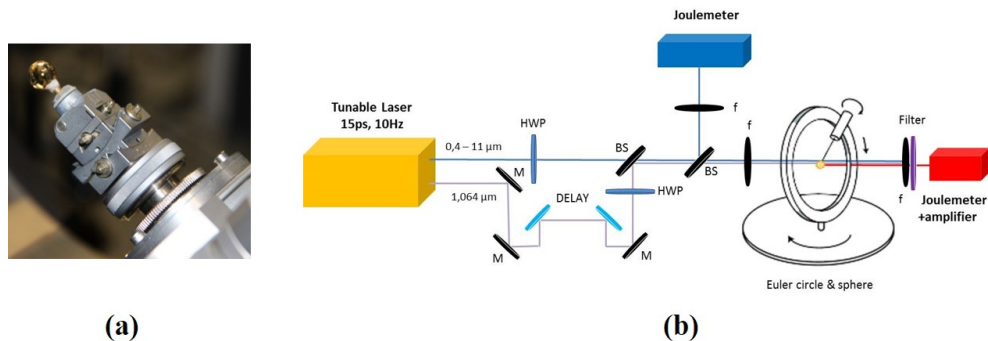


Fig. 1. (a) Picture of the LGN crystal sphere stuck on a goniometric head; (b) Setup used for the direct measurement of SHG and DFG phase-matching tuning curves.

Only one incoming beam tunable between 0.4 and 11 μm is used for studying SHG. It was emitted by a Light Conversion optical parametric generator (OPG) with 15-ps FWHM and 10-Hz repetition rate. The OPG is pumped by the third-harmonic of a beam at 1.064 μm emitted by a Excel Technology Nd:YAG laser. Thus for the study of DFG, we can combine the OPG beam with part of the 1.064 μm beam directly in the sphere as shown in Fig. 1(b).

A 100-mm-focusing lens (f) placed at the entrance side of the sphere ensured normal incidence and quasi-parallel propagation of all the input beams along any diameter of the sphere. The polarization was adjusted by using achromatic half-wave-plates (HWP).

The energy of the incoming beams was measured with a J4-09 Moletron pyroelectric joulemeter placed behind a beam splitter (BS) and a lens with a focal length of 50 mm. The energy of the generated beam was measured simultaneously at the exit of the sphere by a J3-05 Moletron pyroelectric joulemeter associated with a PEM531 amplifier. A filter removed all input beams. The phase-matching wavelengths were controlled by monitoring the wavelengths of the input beams between 0.4 and 1.7 μm with accuracy of ± 1 nm using HR 4000 and of ± 3 nm with NIRquest 512 Ocean Optics spectrometer. The phase-matching

angles were read on the Euler circle with an accuracy of $\pm 0.5^\circ$. A phase-matching direction is detected when the conversion efficiency reaches a maximal value.

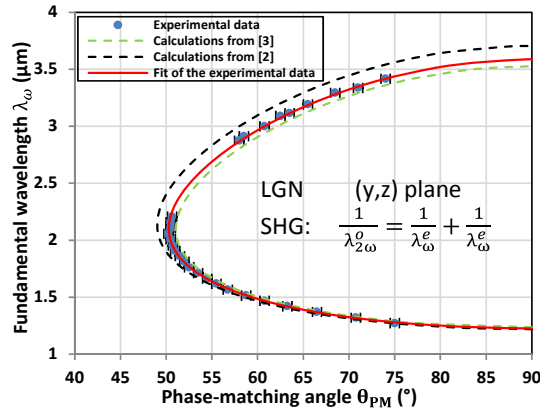


Fig. 2. SHG tuning curve in the (y, z) plane of LGN. Wavelengths accuracy is within dots size.

The recorded SHG and DFG phase-matching tuning curves are shown in Figs. 2 and 3, respectively. We studied type I SHG ($1/\lambda_{2\omega}^o = 1/\lambda_\omega^e + 1/\lambda_\omega^e$) and type II DFG ($1/\lambda_i^e = 1/\lambda_p^o - 1/\lambda_s^e$) in the (y, z) plane, and type III DFG ($1/\lambda_i^o = 1/\lambda_p^o - 1/\lambda_s^e$) in the (x, z) plane. Superscripts o and e stand for the ordinary and extraordinary waves, respectively. λ_ω and $\lambda_{2\omega}$ are the fundamental and second harmonic wavelengths. λ_p , λ_s and λ_i are respectively the pump, signal and idler wavelengths verifying $\lambda_p < \lambda_s \leq \lambda_i$.

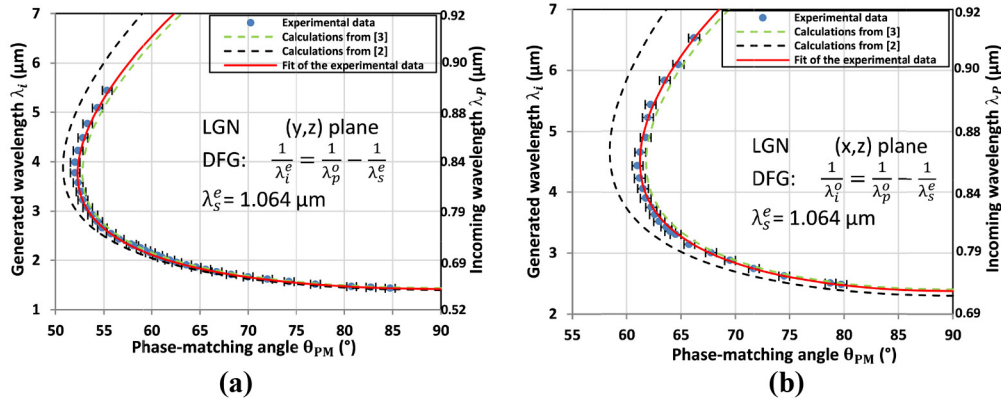


Fig. 3. DFG tuning curve (a) in the (y, z) and (b) in the (x, z) plane of LGN. Wavelengths accuracy is within dots size.

Figures 2 and 3 also show the calculated phase-matching curves using the Sellmeier equations from Refs [2]. and [3]. It highlights discrepancies between our experimental data and both sets of calculations, even if calculations using [3] are closer to our experimental data. It is true especially above $2.3 \mu\text{m}$ that corresponds to the limit of the spectral range over which the ordinary and extraordinary principal refractive indices were determined in Refs [2]. and [3]. As shown in Fig. 4, by performing our measurements up to $6.5 \mu\text{m}$, we widely extended the wavelength range where the two principal refractive indices of LGN are involved. Such a difference might explain the discrepancies shown in Fig. 2 and 3.

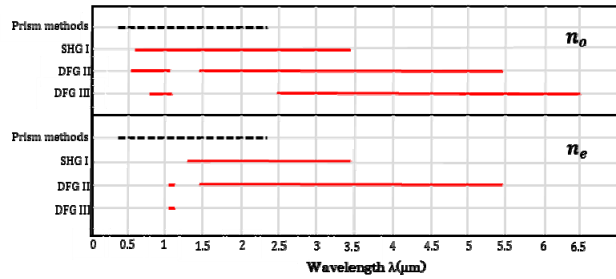


Fig. 4. Spectral ranges where the principal refractive indices of LGN, n_o and n_e , are involved, using the sphere method (red lines), and the prism technique from [2] and [3] (black dashed lines).

We refined the Sellmeier equations of LGN by the simultaneous fit of all our SHG and DFG experimental data shown in Fig. 2 and 3. We used the Levenberg-Marquardt algorithm encoded with Matlab. Among the several possible forms of Sellmeier equations to fit the ordinary and extraordinary refractive indices, the best one was that used in Refs [2, 3], *i.e.*:

$$n_j^2(\lambda) = A_j + \frac{B_j}{\lambda^2 - C_j} - D_j \lambda^2 \quad (1)$$

where λ is in μm and j stands for o or e . The precision of our angular measurements is $\pm 0.5^\circ$, leading to a relative accuracy $\Delta n_j / n_j$ better than 10^{-4} . The numerical values of the best fit parameters A_j , B_j , C_j and D_j are summarized in Table 1. Our interpolated tuning curves using the Sellmeier equations of the present work correspond to the continuous red lines shown Figs. 2 and 3. They clearly show a much better agreement with our experimental data than using the calculations from Refs [2]. and [3].

Table 1. Refined Sellmeier Coefficients of the Two Principal Refractive Indices n_o and n_e of LGN

Sellemeir coefficients	A_j	B_j	C_j	D_j
$j = o$	3.6836	0.0460	0.0296	0.0094
$j = e$	3.7952	0.0483	0.0314	0.0102

3. Nonlinear coefficient and damage threshold

The absolute value of d_{11} of LGN can be determined from angle critical phase-matched type I SHG in the (y, z) plane. The corresponding effective coefficient is expressed as:

$$d_{eff}^{LGN} = d_{11}^{LGN}(\lambda_{2\omega_1}) \cos^2[\theta_{PM_1} - \rho^e(\theta_{PM_1}, \lambda_{\omega_1})] \quad (2)$$

where $\rho^e(\theta_{PM_1}, \lambda_{\omega_1})$ stands for the spatial walk-off.

We chose the nonlinear coefficient of KTP $d_{24}^{KTP}(\lambda_{2\omega_2} = 0.66 \mu\text{m}) = 2.37 \pm 0.17 \text{ pm/V}$ as a reference [4] for the determination of d_{11} of LGN. The coefficient d_{24}^{KTP} governs type II SHG ($1/\lambda_{\omega_2}^e + 1/\lambda_{\omega_2}^o = 1/\lambda_{2\omega_2}^o$) in the (x, z) plane of KTP, the corresponding effective coefficient being $d_{eff}^{KTP} = d_{24}^{KTP}(\lambda_{2\omega_2}) \sin[\theta_{PM_2} - \rho^e(\theta_{PM_2}, \lambda_{\omega_2})]$ with $\theta_{PM_2} = 58.5^\circ$ and $\rho^e(\theta_{PM_2}, \lambda_{\omega_2}) = 2.57^\circ$ at the fundamental wavelength $\lambda_{\omega_2} = 1.32 \mu\text{m}$. A LGN slab was then cut at $(\theta_{PM_1} = 70.4^\circ, \varphi_{PM_1} = 90^\circ)$ according to our refined Sellmeier equations, the goal being to study the SHG in LGN at a fundamental wavelength the closest as possible to that of KTP. It has the advantage that we could get rid of the spectral response of the experimental

setup. The LGN and KTP slabs were cut with the same small thickness $L = 0.52$ mm. The fundamental beam emitted by the OPG was focused with a 100-mm-focal length CaF_2 lens. Then the beam waist diameter was $w_o = 120$ μm on the two slabs surface, with a Rayleigh length of 30 mm that is much longer than L . Then parallel beam propagation was ensured, and the spatial walk-off attenuation is minimized.

The fundamental beam energy was measured with the J4-09 Moletron pyroelectric joulemeter placed behind a beam splitter and a lens with a focal length of 50 mm. The SHG energy was measured at the exit of each slab by the J3-05 Moletron pyroelectric joulemeter combined with a PEM531 amplifier, while a filter removed the input beam. Then we can determine the corresponding SHG conversion efficiency of type I SHG in LGN (η_I^{LGN}), and that of type II SHG in KTP (η_{II}^{KTP}).

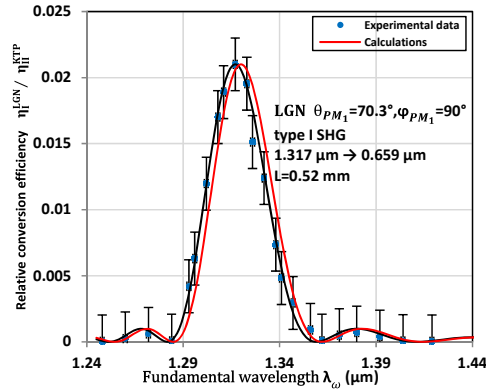


Fig. 5. Calculated (red line) and measured (dots linked with black line) conversion efficiency in LGN relatively to KTP, as a function of the fundamental wavelength. Wavelengths accuracy is within dots size.

Figure 5 shows the ratio $\eta_I^{\text{LGN}} / \eta_{II}^{\text{KTP}}$ recorded as a function of the fundamental wavelength λ_o . The peak wavelength is $\lambda_{o_1} = 1.317$ μm for LGN, which is very close to the targeted value λ_{o_2} . The spectral acceptance $L \cdot \delta\lambda_{o_1}$ is equal to 19.8 mm nm. It is in very good agreement with the calculation using our refined Sellmeier equations. In these conditions, we can calculate $d_{\text{eff}}^{\text{LGN}}$ relatively to $d_{\text{eff}}^{\text{KTP}}$ as follows:

$$\left(d_{\text{eff}}^{\text{LGN}}\right)^2 = \frac{\eta_I^{\text{LGN}}}{\eta_{II}^{\text{KTP}}} \frac{L_{\text{KTP}}^2}{L_{\text{LGN}}^2} \frac{G_{II}^{\text{KTP}}}{G_I^{\text{LGN}}} \frac{A_{II}^{\text{KTP}}}{A_I^{\text{LGN}}} \left(d_{\text{eff}}^{\text{KTP}}\right)^2 \quad (3)$$

with

$$A_I^{\text{LGN}} = \frac{T_o^{\text{LGN}}(\lambda_{2\omega_1}, \theta_{PM_1})}{n_o^{\text{LGN}}(\lambda_{2\omega_1}, \theta_{PM_1})} \left[\frac{T_e^{\text{LGN}}(\lambda_{\omega_1})}{n_e^{\text{LGN}}(\lambda_{\omega_1})} \right]^2 \quad (4)$$

and

$$A_{II}^{\text{KTP}} = \frac{T_o^{\text{KTP}}(\lambda_{2\omega_2})}{n_o^{\text{KTP}}(\lambda_{2\omega_2})} \frac{T_e^{\text{KTP}}(\lambda_{\omega_2}, \theta_{PM_2})}{n_e^{\text{KTP}}(\lambda_{\omega_2}, \theta_{PM_2})} \frac{T_o^{\text{KTP}}(\lambda_{\omega_2})}{n_o^{\text{KTP}}(\lambda_{\omega_2})} \quad (5)$$

n_o and n_e are the ordinary and extraordinary refractive indices. They were calculated at $\lambda_{o_1} = 1.317$ μm for LGN using Eq. (1) and Table 1, and at $\lambda_{o_2} = 1.320$ μm for KTP using

respectively the phase-matching angles θ_{PM_1} and θ_{PM_2} defined above and [4]. T_o and T_e are the corresponding Fresnel transmission coefficients. For LGN, the spatial walk-off angle $\rho^e(\theta_{PM_1}, \lambda_{\omega_1}) = 0.55^\circ$ and the spatial walk-off attenuation $G_T^{LGN} = 0.999$. $G_{II}^{KTP} = 0.987$ for KTP [4,5]. Note that Fig. 5 shows a conversion efficiency of KTP that is two orders of magnitude higher than that of LGN: it is due to the relative value of their trigonometric functions that weigh differently on the nonlinear coefficients at the considered phase-matching angles. According to Eq. (2), we found that $|d_{11}(0.659 \mu\text{m})| = 2.9 \pm 0.5 \text{ pm/V}$ and $\delta_{11} = 0.284 \pm 0.049 \text{ pm/V}$, the Miller index [6], which corroborates the result obtained using the Maker fringes technique [2]. Furthermore it is also very close to $|d_{24}(0.660 \mu\text{m})| = 2.37 \pm 0.17 \text{ pm/V}$ of KTP [4], and a little bit larger than $|d_{11}(0.659 \mu\text{m})| = 2.4 \pm 0.4 \text{ pm/V}$ of LGT [1].

We also determined the surface damage threshold of the same LGN and KTP slabs. Both crystals were illuminated by the same Nd:YAG laser at $1.064 \mu\text{m}$ with a very high beam quality, a pulse duration of 5 ns (FWHM) and repetition rate of 10 Hz. By using a 100-mm-focal BK7 lens, we measured a beam waist diameter of $60 \pm 3 \mu\text{m}$ at their input surface using the standard knife-method. In these conditions, LGN was damaged at an incoming energy of $500 \pm 10 \mu\text{J}$, corresponding to a peak power density of $2.8 \pm 0.7 \text{ GW/cm}^2$. It is a little bit lower than that of KTP where the damage was observed at $760 \pm 10 \mu\text{J}$, *i.e.* $4.3 \pm 1.1 \text{ GW/cm}^2$. Using the same setup and same KTP crystal as a reference, LGT had been damaged for an input energy of $480 \pm 10 \mu\text{J}$, which corresponds to a peak power density of $2.7 \pm 0.7 \text{ GW/cm}^2$ [3]. In our previous work, we reported a surface damage threshold of 1.41 GW/cm^2 in a 1-mm thick LGN slab using KDP as a reference [2]. They were illuminated by a Nd:YAG laser at $1.064 \mu\text{m}$ with a pulse duration of 10 ns (FWHM) and a repetition rate of 1 Hz. Moreover, the experimental protocol was different than the one we used here since the average power had been set at 20 mW and the beam waist diameter at the entrance surface of the slab was equal to $200 \mu\text{m}$. Furthermore, the slabs were moved toward the focal point until damage was observed at their input surface. All these differences could explain the different result.

4. Calculation of the supercontinuum generation by phase-matched OPG

Using our refined Sellmeier equations and the method described in ref [7], we showed that a supercontinuum can be generated using a type II phase-matched OPG *i.e.* $1/\lambda_p^o \rightarrow 1/\lambda_s^e + 1/\lambda_i^e$ when pumped at $\lambda_p = 0.982 \mu\text{m}$ in the (y, z) plane of LGN. Figure 6 shows that the emission could range between 1.4 and $3.45 \mu\text{m}$, the LGN crystal being cut at ($\theta_{PM} = 52^\circ$, $\varphi_{PM} = 90^\circ$). According to the value of d_{11} determined above, the calculated corresponding figure of merit $(d_{eff}^{yz})^2 / n^o(\lambda_p)n^e(\lambda_i)n^e(\lambda_s)$ is equal to $0.15 \frac{\text{pm}^2}{V^2}$ in LGN,

which is a relatively low value. However, the supercontinuum range and the figure of merit are both larger in LGN compared with LGT [1]. Concerning the pump laser to use, Fig. 6 shows that the tuning curve of LGN exhibits a quasi-supercontinuum behavior when the crystal is pumped at $\lambda_p = 1.064 \mu\text{m}$, while it is not anymore the case at $\lambda_p = 0.8 \mu\text{m}$.

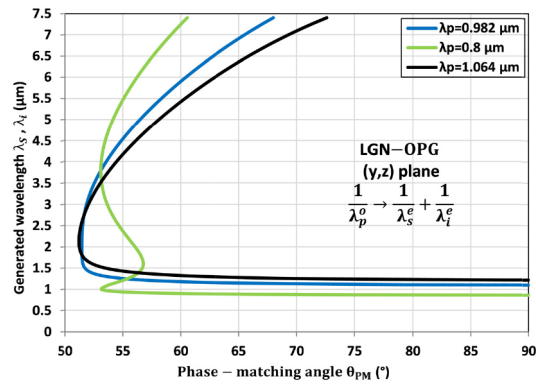


Fig. 6. Calculated OPG tuning curves in the (y, z) plane of LGN at different values of the pump wavelength λ_p .

5. Conclusion

We measured the SHG and DFG phase-matching tuning curves of LGN as well as the absolute magnitude of the associated nonlinear coefficient. These data can be used *per se* for designing any parametric device, but we also used them for refining the Sellmeier equations of the crystal. Using these equations, we found the possibility of generating a super continuum in the mid-IR by pumping LGN at the standard wavelength of emission of the Nd:YAG laser. This interesting feature combined with the ability of this crystal to be grown in large size and high optical quality put LGN in the category of the best nonlinear crystals for practical applications.

Acknowledgment

The authors thank the China Scholarship Council (CSC) for the financial supports of Feng Guo and Dazhi Lu.

Validation of the Angular Quasi-Phase-Matching theory for the biaxial optical class using PPRKTP

DAZHI LU,^{1,2} ALEXANDRA PEÑA,¹ PATRICIA SEGONDS,¹ JÉRÔME DEBRAY,¹ SIMON JOLY,³ ANDRIUS ZUKAUSKAS,⁴ FREDRIK LAURELL,⁴ VALDAS PASISKEVICIUS,⁴ HAOHAI YU,² HUIJIN ZHANG,² JIYANG WANG,^{2,5} CARLOTA CANALIAS,⁴ BENOÎT BOULANGER^{1,5,*}

¹ Univ. Grenoble Alpes, CNRS, Grenoble INP, Institut Néel, 38000 Grenoble, France

² State Key Laboratory of Crystal Materials and Institute of Crystal Materials, Shandong University, 27 Shanda Nanlu, Jinan 250100, China

³ IMS Laboratory, University of Bordeaux, UMR CNRS 5218, 351 Cours de la Libération, 33405 Talence, France

⁴ Laser Physics, Applied Physics Department, Royal Institute of Technology, AlbaNova University Center, Roslagstullsbacken 21, 10691 Stockholm, Sweden

⁵ Institute of Functional Crystals, Tianjin University of Technology, Tianjin, 300384, China

*Corresponding author: benoit.boulangier@neel.cnrs.fr

Received XX Month XXXX; revised XX Month, XXXX; accepted XX Month XXXX; posted XX Month XXXX (Doc. ID XXXXX); published XX Month XXXX

We report the first experimental validation of angular quasi-phase-matching (AQPM) theory in a biaxial crystal by performing second-harmonic generation (SHG) in the periodically-poled Rb-doped KTiOPO₄ (PPRKTP) crystal cut as a sphere. Both AQPM and birefringence phase-matching (BPM) angles were measured thanks to a Kappa circle. © 2018 Optical Society of America

OCIS codes: (160.4330) Nonlinear optical materials; (190.2620) Harmonic generation and mixing; (190.4410) Nonlinear optics, parametric processes.

<http://dx.doi.org/10.1364/OL.99.099999>

Nonlinear optics deals with a strong coupling between light and matter. Its ability to convert and tune the frequency range of existing laser sources is of prime importance in optical devices [1-2]. Phase-matching conditions should be fulfilled in order to obtain and improve frequency conversion during the nonlinear process. The common way for obtaining phase-matching is by using anisotropic crystals with refractive index dispersion and is called birefringence phase-matching (BPM)[1,3]. It is also possible to get phase-matching by a periodic modulation of the sign of the crystal's second-order nonlinear coefficient in one or two dimensions, which corresponds to quasi-phase-matching (QPM) [4,5]. It gives the possibility to access to the highest coefficient of the second-order electric susceptibility tensor [4,6] or to shape the spatial and spectral properties of light [7]. Recently, significant improvement of the electric field poling or bonding techniques have led to larger aperture QPM crystals. For example, few-millimeters-thick periodically poled 5%MgO:LiNbO₃

(5%MgO:PPLN) [8], LiTaO₃ (PPLT) [9], KTiOPO₄ (PPKTP) [10], Rb-doped KTiOPO₄ (PPRKTP) [11] and orientation-patterned GaAs (OP-GaAs) [12] have been successfully obtained. Such large-size artificial materials not only allow laser beams with large apertures and high energies to be used, but they also give the possibility to implement the angular quasi-phase-matching (AQPM) scheme proposed in 2007 [13]. It corresponds to a generalization of QPM since it can be achieved at any angle with respect to the grating vector of the artificial nonlinear medium. This scheme was validated for the first time in 2009 in the case of the uniaxial optical class by studying a 5% MgO:PPLN crystal shaped as a sphere [14]. By studying second-harmonic generation (SHG) and difference-frequency generation (DFG), it had been shown in particular that AQPM brings giant spectral acceptances compared with BPM. In this letter, we report the first validation of the AQPM proposal in the case of the biaxial optical class. We considered a crystal of PPRKTP because it can be obtained in larger size than PPKTP [10] and with a reliable control of the ferroelectric-domain structures [11]. The composition of the crystal we study is Rb_{0.003}K_{0.997}TiOPO₄, and its grating period is $\Lambda = 38.52 \mu\text{m}$ [15]. In the previous studies, PPRKTP was only used along the x-axis of the medium. In the case of 5% MgO:PPLN, the (x,z) plane of the crystal sphere was the only one to be considered. In the present study we aim at accessing to the full angular distribution of AQPM, inside and outside the principal planes.

We shaped the PPRKTP crystal as a sphere using a specific technique allowing us to get a perfect polishing and an asphericity below 1% [16]. We got a sphere with a diameter of 4.76 mm, as shown in Fig. 1(a), the volume of the sphere being fully periodically poled as shown in Fig. 1 (b).

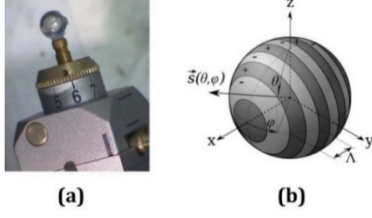


Fig. 1. (a) PPRKTP sphere used for the experiments. (b) Scheme of AQPM in the sphere where Λ is the grating periodicity along the x -axis and $\vec{s}(\theta, \varphi)$ is the unit vector of the wave vectors of the interacting waves where (θ, φ) are the angle of spherical coordinates in the dielectric frame (x, y, z) .

The AQPM condition is given by the following equation [13]:

$$\frac{n_3^\pm(\theta, \varphi)}{\lambda_3} - \frac{n_2^\pm(\theta, \varphi)}{\lambda_2} - \frac{n_1^\pm(\theta, \varphi)}{\lambda_1} - \frac{1}{\Lambda_{eff}(\theta, \varphi)} = 0 \quad (1)$$

θ and φ are the angles of spherical coordinates in the dielectric frame (x, y, z) . λ_1, λ_2 and λ_3 are the wavelengths of the three interacting waves that are linked by energy conservation, *i.e.* $\lambda_3^{-1} = \lambda_2^{-1} + \lambda_1^{-1}$; n_1^\pm, n_2^\pm and n_3^\pm are the corresponding refractive indices in the considered AQPM direction (θ, φ) , the signs $+$ and $-$ denoting the two possible values of the refractive index according to birefringence. In the following, the notations $\lambda_\omega (= \lambda_1 = \lambda_2)$ and $\lambda_{2\omega} (= \lambda_3)$ for the fundamental and second-harmonic (SH) wavelengths respectively will be used. $\Lambda_{eff}(\theta, \varphi) = \Lambda |\sin(\theta) \cos(\varphi)|^{-1}$ is the effective grating periodicity in the direction (θ, φ) : it ranges from a minimal value corresponding to a propagation of the interacting waves along the x -axis, *i.e.* $\Lambda_{eff}(\theta = 90^\circ, \varphi = 0^\circ) = \Lambda$, to a maximal one obtained when propagation occurs in the y - z plane, *i.e.* $\Lambda_{eff}(\theta, \varphi = 90^\circ) \rightarrow \infty$. Note that AQPM authorizes six possible combinations of refractive indices in Eq. (1) for SHG, which defines the six SHG AQPM types, BPM exhibiting only two of them [3, 13].

The Sellmeier equations of RKTTP are not known, therefore we used those of KTP since the Rubidium concentration is small (0.3%). Then we used the Sellmeier equations of Ref. [17] for the calculation of the SHG AQPM angles. We found that only four SHG AQPM types are allowed among the six possible types, and that for fundamental wavelengths above $2.098 \mu\text{m}$. At this wavelength, type V AQPM exists only along the x -axis, and it disappears for smaller wavelengths. We chose $2.15 \mu\text{m}$ as fundamental wavelength, which was close to the cut-off of the source we used. The four AQPM relations are given in Tab. 1., and the corresponding angular tuning curves at $\lambda_\omega = 2.15 \mu\text{m}$ are shown in Fig. 2.

Table 1 Possible SHG AQPM types in PPRKTP; n^+ and n^- are the two possible values of the refractive index at the fundamental or second harmonic wavelengths, λ_ω and $\lambda_{2\omega}$ respectively, in the AQPM direction (θ, φ) .

Types	AQPM relations
I	$n_{2\omega}^-(\theta, \varphi) \lambda_{2\omega}^{-1} = 2n_\omega^+(\theta, \varphi) \lambda_\omega^{-1} + \Lambda_{eff}^{-1}(\theta, \varphi)$
II	$n_{2\omega}^-(\theta, \varphi) \lambda_{2\omega}^{-1} = n_\omega^+(\theta, \varphi) \lambda_\omega^{-1} + n_\omega^-(\theta, \varphi) \lambda_\omega^{-1} + \Lambda_{eff}^{-1}(\theta, \varphi)$
IV	$n_{2\omega}^-(\theta, \varphi) \lambda_{2\omega}^{-1} = 2n_\omega^-(\theta, \varphi) \lambda_\omega^{-1} + \Lambda_{eff}^{-1}(\theta, \varphi)$

$$V \quad n_{2\omega}^+(\theta, \varphi) \lambda_{2\omega}^{-1} = 2n_\omega^+(\theta, \varphi) \lambda_\omega^{-1} + \Lambda_{eff}^{-1}(\theta, \varphi)$$

Figure 2 also shows the tuning curves of types I and II BPM at $\lambda_\omega = 2.15 \mu\text{m}$. The corresponding phase-matching relations can be obtained from those of types I and II AQPM given in Tab. 1 by doing $\Lambda_{eff}(\theta, \varphi) \rightarrow \infty$. The consideration of BPM in this framework of AQPM is relevant from the experimental point of view as it will be shown hereafter. As seen in Fig. 2, all the tuning curves range between the (x, z) and the (x, y) or (y, z) planes, which determine a specific strategy for scanning the space in order to measure the corresponding phase-matching angles, as shown in Fig. 3. The method consists in rotating the sphere around the z -axis by incremental values of the angle φ (φ -Scanning), and, for each value of φ , the sphere is then rotated by the angle θ (θ -Scanning) until the fundamental beam and the phase-matching direction are in coincidence in the plane that is considered. One cone surrounding the x -axis and the other one the z -axis, so the best choice was to stick the sphere along the y -axis. A Laue orientation of the sphere gives us a precision better than 0.05°

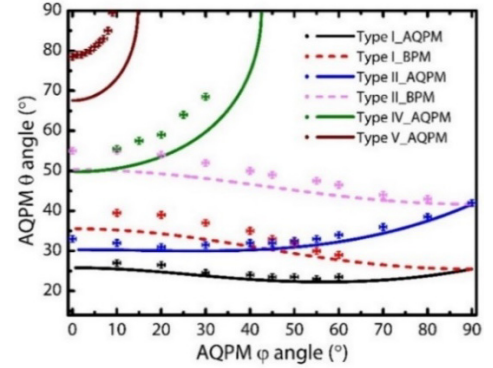


Fig. 2. All the possible SHG AQPM and BPM curves calculated in PPRKTP pumped at a wavelength of $2.15 \mu\text{m}$ are shown as solid and dashed lines, respectively. Cross dots stands for the experimental data.

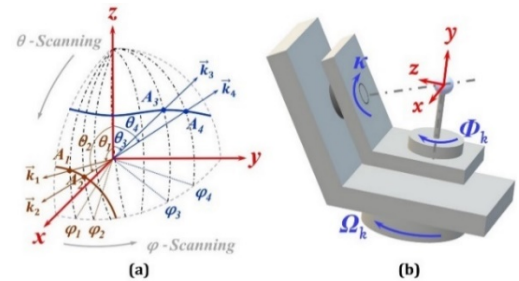


Fig. 3. (a) Schematic diagram of the scanning mode for determining the two possible topologies of phase-matching cones, *i.e.* around the x -axis (brown) or z -axis (blue). The \vec{k}_i 's ($i = 1, 2, 3, 4$) correspond to the phase-matching directions at the angles θ_i and φ_i crossing the cones at A_i . (x, y, z) is the dielectric frame; (b) Schematic diagram of the Kappa circle, consisting in the three rotation angles κ, Φ_k and Ω_k .

The sphere was then placed at the center of a Kappa circle described in Fig. 3(b). It was motorized by stepper motors with an accuracy of 0.003° and controlled by precise electronics. The three rotation axes κ, Φ_k and Ω_k are arranged in such a way that the axis

of rotation κ is placed at a non-zero angle with respect to the vertical direction. This arrangement enables multiple combinations between the three axes for a same direction, that allowed us to choose the combination for which we had no “blind spot”. The correspondence between the angles of spherical coordinates (θ, φ) and the Kappa angles $(\Omega_k, \kappa, \Phi_k)$ is established thanks to a homemade interfacing program with a command system.

Then the PPRKTP sphere was illuminated by a beam at the fundamental wavelength $\lambda_\omega = 2.15 \mu\text{m}$. It was emitted by an optical parametric oscillator that delivers 5-ns-FWHM pulses at 10-Hz-repetition rate. A half-wave plate allowed the incident beam to be polarized according to the chosen AQPM types. A focusing lens was properly located at the entrance of the sphere, ensuring the quasi-parallel propagation of the beams inside the sample [14]. The energy of the generated beam was measured at the exit of the sphere by an amplified Si Hamamatsu C2719 photodiode placed after a 75-mm-focusing lens, a filter removing the fundamental beam. The phase-matching wavelengths were controlled by a NIRquest 512 Ocean Optics spectrometer with an accuracy of ± 3 nm. The SHG phase-matching angles are detected when the associated conversion efficiency is maximal. The corresponding angular accuracy is of $\pm 0.5^\circ$. Figure 4 gives the example of the determination of type V AQPM angle at $\lambda_\omega = 2.15 \mu\text{m}$ in the (x, z) plane of the PPRKTP sphere.

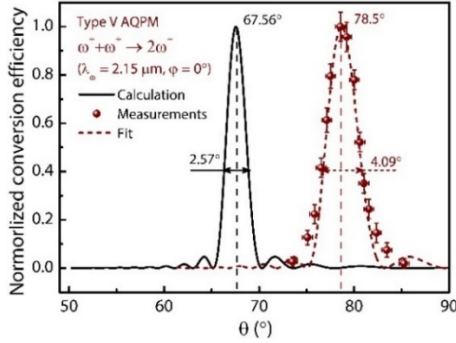


Fig. 4. Measured (dots fitted by dashed line) and calculated (solid line) SHG conversion efficiency as functions of θ angle of Type V AQPM.

It clearly appears from Fig. 4 that the experimental AQPM angle in the (x, z) plane is $\theta = 78.5 \pm 0.5^\circ$, which is bigger than the calculated one, *i.e.* 67.56° . This discrepancy is due to the fact that the Sellmeier equations we used for the calculation are those of KTP [17], as mentioned above. The experimental and calculated angular and spectral acceptances are also larger than the calculated values because there is a small divergence inside the sphere, of about several mrad. Following this scanning process, we measured the entire angular tuning curves of types I, II, IV and V. As shown in Fig. 2, there is a shift of a couple of degrees between measurements and calculations. But the behaviors are the same, and we also confirmed the fact that no more than the four calculated AQPM types are allowed, which was the first step in the validation of the AQPM theory in a biaxial crystal. Note also that the measured Types I and II BPM curves agree with the calculation, which highlights the fact that the periodical poling does not modify the refractive indices.

The second step of validation concerned the angular evolution of the effective coefficient. As PPRKTP belongs to the crystal class

mm2, there exist five independent nonlinear coefficients in the case of SHG, *i.e.* using the contracted notation : d_{15} , d_{24} , d_{31} , d_{32} and d_{33} [18]. Thus the effective coefficient corresponding to any AQPM direction (θ, φ) can be calculated using the following equation :

$$d_{eff}(\theta, \varphi) = \frac{2}{\pi} \begin{bmatrix} d_{15}(2\omega)(F_{xz}(\theta, \varphi) + F_{zx}(\theta, \varphi)) \\ + d_{24}(2\omega)(F_{yz}(\theta, \varphi) + F_{zy}(\theta, \varphi)) \\ + d_{31}(2\omega)F_{xx}(\theta, \varphi) + d_{32}(2\omega)F_{yy}(\theta, \varphi) \\ + d_{33}(2\omega)F_{zz}(\theta, \varphi) \end{bmatrix} \quad (2)$$

with

$$F_{ijk}(\theta, \varphi) = e_i^\pm(2\omega, \theta, \varphi) e_j^\pm(\omega, \theta, \varphi) e_k^\pm(\omega, \theta, \varphi) \quad (3)$$

The index i stands for x, y or z , and e_a^\pm ($a = i, j, k$) represent the unit vectors of the electric fields of the different interacting waves corresponding to the refractive indices of Tab. 1 according to the type that is considered. From Eqs. (2) and (3), it appears that the only cases for which the effective coefficient is zero are those of types I and IV in the principal planes. Table 2 gives the expression of the effective coefficient for types II and V AQPM, for which it has a non zero value in the principal planes.

Table 2 Non-zero effective coefficient in (x, z) and (x, y) principle planes; ρ is the Poynting walk-off angle.

Types	Planes	Effective coefficients (d_{eff})
II	(x, z)	$(2/\pi).d_{24} \sin(\theta - \rho_\omega(\theta))$
	(y, z)	$(2/\pi).d_{15} \sin(\theta - \rho_\omega(\theta))$
V	(x, z)	$\left(\frac{2}{\pi}\right) \left[2d_{15} \sin(\theta - \rho_\omega(\theta)) \cos(\theta - \rho_\omega(\theta)) \cos(\theta - \rho_{2\omega}(\theta)) \right. \\ \left. + \sin(\theta - \rho_{2\omega}(\theta)) (d_{31} \cos^2(\theta - \rho_\omega(\theta)) + d_{33} \sin^2(\theta - \rho_\omega(\theta))) \right]$
	(x, y)	$(2/\pi).d_{33}$

The effective coefficient acts at the level of the Figure of Merit (FOM) through the following equation [18]:

$$FOM(\theta, \varphi) = \frac{d_{eff}^2(\theta, \varphi)}{n_\omega^\pm(\theta, \varphi) \cdot n_\omega^\pm(\theta, \varphi) \cdot n_{2\omega}^\pm(\theta, \varphi)} \quad (4)$$

In order to avoid the difficulties associated with absolute measurements, we considered a normalized SH intensity defined as follows:

$$I_{2\omega}^N(\theta, \varphi) = \frac{I_{2\omega}(\theta, \varphi)}{I_{2\omega}(\theta, \varphi = 0^\circ / 10^\circ)} \approx \frac{FOM(\theta, \varphi)}{FOM(\theta, \varphi = 0^\circ / 10^\circ)} \quad (5)$$

It corresponds to the ratio between the SH intensities at different AQPM angles (θ, φ) and the SH intensity at the minimal value of φ corresponding to the different types: $\varphi = 0^\circ$ for types II and V AQPM, and $\varphi = 10^\circ$ for types I and IV since the corresponding effective coefficients are zero in the principal planes as mentioned above. The calculated and measured normalized SH intensities are plotted in Fig. 5 as a function of the AQPM angle φ for the four AQPM types. The corresponding AQPM angles θ are given by the four curves of Fig. 2. Figure 5 confirms the very good agreement between theory and experimental results. Note that there is an abnormal peak on the type II AQPM curve of Fig. 5(b)

for φ ranging from 40° to 60° . That can be well explained by the crossing of this curve with that of type I BPM, as shown in Fig. 2. Actually, BPM can exist in a periodically-poled medium since birefringence exists.

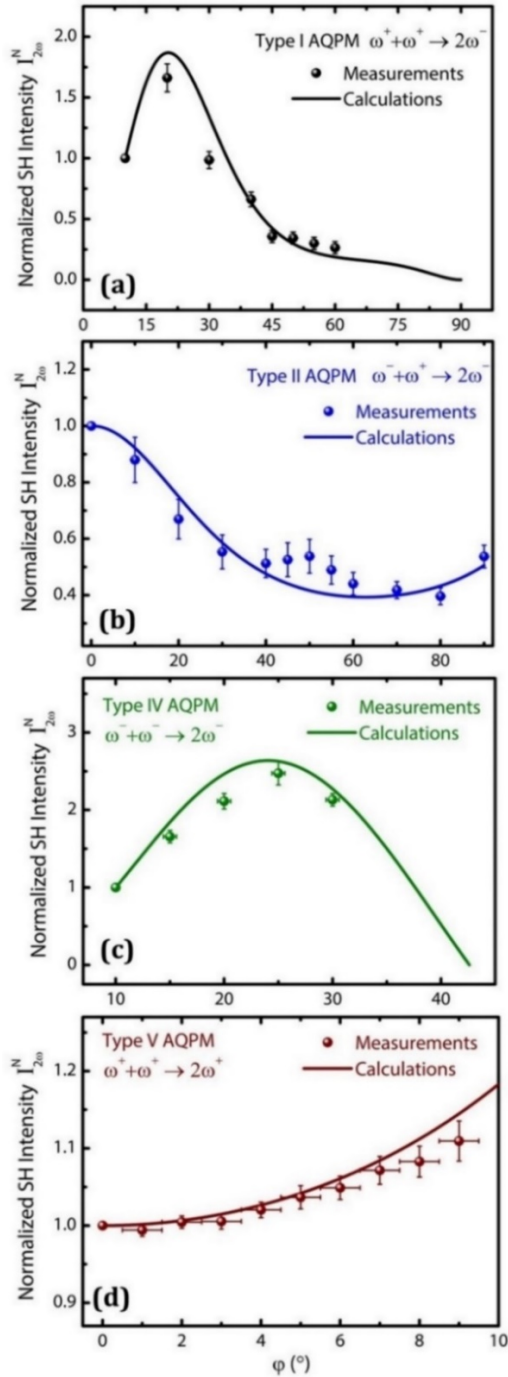


Fig. 5. Normalized SH intensities as a function of types I, II, IV and V AQPM angles φ for a fundamental wavelength $\lambda_\omega = 2.15 \mu\text{m}$.

The coexistence of BPM and AQPM is then possible if the phase-matching directions are in coincidence, and if there are the required common polarization states, which is the case for type I BPM and type II AQPM in PPRKTP. One of the polarization states of the fundamental waves for generating type I BPM ($\omega^+ + \omega^+ \rightarrow 2\omega^-$)

is the same as that of type II AQPM ($\omega^+ + \omega^- \rightarrow 2\omega^-$), *i.e.* the (+) mode, therefore, type I BPM is automatically excited during a type II AQPM experiment due to the common fundamental mode (+). Figure 2 also shows an intersection between the angular tuning curves of type IV AQPM ($\omega^- + \omega^- \rightarrow 2\omega^-$) and Type II BPM ($\omega^- + \omega^+ \rightarrow 2\omega^-$) for φ ranging from 0° to 10° . But in that case, Type II BPM cannot be excited during a type IV AQPM because the fundamental (+) mode is missing. Then type II BPM cannot influence the tuning curve of type IV AQPM, which can be verified in Fig. 5 (c).

As a conclusion, we performed the first experimental validation of the AQPM proposal in the case of the biaxial optical class by performing SHG at a fundamental wavelength of $2.15 \mu\text{m}$ in a large-aperture PPRKTP shaped as a sphere. The angles of the four possible AQPM types were measured by the sphere method using a Kappa circle, and it is the first time that AQPM directions are explored out of the principal planes of a periodically poled medium. Meanwhile, the measured SH generated intensities matched perfectly well with the calculations. It is also the first time to the best of our knowledge that it has been shown that BPM can be excited during QPM without any modification of the respective angular distributions. The next step of this work will be devoted to AQPM experiments in the case of the isotropic optical class, by studying for example OP-GaAs or OP-GaP [19].

Funding. CNRS international project of scientific cooperation (PICS n°7739).

Acknowledgment. The authors thank the China Scholarship Council (CSC) for the financial supports of D. Lu, and Tianjin Short-term Recruitment Program for Foreign Experts for B. Boulanger.

References

1. J.A. Armstrong, N. Bloembergen, J. Ducuing and P.S. Pershan, Phys. Rev. **127**, 1918 (1962).
2. V. Petrov, Opt. Mat. **34**, 536 (2012).
3. J.P. Fève, B. Boulanger, and G. Marnier, Opt. Commun. **99**, 284 (1993).
4. M.M. Fejer, G.A. Magel, D.H. Jundt and R.L. Byer, IEEE J. Quantum Elect. **28**, 2631 (1992).
5. V. Berger, Phys. Rev. Lett. **81**, 4136 (1998).
6. H. Karlsson and F. Laurell, Appl. Phys. Lett. **71**, 3474 (1997).
7. R. Remez, N. Shapira, C. Roques-Carmes, R. Tirole, Y. Yang, Y. Lereah, M. Soljačić, I. Kaminer, and A. Arie, Phys. Rev. A **96**, 061801(R) (2017).
8. H. Ishizuki and T. Taira, Opt. Lett. **30**, 2918 (2005).
9. H. Ishizuki and T. Taira, Opt. Express **18**, 253 (2010).
10. J. Hellström, V. Pasiskevicius, H. Karlsson, and F. Laurell, Opt. Lett. **25**, 174 (2000).
11. A. Zukauskas, N. Thilmann, V. Pasiskevicius, F. Laurell and C. Canalias, Opt. Mater. Express **1**, 201 (2011).
12. T. Kubota, H. Atarashi, and I. Shoji, Opt. Mat. Exp. **7**, 932 (2017).
13. Y. Petit, B. Boulanger, P. Segonds and T. Taira, Phys. Rev. A **76**, 063817 (2007).
14. P. Brand, B. Boulanger, P. Segonds, Y. Petit, C. Félix, B. Ménaert, T. Taira and H. Ishizuki, Opt. Lett. **34**, 2578 (2009).
15. F. Masiello, T. A. Lafford, P. Pernot, J. Baruchel, D. S. Keeble, P. A. Thomas, A. Zukauskas, G. Strömqvist, F. Laurell and C. Canalias, J. Appl. Crystallogr. **44**, 462 (2011).
16. B. Ménaert, J. Debray, J. Zaccaro, P. Segonds, and B. Boulanger, Opt. Mat. Exp. **7**, 3017 (2017).
17. K. Kato and E. Takaoka, Appl. Optics **41**, 5040 (2002).
18. B. Boulanger and J. Zyss, *International Table for Crystallography*, (Kluwer Academic Publishers 2006).
19. P. G. Schunemann, L. A. Pomeranz, and D. J. Magarrell, in: Conference on Lasers and Electro-Optics, (OSA, 2015), p. SW30.1.

Résumé de thèse

L'optique non linéaire qui convertit la gamme de fréquences des sources lasers vers l'ultraviolet, le visible, l'infrarouge ou le térahertz, joue un rôle crucial pour la médecine, l'industrie, les applications militaires, la spectroscopie ou l'information quantique par exemple. L'accord de phase par biréfringence (BPM) ou le quasi-accord de phase (QPM) de processus non linéaires quadratiques dans des cristaux massifs sont deux voies privilégiées dans ce contexte. Au cours de ce travail de thèse, un cristal uniaxe de $\text{La}_3\text{Ga}_{5,5}\text{Nb}_{0,5}\text{O}_{14}$ (LGN) a été élaboré en utilisant la méthode de Czochralski, puis il a été étudié en configuration de BPM. Nous avons aussi validé la théorie du QPM angulaire (AQPM), qui correspond à la généralisation du QPM par la considération de n'importe quel angle par rapport au vecteur du réseau. Pour cela, nous avons étudié un cristal biaxe de Rb:KTiOPO_4 à domaines ferroélectriques alternés périodiquement (PPRKTP) usiné en forme de sphère. Tous ces résultats constituent une base fiable pour les études avenir consacrées à la conception de dispositifs pour la conversion de fréquence.

Mot clés: Optique non linéaire, Conversion de fréquences, Croissance de cristaux par Czochralski, Accord de phase par biréfringence, Quasi-accord de phase.

Abstract

Nonlinear optics converting the frequency range of laser sources to ultraviolet, visible, infrared or terahertz ranges, plays a crucial role in medicine, industry, military applications, spectroscopy or quantum information for example. Birefringence phase-matching (BPM) or quasi-phase-matching (QPM) of quadratic nonlinear processes in bulk crystals are two preferred alternatives in this context. During this PhD work, a $\text{La}_3\text{Ga}_{5,5}\text{Nb}_{0,5}\text{O}_{14}$ (LGN) uniaxial crystal was grown using the Czochralski method and then studied in the framework of BPM. We also validated the theory of angular QPM (AQPM), corresponding to a generalization of QPM by considering any angle with respect to the grating vector. For that purpose, we studied a periodically-poled large-aperture Rb:KTiOPO_4 (PPRKTP) biaxial crystal cut as a sphere. All these results provide a reliable corpus for further studies devoted to the design of frequency conversion devices.

Key words: Nonlinear optics, Frequency conversion, Czochralski crystal growth, Birefringence phase-matching, Quasi-phase-matching